UNIVERSIDAD COMPLUTENSE DE MADRID
FACULTAD DE CIENCIAS FÍSICAS

TESIS DOCTORAL

The JEM-EUSO infrared camera: prototype and Simulation

Prototipo y Simulación de la cámara infrarroja de JEM-EUSO

MEMORIA PARA OPTAR AL GRADO DE DOCTOR

PRESENTADA POR

José Alberto Morales de los Ríos Pappa

Directores

María Dolores Rodríguez Frías
Luis del Peral

Madrid

UNIVERSIDAD COMPLUTENSE DE MADRID

FACULTAD DE CIENCIAS FÍSICAS

TESIS DOCTORAL

The JEM-EUSO infrared camera: Prototype and Simulation

Prototipo y Simulación de la cámara infrarroja de JEM-EUSO

MEMORIA PARA OPTAR AL GRADO DE DOCTOR

PRESENTADA POR

José Alberto Morales de los Ríos Pappa

Directores:

Dra. María Dolores Rodríguez Frías,

Dr. Luis del Peral

Madrid, January 19, 2021

UNIVERSIDAD COMPLUTENSE DE MADRID

FACULTAD DE CIENCIAS FÍSICAS

TESIS DOCTORAL

The JEM-EUSO infrared camera: Prototype and Simulation

Prototipo y Simulación de la cámara infrarroja de JEM-EUSO

MEMORIA PARA OPTAR AL GRADO DE DOCTOR

PRESENTADA POR

José Alberto Morales de los Ríos Pappa

Directores:

Dra. María Dolores Rodríguez Frías,

Dr. Luis del Peral

Agradecimientos

A mi pequeñita, Olivia quiero estar cuando defiendas tú tesis.

A Asuka, gracias por apoyarme siempre para alcanzar mis metas.

A mis viejos (Mis Padres) por infundir el valor de los estudios y la perseverancia desde mi infancia.

A mis directores Dr. Luis del Peral y la Dra. María Dolores Rodríguez-Frías por creer en mí cuando yo sólo sabía la mitad de lo que estaba haciendo, la otra mitad la aprendí por el camino.

A mis compañeros del grupo SPAS-UAH (Miguel, Germán, Noelia, Héctor y Guadalupe); venga, que la próxima no será la espera tan larga!

A todos, Muchas Gracias...

Abstract

Cosmic Rays Physics is one of the fundamental Physics key issues and an essential tool of Astroparticle Physics that aims, in a unique way to address many fundamental questions of the extreme and non-thermal Universe in the Astroparticle Physics domain at the highest energies never detected so far. Moreover, Ultra High Energy Cosmic Rays (UHECR) has witnessed a breakthrough with the Pierre Auger Observatory (PAO) and Telescope Array (TA) success. The results on UHECR by PAO and TA have pointed out the huge physics potential of this field that can be achieved by an upgrade of the performances of current ground-based instruments and with new space-based missions. To fully explore the Extreme Universe, next-generation observatories need to observe the full sky and significantly increase UHECR exposure. To reach the largest exposures, space observatories are likely to be essential. The Extreme Universe Space Observatory (EUSO) space observatory aims to achieve one of our main goals, reach the so-called "Particle Astronomy Era."

The Extreme Universe Space Observatory (EUSO) of the International Space Station (ISS) will be the first space-based mission worldwide in the field of Ultra High-Energy Cosmic Rays (UHECR) and will provide a real breakthrough toward the understanding of the Extreme Universe at the highest energies never detected from Space so far. EUSO from space will pioneer the observation of cosmic rays at the extreme high energy range. EUSO will use our atmosphere as a huge calorimeter to detect the electromagnetic and hadronic components of the Extensive Air Shower (EAS). For UHECR experiments, the atmosphere is not only the showering medium for the primary cosmic ray; it is an essential part of the readout system as

well. A UHECR space observatory has an Atmospheric Monitoring System (AMS) to gather the atmosphere status data during the UHECR observation period. The AMS plays a fundamental role in our understanding of the atmospheric conditions in the Field of View (FoV) of the EUSO main telescope, and it will include an IR-Camera and a LIDAR. The AMS IR-Camera is an infrared imaging system aimed to detect the presence of clouds. This includes accurate detection of the cloud coverage and cloud top altitude.

In this work, a dedicated contribution at the System level to a novel and space qualified infrared camera has been accomplished. The space design and prototyping (Chapter 2), characterization, and laboratory dedicated tests of the infrared camera are presented. Tests have been performed at the Instituto de Astrofísica de Canarias (IAC) LISA laboratory, and the results will be discussed in Chapter 3.

An End to End (E2E) simulation of the infrared camera has been fully delivered and detailed in Chapter 4. An E2E dedicated simulation of the infrared camera gives us simulated infrared images of those we expect to obtain once the infrared camera is onboard a space mission. It provides us with the capabilities to study the impact of several scenarios of the atmosphere, in terms of retrieval temperature accuracy, to analyze the detection capabilities, calibration procedures, and a correction factor to be taken into account for the final data of the infrared camera onboard a space mission. At this design stage of the IR-Camera prototype, this E2E simulation will give some hints in key points of the design, like the compression algorithms evaluation, and an estimation of the expected accuracy of few calibration options.

Moreover, a novel computing model for EUSO has been fully developed

and presented in Chapter 5 for the processing of the ground segment support data to be produced by the EUSO space observatory every year, for the instrument's simulation and the data analysis tasks.

Resumen

La Física de Rayos Cósmicos es uno de los temas clave de la Física Fundamental y una herramienta esencial de la Física de Astropartículas que tiene como objetivo, de una manera única, abordar muchas cuestiones fundamentales del Universo extremo y no termal en el dominio de la Física de Astropartículas a las energías más altas nunca detectadas por el momento. Además, el campo de la radiación cósmica de ultra-alta energía ha sido testigo de un gran avance con el éxito del Observatorio Pierre Auger (PAO) y Telescope Array (TA). Los resultados sobre UHECR de PAO y TA han señalado el enorme potencial físico de este campo que se puede lograr mediante una mejora de las prestaciones de los instrumentos terrestres actuales y con nuevas misiones espaciales. Para explorar completamente el Universo Extremo, los observatorios de próxima generación deben observar el cielo completo y aumentar significativamente la exposición de radiación cósmica de ultra-alta energía (UHECR). Para alcanzar las mayores exposiciones, es probable que los observatorios espaciales sean esenciales. El observatorio espacial EUSO tiene como uno de nuestros principales objetivos, alcanzar la llamada "Era de la Astronomía de Partículas".

El Observatorio Espacial del Universo Extremo (EUSO) de la Estación Espacial Internacional (ISS) será la primera misión espacial en todo el mundo en el campo de los rayos cósmicos de energía ultra alta (UHECR) y proporcionará un avance real hacia la comprensión del Universo extremo. Universo con las energías más altas nunca detectadas desde el espacio hasta ahora. EUSO desde el espacio será pionero en la observación de rayos cósmicos en el rango de energía extremadamente alto. EUSO utilizará nuestra atmósfera como un gran calorímetro, para detectar los componentes electro-

magnéticos y hadrónicos de las cascadas atmosféricas extensas (EAS). Un observatorio espacial UHECR tiene un Sistema de Monitoreo Atmosférico (AMS), para recopilar datos del estado de la atmósfera durante el período de observación UHECR. El AMS juega un papel fundamental en nuestra comprensión de las condiciones atmosféricas en el campo de visión (FoV) del telescopio principal EUSO e incluirá una cámara IR y un LIDAR. La cámara IR AMS es un sistema de imágenes infrarrojas destinado a detectar la presencia de nubes. Además, la cobertura de nubes y la altitud de la cima de las nubes se lograrán con precisión.

En esta Tesis Doctoral se ha contribuido a nivel de Sistema al completo diseño de una cámara infrarroja novedosa y calificada para uso espacial. Se presentan el diseño y la creación de prototipos espaciales (Capítulo 2), la caracterización y las pruebas de laboratorio de la cámara infrarroja. Las pruebas se han realizado en el laboratorio LISA del Instituto de Astrofísica de Canarias (IAC) y los resultados se comentarán en el Capítulo 3.

La simulación E2E de la cámara infrarroja se ha llevado a cabo por completo y se detalla en el Capítulo 4. La simulación E2E de la cámara infrarroja nos proporciona imágenes infrarrojas simuladas de las que esperamos obtener una vez que la cámara infrarroja esté a bordo de la misión espacial. Nos ha permitido además estudiar el impacto de varios escenarios de la atmósfera, en términos de precisión de la temperatura de recuperación, para analizar las capacidades de detección, los procedimientos de calibración y el factor de corrección a tener en cuenta para los datos finales de la cámara infrarroja a bordo. En esta etapa de diseño del prototipo de cámara IR, esta simulación E2E dará información crucial en puntos clave del diseño, como la evaluación de algoritmos de compresión y una estimación de la precisión

esperada de algunas opciones de calibración.

Además, se ha desarrollado un modelo computacional novedoso para EUSO y se ha presentado en el Capítulo 5, para el procesamiento de los datos de apoyo del segmento terrestre que producirá el observatorio espacial EUSO cada año, para la simulación del instrumento y las tareas de análisis de datos.

Contents

List of Figures

List of Tables

Chapter 1

Introduction

Victor Hess first discovered indirect detection of radiation from outside the Earth surface in 1912[1]. These high energy particles were called *Cosmic Rays* and still represent a big challenge for physicists and astronomers. Huge progress has been made since then from the theoretical and experimental points of view. However, fundamental questions are still opened: where do they come from?, how are they accelerated to such high energies?, what is the composition of the highest energy cosmic rays?, how to interpret the features observed in the energy spectrum?, and so on. Furthermore, these questions are intrinsically linked, making it a more complex problem.

The origin of cosmic rays is not identified, especially for Ultra-High Energy Cosmic Rays (UHECRs), despite the limited numbers of astrophysical objects that can accelerate particles to such energies. With a steep power-law energy spectrum and possible Greisen-Zatsepin-Kuzmin effect, UHECR flux at highest energy (above $\approx E > 5 \cdot 10^{19}$ eV) is far small to investigate their origin by these ground-based experiments. Therefore, an Extreme Universe Space Observatory with a huge area is needed ([2], [3]. [4]).

1.1 Cosmic Radiation

Cosmic rays are high-energy charged particles originating in outer space that travel at nearly the speed of light and strike the Earth from all directions. Most cosmic rays are the nuclei of atoms, ranging from the lightest to the heaviest elements in the periodic table. Cosmic rays also include high energy electrons, positrons, and other subatomic particles. The term "cosmic rays" usually refers to galactic cosmic rays, which originate in sources outside the solar system, distributed throughout our Milky Way galaxy. However, this term has also come to include other classes of energetic particles in space, including nuclei and electrons accelerated in association with energetic events on the Sun (called solar energetic particles), and particles accelerated in interplanetary space. [5]

Cosmic rays were discovered in 1912 by Victor Hess when he found that an electroscope discharged more rapidly as he ascended in a balloon. He attributed this to a source of radiation entering the atmosphere from above, and in 1936 was awarded the Nobel prize for his discovery. For some time it was believed that the radiation was electromagnetic in nature (hence the name cosmic "rays"), and some textbooks still incorrectly include cosmic rays as part of the electromagnetic spectrum. However, during the 1930's it was found that cosmic rays must be electrically charged because they are affected by the Earth's magnetic field.

Most galactic cosmic rays have energies between 100 MeV (corresponding to a velocity for protons of 43% of the speed of light) and 10 GeV (corresponding to 99.6% of the speed of light). The number of cosmic rays with energies beyond 1 GeV decreases by about a factor of 50 for every factor of 10 increase in energy. Over a wide energy range the number of particles per

square meter per steradian per second with energy greater than E GeV is given approximately by $N(> E) = k(E + 1) - a$, where k is of the order of 5000 per square meter per steradians per second and a is approximately 1.6. The highest-energy cosmic rays measured to date have had more than 10^{20} eV, equivalent to the kinetic energy of a baseball traveling at approximately 100 mph!.

The Sun is also a sporadic source of cosmic ray nuclei and electrons accelerated by shock waves traveling through the corona and magnetic energy released in solar flares. During such occurrences, the intensity of energetic particles in space can increase by a factor of 102 to 106 for hours to days. Such solar particle events are much more frequent during the active phase of the solar cycle. The maximum energy reached in solar particle events is typically 10 MeV to 100 MeV, occasionally reaching 1 GeV (roughly once a year) to 10 GeV (roughly once a decade). Solar energetic particles can be used to measure the elemental and isotopic composition of the Sun, thereby complementing spectroscopic studies of solar material.

Cosmic rays include essentially all of the periodic table elements; about 89% of the nuclei are hydrogen (protons), 10% helium, and about 1% heavier elements. The common heavier elements (such as carbon, oxygen, magnesium, silicon, and iron) are present in the same relative abundances as in the solar system. However, there are important differences in elemental and isotopic composition that provide information on the origin and history of galactic cosmic rays.

1.2 Extensive Air Showers (EAS)

When high-energy cosmic rays undergo collisions with atoms of the upper atmosphere, they produce a cascade of "secondary" particles that shower down through the atmosphere to the Earth's surface. Secondary cosmic rays include pions (which quickly decay to produce muons, neutrinos, and gamma rays) and electrons and positrons produced by muon decay and gamma ray interactions with atmospheric atoms. The number of particles reaching the Earth's surface is related to the cosmic ray's energy that struck the upper atmosphere. Cosmic rays with energies beyond 10^{14} eV are studied with large "air shower" arrays of detectors distributed over many square kilometers that sample the particles produced. The frequency of air showers ranges from about 100 per square meter per year for energies $> 10^{15}$ eV to only about 1 per square kilometer per century for energies beyond 10^{20} eV. Large detectors placed deep in underground mines or underwater also studies cosmic ray interaction products such as neutrinos [6].

A proton originated EAS comprises the electromagnetic shower and the hadronic shower. The main difference between electromagnetic and hadronic showers is that the hadronic shower produces a large number of muons, which are hardly produced in the electromagnetic shower. The hadronic cascade consists of the nucleus itself and secondary nuclei and a large quantity of $\pi^{\pm}$ which decay to μ. The $\pi^{\pm}$ production is connected to π^0 production, which then decays to γ undergoing pair production and becoming part of the shower's electromagnetic part. Depending on the primary particle, the corresponding EAS is dominated by either electromagnetic shower cascades or hadronic ones. We will concentrate on the electronic component's behavior, which is the main part of an air shower. One rather simplified

model for EAS was put forward by Heitler in the 30s [7]. Considering that the two processes that govern the shower are bremsstrahlung and pair production, Heitler assumes in his model that a primary particle travels the depth-distance λ_{em} and then produces two particles with half the energy which do the same and so forth. The depth-distance or simply the depth is usually referred to with X and is defined as the integral of the density of the medium, the primary traverses as eq 1.1.

$$X(r) = \int_0^{r_{max}} \rho(r)\, \partial r \tag{1.1}$$

This pair generation process continues until the secondary particles have energy below the critical energy E_c at which losses due to ionization and particle production are the same ($E_c \approx 86$ MeV for electrons in the air). The number of particles as function of depth can be expressed as $N(X) = 2(X/\lambda_{em})$ and the maximum number of particles as $N_{max} = E_{initial}/E_c$. With the above, we can then calculate that the higher amount of particles are produced at the depth in equation 1.2, also called shower maximum.

$$X_{max} = \lambda_{em} \times log_2(N_{max}) \tag{1.2}$$

What we use to detect these particles are fluorescence and the Cherenkov radiation. The charged particles, mostly electrons, produced in the shower undergo inelastic collisions with the air molecules and can excite the transitions between two electronic states in the nitrogen molecule. The state emitting is in the wavelength of interest, i.e., between 300 nm and 400 nm (UV), mainly the 2nd positive state 2P of N2 and a smaller contribution of the 1st negative state 1N of N+ 2.

The excitation duration is in the order of 10 ns, and the fluorescence

light is emitted isotropically. Suppose we are not concerned with very low energies (keV). In that case, the fluorescence yield is independent of the primary particle's energy. Thus the fluorescence technique, measuring the number of produced electrons, which is a function of the energy, can be used for calorimetric measurements of the energy deployed. This is especially true if we consider that ionization takes about 90% of the primary cosmic ray energy. Of course, a good knowledge of the fluorescence yield is needed and is a challenging issue.

Besides the isotropic fluorescence emission, the charged particles, moving faster than light in the medium, also emit Cherenkov photons, which are not isotropic but strongly beamed along the shower axis.

Chapter 2

The infrared camera onboard the Extreme Universe Space Observatory

2.1 The Extreme Universe Space Observatory

The Extreme Universe Space Observatory (EUSO) [8] is an international, multi-agency mission aimed at investigating the nature and origin of Extreme Energy Cosmic Rays (EECRs) (charged particles, photons, neutrinos, with $E > 5 \cdot 10^{19}$ eV, the conventional GZK suppression) and opening the channel of High Energy Neutrino Astronomy. It will be meant to detect Ultra High Energy Cosmic Rays (UHECRs) using the whole Earth as a detector. EUSO telescope from the International Space Station (ISS) will orbit around the Earth every $\sim$ 90 minutes at the altitude of 350 km to 400 km to capture the moving track of the Ultra-Violet (UV) photons from Extensive Air Showers (EAS). The telescope has a super-wide ($\pm 30°$) Field of View (FoV) with optics made by Fresnel lenses. The telescope has a time resolution of 2.5 μs and a spatial resolution of about 0.5 km (corresponding to 0.07°) in nadir mode.

The experiment's main goal is to measure the UHECR primary particle's

energy and the shower's arrival direction. With this information, energy sources and acceleration mechanisms might be identified and studied.

The detected radiation is essentially the fluorescence light produced by the de-excitation of nitrogen molecules excited by the Extensive Air Showers (EAS) and a Cherenkov component due to the particles' high velocity. The fraction of this fluorescence and Cherenkov depends on the scattering and absorption of the atmosphere. Hence, one of the main problems detecting the signal of the fluorescence and Cherenkov light that arrives to the EUSO detector is the presence of clouds ([9], [10], [11], [12], [13], [14], [15]). Therefore a space-qualified infrared camera is mandatory in any space mission intended to detect cosmic radiation from Space.

The Greisen-Zatsepin-Kuzmin (GZK) suppression is a theoretical upper limit on how far UHECRs can travel through space. The GZK suppression states that cosmic rays above a certain energy, about $6x10^{19}$ eV, will interact with Cosmic Microwave Background (CMB) photons. Since CMB photons are everywhere, above this energy cutoff, the universe will be partially opaque to UHECRs, limiting them to a mean free path of about 50 Mpc if they are above the cutoff energy. Due to this effect and low flux for UHECR, a space detector with a huge collecting area is mandatory.

An Extreme Universe Space Observatory will address the following fundamental observational questions:

- How does the cosmic-ray spectrum continue beyond the existing data? Is there a maximum energy? Are there point sources responsible for the spatially correlated event pairs already observed? Is there anisotropy that indicates source regions?

- Are the EECRs protons, nuclei, photons, neutrinos, or exotic particles?

- What is the neutrino flux at extreme energies?
- Are there point sources of neutrinos? Are active galactic nuclei (AGN) or gamma-ray bursts (GRBs) copious sources of neutrinos? Are there other sources?
- What is the gamma-ray flux at extreme energies? Does it exhibit any predicted quantum gravity effects?

Interpreting the EUSO data will lead us to consider the following theoretical questions:

- What processes and what astronomical objects can generate radiation at these extreme energies?
- Are EHECRs the result of high-energy neutrinos arriving from distant sources?
- Must we postulate topological defects and/or supermassive relic particles to explain the observations?
- Is special relativity valid at extreme energies?
- Are the EHECRs a window to new physics at the TeV–PeV mass energy scale?

The use of the fluorescence and Cherenkov radiation as a measure of the characteristics of an UHECR has already been used and will be used by future ground-based cosmic ray detectors. The observational approach of EUSO, which looks at the atmosphere from a space-based telescope placed on the International Space Station (ISS), contains some peculiarities with respect to ground-based approaches. They deserve to be outlined to stress the different problems and opportunities which arise from them.

Since the ISS covers the whole Earth surface in the latitude range $\pm 51^{\circ}$ approximately and moves at a speed of $\sim$ 7 km/s, the variability of the scene seen by JEM-EUSO is much higher than that observed by a ground-based experiment. Moreover, the optics aperture implies that a portion as large as $\sim$ 200000 km^2 is observed at once. In such a large field of view, the atmosphere status and the expected detection acceptance can have a certain degree of non-homogeneity, whose effect has to be considered and evaluated. By far, this is the largest complication a space-based detection approach has to face in contrast to the ground-based experiments.

On the other hand, the use of a space-based detector has several very significant advantages:

- The non-proximity of the EUSO detector to the shower considerably diminishes the severe problems associated with the determination of the solid angle and the differential attenuation of the atmosphere traversal suffered by the UV light, also within the same shower.
- The near-constant fluorescence emission rate at any height below the stratosphere allows to make simple and justified assumptions on the relationship between the energy and the fluorescence yield at the shower maximum as well as regards the relationship between the time width of the shower and the altitude at which it is produced.
- The observation of the fluorescence from above allows the method to be much less sensitive to the presence of most aerosols that are limited to altitudes below the atmospheric boundary layer.

The observational approach of EUSO is based on the measurement of fluorescence and Cherenkov photons produced by the UHECR shower as it

progresses through the atmosphere.

A hadronic UHECR (Ultra High Energy Cosmic Rays at E = 10^{18} eV) penetrating the earth's atmosphere will interact promptly and generate an Extensive Air Shower (EAS). After the first interaction, a shower of secondary particles will be produced. These secondary particles, whose number ($> 10^{11}$) is proportional to the energy of the primary UHECR, will deposit their energy in the atmosphere. A fraction of the total energy carried by the charged particles ($\sim$0.5%) will be converted into fluorescence photons through the excitation of N_2 molecules. A highly beamed Cherenkov radiation is generated as well by the ultrarelativistic particles in the shower. The fluorescence light is emitted isotropically by the N_2 molecules along the shower's path. The fluorescence yield depends on the local pressure and temperature but appears rather constant with the altitude, below 15 km.

The EUSO observational approach mainly relies on the fact that, thanks to the huge amount of emitted light, a fraction ($\sim 10^{-11}$) of these photons will reach a light-collecting device of few squared meters, placed outside the atmosphere, at the ISS height of $\sim$ 400 km, looking downward to the Earth at night, as shown in Figure 2.1.

Typically, for a 10^{20} eV shower, a few thousand photons will reach the EUSO detector. As the EUSO telescope has a Fresnel lens system associated with a fast counting, pixelized focal surface, EUSO will detect the number of photons arriving plus their direction and time of arrival. It is the observation of this specific space-time correlation that identifies, very precisely, the presence of an UHECR shower.

It is important to notice that, apart from the incident energy, the integrated number of photons and the shower's time duration will also depend

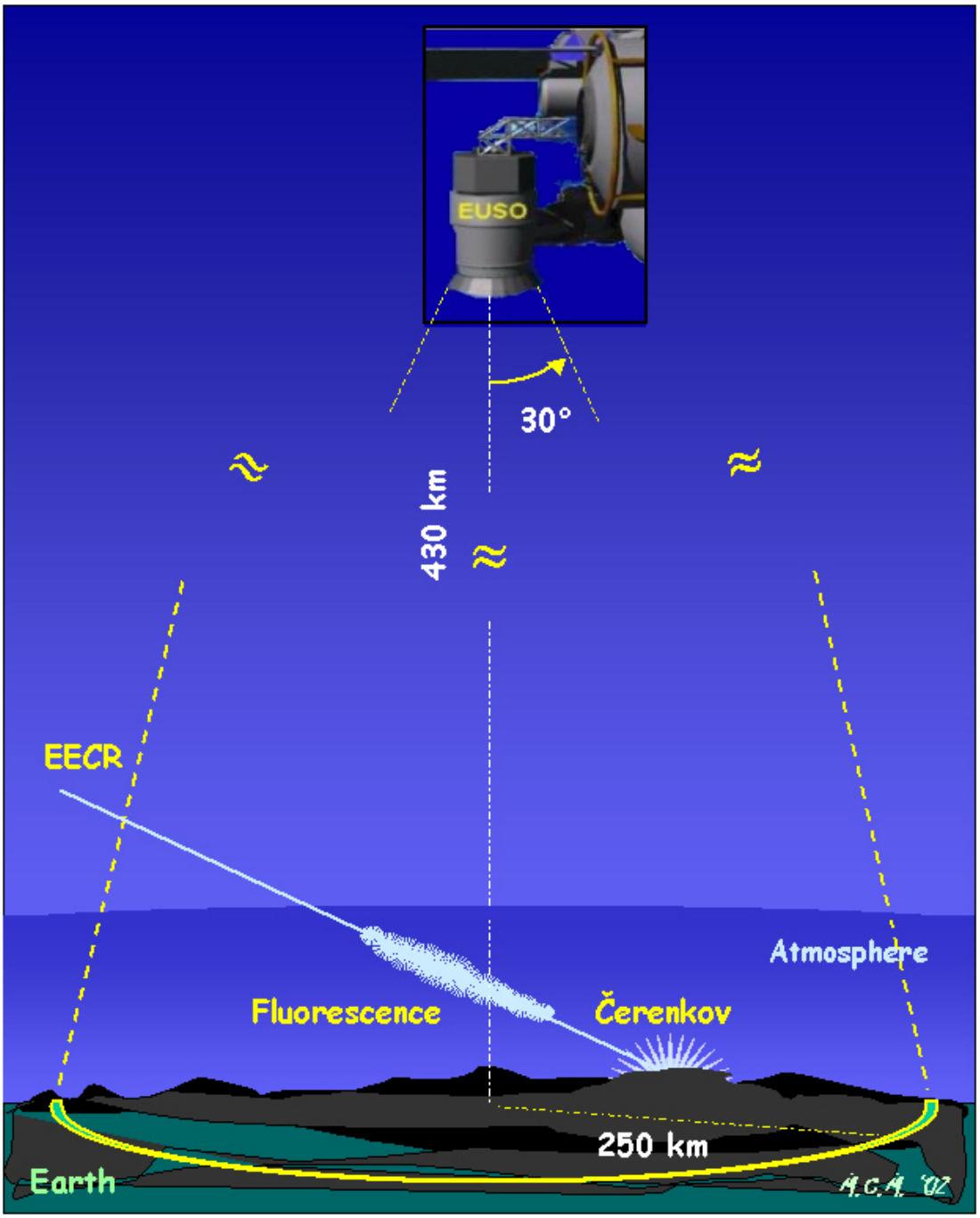

Figure 2.1: Artistic view of the JEM-EUSO observational approach doing astronomy looking downward the night Earth atmosphere.

on the shower angle. A vertical shower will develop rapidly ($\Delta t \sim 100$ μs) and, in some case, the maximum of the shower development (S_{max}) will not be reached before the ground. Conversely, at high altitude, a quasi-horizontal shower will develop over a long track, and its duration time will

be much larger, possibly reaching values $\Delta t \geq 300$ μs.

Because the secondary shower particles' velocities are higher than the local velocity of light, Cherenkov emission is also emitted. This emission is focused (within a cone of $\sim 1.3^{\circ}$ radius) along the shower axis and will be visible by EUSO through two effects. The first effect is the possible diffusion of the Cherenkov photons by the atmosphere's molecular and aerosol content, i.e. the Rayleigh and Mie large angle scattering processes. The second effect is due to the "albedo" of the ground surface, viewed as a rough discontinuous surface, as far as the refraction index is concerned. A similar effect can also be due to the presence of clouds that will act as an efficient reflective layer. Depending on the optical depth of the clouds, the effective albedo can reach up to 80%. In the case of a water surface, the albedo is typically an order of 5% to 8%. The Cherenkov radiation corresponds to a large band in wavelength 200 nm to 500 nm and has a λ^{-2} wavelength dependence.

2.2 The Infrared Camera of the Extreme Universe Space Observatory

2.2.1 Infrared Radiation

Infrared (IR) light is electromagnetic radiation with longer wavelengths than visible light, extending from the nominal red edge of the visible spectrum at 760 nm to 1000 μm. This range of wavelengths includes most of the thermal radiation emitted by objects near room temperature. Infrared light is emitted or absorbed by molecules when they change their rotational-vibrational movements. The existence of infrared radiation was first discovered in 1800

by astronomer William Herschel [16].

The infrared spectrum (Figure 2.2) may be split up into further regions:

- Near Infrared (Short wave IR) – between 760 nm to 2000 nm.
- Mid Infrared (Medium wave IR) – between 2000 nm to 4000 nm.
- Far Infrared (Far IR) – between 4000 nm (or 4 μm) to 1000 μm (or 1 mm).

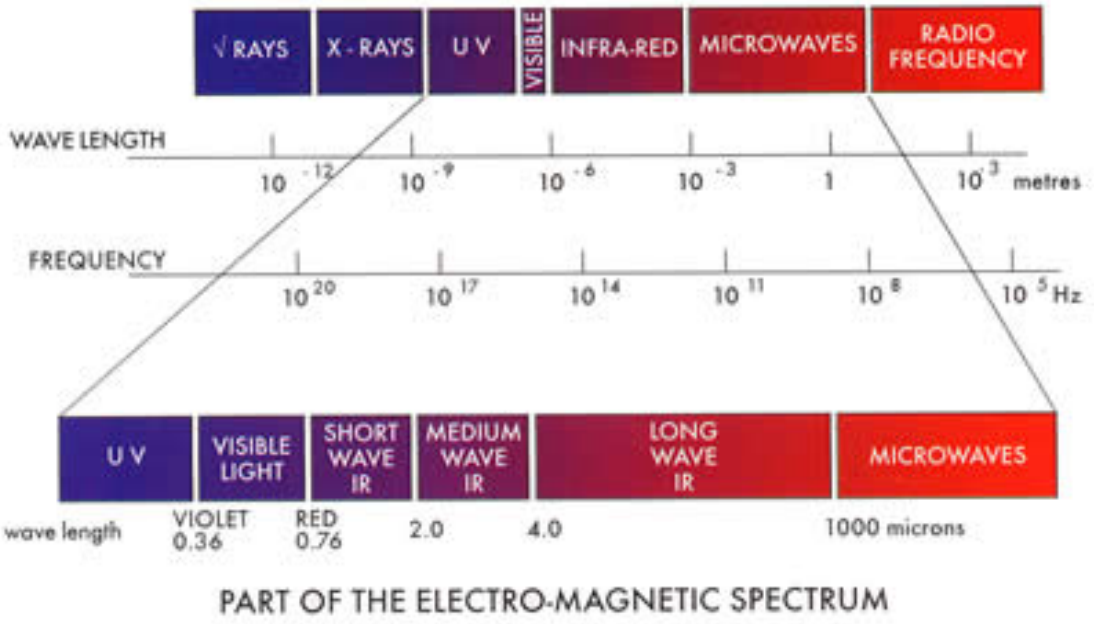

Figure 2.2: The electromagnetic spectrum.

The emissivity of a material (usually written ϵ or e) is the relative ability of its surface to emit energy by radiation. The ratio of energy radiated by a particular material to energy radiated by a black body at the same temperature. A true black body would have an $\epsilon = 1$ while any real object would have $\epsilon < 1$. Emissivity is a dimensionless quantity.

Infrared emitters are usually classified into one of these ranges by their temperature in operation. Typical temperatures are:

- Near Infrared: 2100° C

- Mid Infrared: 750° C to 1200° C
- Far Infrared: below 600° C

Thermal infrared radiation also has a maximum emission wavelength, which is inversely proportional to the object's absolute temperature, in accordance with Wien's displacement law.

2.2.2 Infrared Camera Space Instrument

The infrared camera will measure the radiance coming from the Earth-clouds-atmosphere system and retrieve the cloud temperature from the measured radiance. Moreover, the infrared camera is constrained by the EUSO requirements under space qualification. Therefore the measurements will be performed at night. For that reason, the radiance observed will be basically related to the temperature and the emissivity.

Infrared Camera Space Design

The infrared camera design is composed of three main blocks ([17], [18]):

- IRCAM Telescope Assembly
- IRCAM Electronic Assembly
- IRCAM Calibration Unit

The Telescope Assembly; detector and Front End Electronics

IRCAM Telescope Assembly encompasses the Infrared detector, the Front End Electronics (FEE), and all the optical lens assembly. Its main function is to acquire the infrared radiation and to convert it into digital counts ([17], [18]).

Table 2.1: Requirements for the IR-Camera of the EUSO Space Mission.

Parameter	Target value	Comments
Measurement range	220 K - 320 K	Annual variation of cloud temperature plus 20 K margin
Wavelength	10 μm to 12 μm	Two atmospheric windows available: 10.3 μm to 11.3 μm and 11.5 μm to 12.5 μm
FoV	48°	Same as main instrument
Spatial resolution	0.1° (Goal) 0.2° (Threshold)	@FOV centre
Absolute temperature accuracy	3 K	500 m in cloud top altitude
Mass	$\leq$ 11 kg	Inc 20% margin.
Dimensions	400 $\times$ 400 $\times$ 370 mm	w/o Insulation and mounting bracket.
Power	$\leq$ 15 W	Inc 20% margin.
Lifetime	5 years On-orbit	+2 years On-ground

A dedicated optical design has been developed due to the difficulty of acquiring radiation at very far infrared wavelength 10 μm to 12.5 μm. Its function is collecting the infrared radiation through filtering capability and imaging it into the detector. The optical design has to be very fast in terms of f-number; and guarantee the requested FoV, the same as the main instrument. Ge lenses have been manufactured due to this material's excellent properties in terms of transparency in the infrared region under study and rad-hard qualifies.

The detector in the current baseline is the uncooled amorphous silicon microbolometer manufactured by ULIS. The array dimensions will be 640x480 pixels. A thermo-electrical cooler will guarantee a very stable temperature on the Focal Plane Array (FPA). The working operative temperature is around 303 K.

The IR camera spectral selection needed to meet EUSO requirements will be attained by two filters centered at 10.8 μm and 12 μm. The bandwidth of both filters is 1 μm. The filters are mounted on a Ge substrate located just in front of the detector and placed side by side so that the scenario will be divided into two parts. One of the parts will be observed in the band centered in 10.8 μm and the other in the band centered in 12 μm. This arrangement permits a bispectral snapshot camera without a dedicated filter wheel mechanism to have a more reliable baseline and reduce costs.

The FEE manages and drives the muBolometer array. It retrieves the pixel data from the detector, pre-amplifies, and transfers it to the specific acquisition chain. It provides the bias and the sequencer, and manages the modes of image acquisition. The FEE communicates with the ICU and provides the uncompressed raw images.

The electronics assembly

The IRCAM Electronic Assembly shall provide mechanisms to process and transmit images obtained from an IR detector controlled by a dedicated Front End Electronic Board ([19], [20]). The following functionalities have been included to implement these features:

- A processing stage to compress and then format the image bitstream.
- A driver stage to manipulate the actuators of the system.
- A Power Supply Unit to control the system power consumption.
- High integration and easy testing capabilities.

The Electronic Assembly is composed of two main sections:

- Instrument Control Unit (ICU)
- Power Supply Unit (PSU)

Both blocks follow cold redundancy architecture and are placed on individual PCBs. The ICU processes data generated by the FEE and controls several aspects of the system management such as the electrical system, the thermal control, mechanisms (shutter, blackbodies, etc.), data management (compression, format), and the communication with the platform computer. The ICU manages the actuators of the instrument. The Power Supply Unit (PSU) receives the main power bus from EUSO main telescope, and it provides the required power regulation to the system and the subsystems.

The calibration subsystem

The IRCAM calibration function will provide means to correct on the final data product the effects of non-desired sources, being these sources errors

or other sources (natural sources for instance or thermal radiative sources) ([19], [20]).

The calibration unit is mainly composed of:

- Two Black Bodies + Temperature controlled Shutter.
- Mechanism and the motor.
- The positioning system
- Calibration Thermal control

This unit has to guarantee a reference internal temperature to carry out the radiometric calibration of the data coming out of the FEE. Following operational modes' strategy, four positions are provided from this unit: Acquire, Shutter (offset correction), Calibration Hot point, and Calibration Cold point.

To validate the design of some key subsystems in IRCAM, prototypes, and breadboard models (BBM) have been built in a preliminary phase of the project. In the detector proximity electronics, the so-called Front End Electronics Prototype (FEEP) has been developed. At the end of the prototype development, manufacturing and testing, the aim is to design the IRCAM FEE, which guarantees that the specifications are fulfilled in terms of electrical functions. To build a prototype with a similar performance to the flight design, the prototype's components were selected to be the equivalent non-flight parts or similar parts with a noise performance equivalent to the flight components. FEEP is not representative of the flight model neither in form nor in radiation characteristics.

Chapter 3

Characterization of the IR-Camera Prototype

This chapter presents the validation of the ULIS UL-04-17-1 micro-bolometer for space applications in the EUSO mission. The detector validation's main issue is that the so-called Front-End Electronics (FEE), even in the design phase, is not the final one of the flight phase. To overcome this problem, I have used a commercial prototype electronics developed by INO (Canada). With this module known as IRXCAM-640, it seems possible to configure and handle the array under test using almost any available configuration. In some cases, the micro-bolometer and the FEE (in this case, the above mentioned IRXCAM-640, which includes data output to a PC-based platform, and it is by far more functional than a typical FEE) are strongly dependent. This is the main reason why it is difficult in some cases to split results. However, most of them are detector-limited. The INO IRXCAM-640 is a versatile and reliable electronics module, and its performances are also explained in this chapter in brief detail.

Table 3.1: Main characteristics of the ULIS UL-04-17-1 detector.

Parameter	**Value**
Focal plane	640×480 pixels
Frame rate	up to 60 Hz
Pixel pitch	25 μm
Dimensions	$23.5 \times 32 \times 7.7$ mm
Power consumption	< 300 mW (without TEC).
Spectral response	LWIR
Typical response	5 mV/K
Sensitive area	16×12 mm
Output dynamic range	1.0 V to 4.2 V
Outputs	Configurable 1 or 2 analog outputs.
Qualifications	NIL STD 883-810 (in progress)
Weight	25 g

3.1 The ULIS UL-04-17-1 Microbolometer Array

The chosen micro-bolometer array is the UL-04-17-1 from ULIS (France), a 640×480 pixels LWIR un-cooled micro-bolometer. In-depth explanation of its performances and handling is given in the main datasheet. The UL-04-17-1 includes a micro-bolometer Focal Plane Array (FPA) comprised of 640×480 elements two-dimensional detector array made from amorphous Silicon resistive bolometer micro-bridges connected to a silicon ROIC (Read-Out Integrated Circuit), and a thermoelectric stabilizer (TEC), integrated into a miniaturized metal packaging. The UL-04-17-1 sensor produces raw analog video data up to 60 frames per second and is controlled using a serial link. Pixel pitch is 25×25 μm, and the image size is 16 mm by 12 mm (20 mm diagonal). Some general characteristics are given in Table 3.1.

3.1.1 Performances provided by ULIS

ULIS delivers its micro-bolometers with some warranted parameters, disclosed in a specific data sheet STR (Specific Technical Report) is sent for each unit. These tests are done in the following test operating conditions: Typical FPA temperature of 30° C (with ±10 mK stability). The background temperature is 20° C. The output rate at 8 MHz (for 50 Hz of frames per second) with two outputs. Furthermore, all the electro-optical parameters are defined and measured with a $F\sharp = 1$ (F-number equal to 1) optical aperture condition. The useful scene temperature dynamic range at the detector window level is, at least, 60° C. Measurement nominally from at least −10° C to +50° C which corresponds to an electrical dynamic range of 3.2 V, with the output voltage swings between 1.0 V and 4.2 V. The dynamic range can be increased when decreasing GFID bias value from the recommended value given in the specific STR but, have to take in account the change in the NETD (Noise Equivalent Temperature Difference) performance. The voltage values for $GFID$ and VSK are given in the STR data sheet for information only.

Some variable data prefixed that are analyzed in the tests are the following (This is also tested by ULIS and reported in the STR):

Temporal NETD – For a 50 Hz frame rate, the 300 K average temporal pixel Noise Equivalent Temperature Difference (NETD) of all operating pixels is better than 120 mK.

Responsivity – ULIS gives a responsivity value typically about 5 mV/K. This parameter is given in the STR, slightly different for each detector. The responsivity mean value is calculated on the operating pixel population.

Operating Point: Biases Adjustment –

The operating point depends on:

1. Tuning of the detector: $VFID$ (gain), $Vskimming$ (Offset), and $Capacitance$ (CTIA gain).
2. Integration time.
3. FPA Temperature.

3.2 Test Setup

This section describes the laboratory, the equipment used on these tests, and the methods and dedicated parameters to be evaluated [Morales de los Ríos et al.].

3.2.1 The IAC-LISA laboratory

The Instituto de Astrofisica de Canarias (IAC) has designed and built a global facility to test astronomical and space arrays and related devices, such as entire cameras or generic control electronics to handle one detector under the performed tests. This new facility, known as LISA, is located in the institute headquarters in La Laguna (Tenerife), where the main facilities are installed. Currently, LISA is able to characterize the main figures of merit of devices working in the visible range (such as the conversion factor or gain, readout noise, linearity, saturation levels, charge transfer efficiency, pixel response non-uniformity, fringing, dark current, cosmetics and, of course, the quantum efficiency, probably the most critical subject in this kind of devices). The test bench is a fixed facility fully equipped mounted in a 25 m^2 clean area, where almost any of the procedures are entirely automatized

using well-known SW standards tools (as NI-LabView and MATLAB). The figure 3.1 is a picture of the LISA laboratory [Morales de los Ríos et al.].

Figure 3.1: Picture of the IAC, LISA laboratory.

In order to carry out tests under different ambient well-controlled temperature, we use a $2\times2\times2$ m^3 Dycometal series 2604, climate chamber, with a temperature range from $-20°$ C to $80°$ C, controlled with an accuracy of $0.5°$ C, and relative humidity controlled range from 15% to 98%. All the test presented here were carried in the LISA laboratory and in the climate chamber seen in figure 3.2, in the IAC headquarters [Morales de los Ríos et al.].

Figure 3.2: Dycometal climate chamber for the ambient controlled tests

3.2.2 The INO IR-Camera

The IRXCAM-640 core [21] is a module developed to handle 640 × 480 pixels microbolometer FPA as the ULIS UL-04-17-1 chip. Providing 16 bits raw signal outputs at 60 Hz, the electronics give total access to the detector configuration parameters. It incorporates the TEC control and the micro shutter control. Only a few bolometer performance settings have been disabled (for instance, readout windows area or change the Master Clock frequency). The electronics show a low level of noise, much lower than the detector's noise level. The IRXCAM software controls the detector and displays the image acquired, and it also calibrates and characterizes the IR camera. The IR camera core, providing a 16 bits raw signal output at 60 Hz, is specially designed for developers thanks to total access to the

detector configuration parameter. Figure 3.3 is an image of the IRXCAM-640 indicating the main parts.

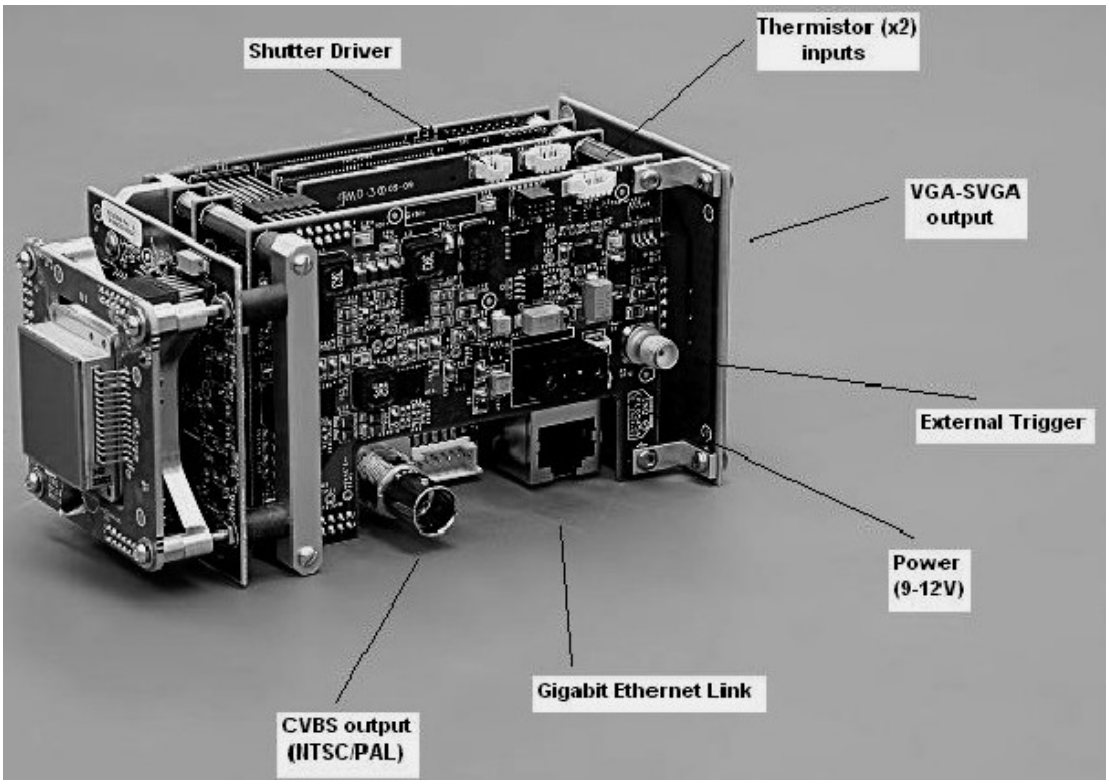

Figure 3.3: IRCAM-640 provided by INO

The controller is not a "camera itself" because there is no calibration in temperature, or well-defined optics, as in the usual thermal imagers. The main objective of INO is to supply versatile electronics to adapt different detectors able to configure the most important operating parameters (as voltages or on-module pre-processing) and, of course, fast prototyping. The output (control and sending data to the main platform) supports various formats such as $NTSC$, PAL, VGA, $CameraLink$, and $GigE$(Ethernet), although in our model, only the $GigE$ is available. Besides, it incorporates optionally (included in this case) the TEC control and the micro shutter control. Only a few bolometer parameters have been fixed by INO, and cannot be changed (for example, readout windows area or the master clock

Table 3.2: Main characteristics of the IRXCAM-640

Parameter	**Value**
Sensor	ULIS UL-04-17-1, 640x480 Pixels,
	25 μm pitch, LWIR 7 μm to 14 μm band.
Video output	Gigabit Ethernet link: RJ-45 connector.
Control output	Gigabit Ethernet link: system operation signals,
	parameters and calibrations tables loading.
FPA Operability	$> 99\%$
Frame rate	30 Hz or 60 Hz
NETD	< 65 mK
Power supply	+9 V to +12 V DC
Power consumption	≈ 6.5 W
Dimensions	$65 \times 59 \times 125$ mm
Weights	≈ 250 g
Temperature requirements	$-30°$ C to $55°$ C (operating)
	$-40°$ C to $80°$ C (storage)
Optional periferics used	External Trigger input (opto-isolated)
	TEC driver.
	Microshutter electronic driver.

frequency). In Table 3.2 main specifications of the IRXCAM-640 are displayed.

Regarding the thermal control of the FPA, the IRXCAM-640 architecture favors TEC less operation (from $-30°$ C up to $+55°$ C) for optimum system efficiency (lowest power consumption). For applications requiring an accurate FPA thermal stability, the module provides the FPA temperature value used to control the Thermo Electrical Cooler (TEC) already integrated into the FPA package. With this module, it is possible to vary and set the FPA temperature in the range [$+8°$ C to $+30°$ C], with a precision in the voltage to temperature sensor of 10 mK. Another option included in

Table 3.3: Main characteristics of the SURNIA optics

Parameter	**Value**
Image Diagonal	21 mm
Stop Size	26.4 mm
Stop Position	22.9 mm
BWD	35.6 mm
Flange to F.P	39.4 mm
Focal Length	25 mm
F#	0.86
Wavelength	$7 - 14$ μm
Circular FOV	45°
Transmission (Typical)	95%

our IRXCAM-640 module is the micro shutter electronic driver integrated to get offset images. The infrared thermal imagers are optics-dependent for their calibrations. In fact, all the parameters reported by ULIS (and also by INO) for their devices are referred to as a configuration of a f-number (or F#) equal to 1 as a typical value. The most important merit figures (as the NETD, for example) are F# dependent (relation between focal length and aperture). A very simple trade-off was made to choose a commercial objective to adapt the IRXCAM-640 module for the tests. Finally, we decided to acquire a SURNIA Lenses from Janos (main characteristics can be seen in the table 3.3), with a focal length equal to 25 mm and F# equal to 0.86 (faster optics than the used by INO and ULIS in their tests). This lens will maximize the amount of energy transferring to the detector. The IRXCAM-640 manufacturer provided the mechanical mount to adapt this lens to the device.

3.2.3 Hardware Setup

These tests' hardware involves a series of laboratory equipment that includes: the IRXCAM-640 with the micro-bolometer to be characterized as the detector (explained before), the target Black Body (BB), and equipment to control and monitor the camera and ambient temperatures during the tests.

The target

The BB selected for these tests has been the DCN-1000-L3 model from HGH Systems Infrarouges (France) [22]. This BB consists of an emissive head equipped with thermoelectric coolers whose heat dissipation is ensured by a refrigerated liquid, supplied (glycol water) by a separate cooling liquid unit, and circulated through a jacket at the back of the thermoelectric coolers. The minimum temperature is -40° C in absolute mode. This is not far from the lowest temperature requested for the microbolometer. To avoid dew condensation on low-temperature surfaces, the system includes several options such as sweeping dry gas on the emissive area, with an attached mounting, desiccant, and sleeve. The emissive head also includes a target support. To carry out some NETD tests, two infrared 8 μm to 14 μm targets (Half-Moon type, and four-bar vertical type) were acquired to be placed in front of the cold BB. Both the target and the emissive surface temperatures are measured in real-time thanks to high precision calibrated Pt sensors. The electronics can be handled via a touch screen panel or by an Ethernet communication link. The main characteristics of the BB are displayed in table 3.4, and figure 3.4 show a picture of the BB.

Table 3.4: Main characteristics of the HGH DCN-1000-L3 Black Body

Parameter	**Value**
Emissive area	75×75 mm
Absolute Temp Range	$-40°$ C to $150°$ C.
Thermal Uniformity	$0.01°$ C.
Emissivity	0.98 ± 0.02.
Regulation Type	Real Time PID.
Stability	$0.002°$ C.
Temperature sensor	Calibrated Pt probe.
Temperature accuracy	Differential $0.01°$ C.
	Absolute $0.03°$ C.

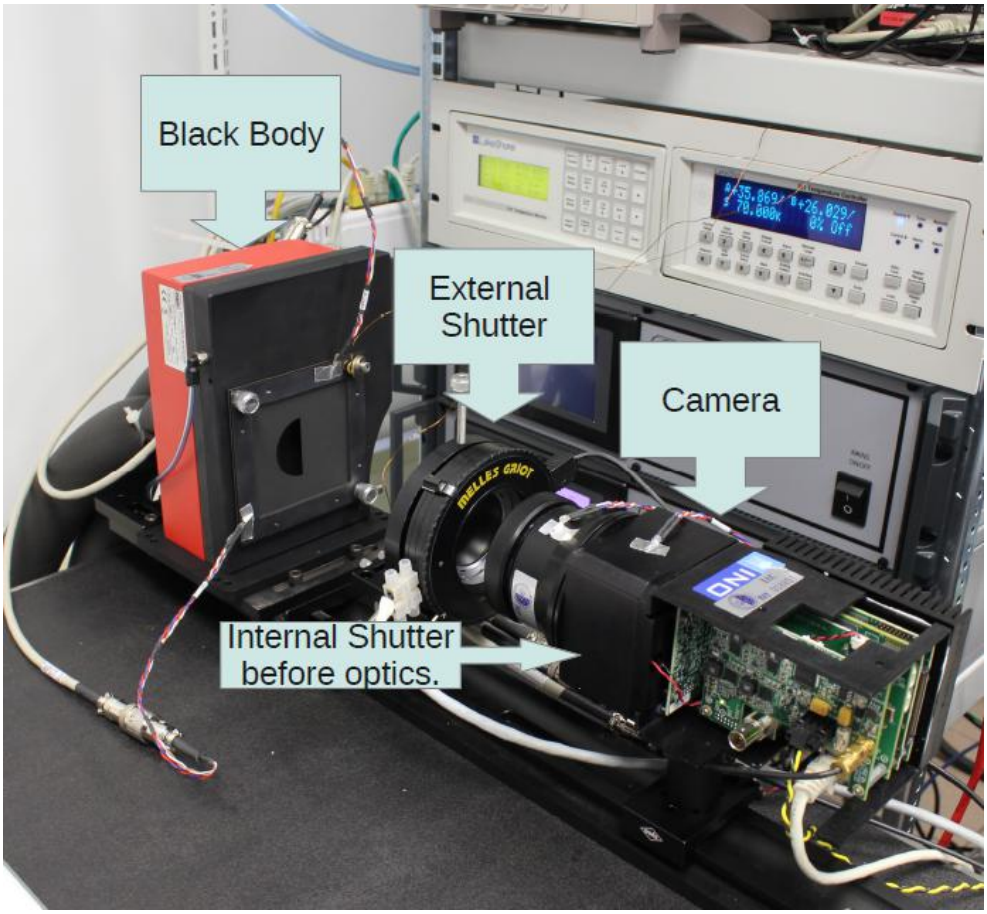

Figure 3.4: Characterization tests setup

Monitor, control of instrument and room temperatures

To carry out temperature and control measurements, the LISA laboratory has several typical temperature devices manufactured by Lakeshore, as the model 218, with 8 channel monitor or the model 331, with 2 channel monitor and control. The "Soft-Cal" calibrated temperature sensors are of two types: (a) platinum resistors and (b) silicon diodes. In these tests, 2 silicon diodes connected to the Lakeshore 331 and 8 platinum resistors connected to the Lakeshore 218 were used. The Lakeshore laboratories calibrated the 2 silicon diodes, and I have performed a calibration exercise before the tests to calibrate the 8 platinum resistors, using the 2 silicon diodes as reference. The calibration error for the diodes is around 10 mK, and for the platinum, resistors are estimated to be around 20 mK. Figure 3.4 shows the IRXCAM-640 and BB with the temperature probes all around the instruments.

We have identified the need to measure the temperature at different points of the experiment. At least:

- The FPA micro-bolometer (given by the IRXCAM-640 control program).
- The temperature of the enclosure, camera body, and optics.
- The temperature of the BB emissive surface (given by the BB control).
- The target temperature (same or equal to the BB enclosure, given by the BB control), and the half-moon mask attached to the BB.
- The ambient temperature in the air surrounding the experiment.

Previous tests showed that the shutter temperature has great importance in the measurements. For this reason, we have developed a shutter case

temperature control, using 2 heater resistors, connected in parallel, of 10 W at 15 Ω, a LakeShore 331 temperature controller, and a calibrated diode as a temperature measurement device. With this control, we can stabilize the shutter case temperature within ±10 mK. Figure 3.5 shows the detail of the shutter case temperature control, and Figure 3.6 shows a schematic of the instruments involved in the tests and their connections.

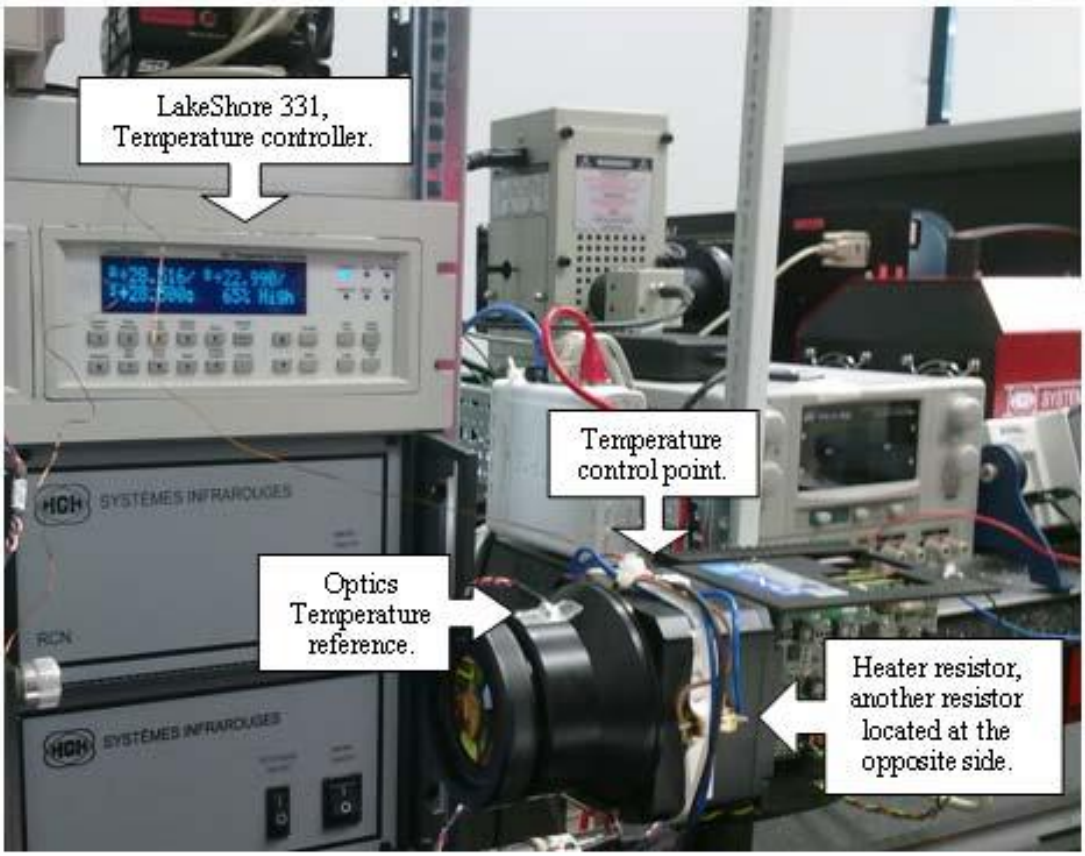

Figure 3.5: View of the shutter case temperature control system.

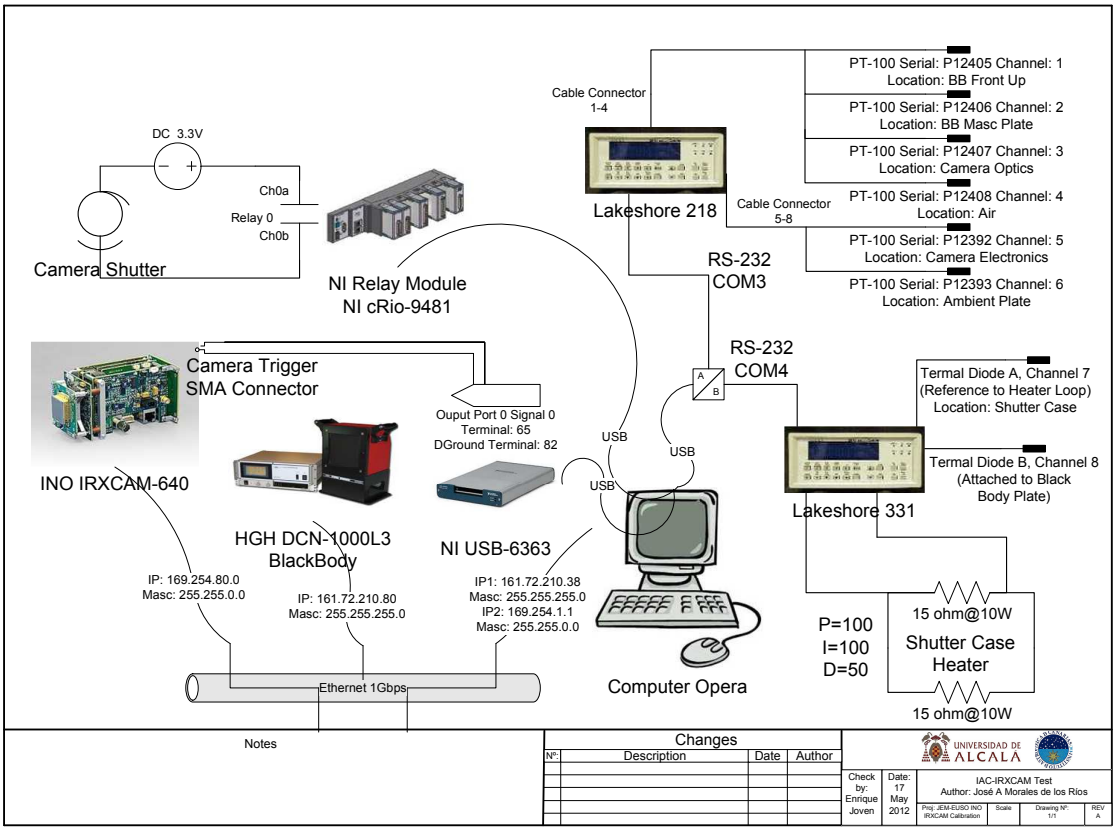

Figure 3.6: Blueprint of the test setup

3.2.4 Test Control Software

To carry out the extense series of tests, a general-purpose control program was fully developed and written using LabView (an image of the software's user interface can be seen in Figure 3.7). A scheme of the control logic can be seen in Figure 3.8. The design of this software and the control logic takes into account the need for the following characteristics:

- Synchronized control of HGH Systems Infrarouges DCN 1000L3 Black Body.
- IRXCAM-640 External trigger (TTL output/input, high to low flange) to acquire images. Provided by NI-USB-6343 device.

- External trigger (TTL output/input) to open / close a Melles-Griot external shutter (optional). Provided by NI-USB-6343 device.

- External switch to close relay (model NI-9481 device) to supply 3 V to the internal ULIS incorporated micro shutter's motor.

- Serial control of an 8-channel Lakeshore 218 temperature monitor, with 8 Pt-100 temperature resistor sensors (2-point calibrated, $\sim$ 20 mK accuracy).

- Serial control of a 2-channel Lakeshore 331 temperature controller, with 2 Silicon-diodes temperature sensors (2-point calibrated, $\sim$ 20 mK accuracy). Able to close a PI(D) control loop to thermalize the internal shutter + optics enclosure (less than $\sim$ 20 mK accuracy), using 2, 15 Ω, 10 W resistors connected in parallel (maximum $7.5 \times 2 = 15$ W, using the 1 A, 50 V internal source of the Lakeshore-331).

- Programmable delays between offset images (variable number), raw target images (variable number), the time between blackbody temperature setpoints (variable number), and time between offset and target images.

- Data output: FITS files, 16 bits raw data, separately offset and object images. FITS conversion up to 128 images per series (limited by the INO – program) from the CSV original format, keeping entire headers with default INO keywords plus values of all the temperature sensors added.

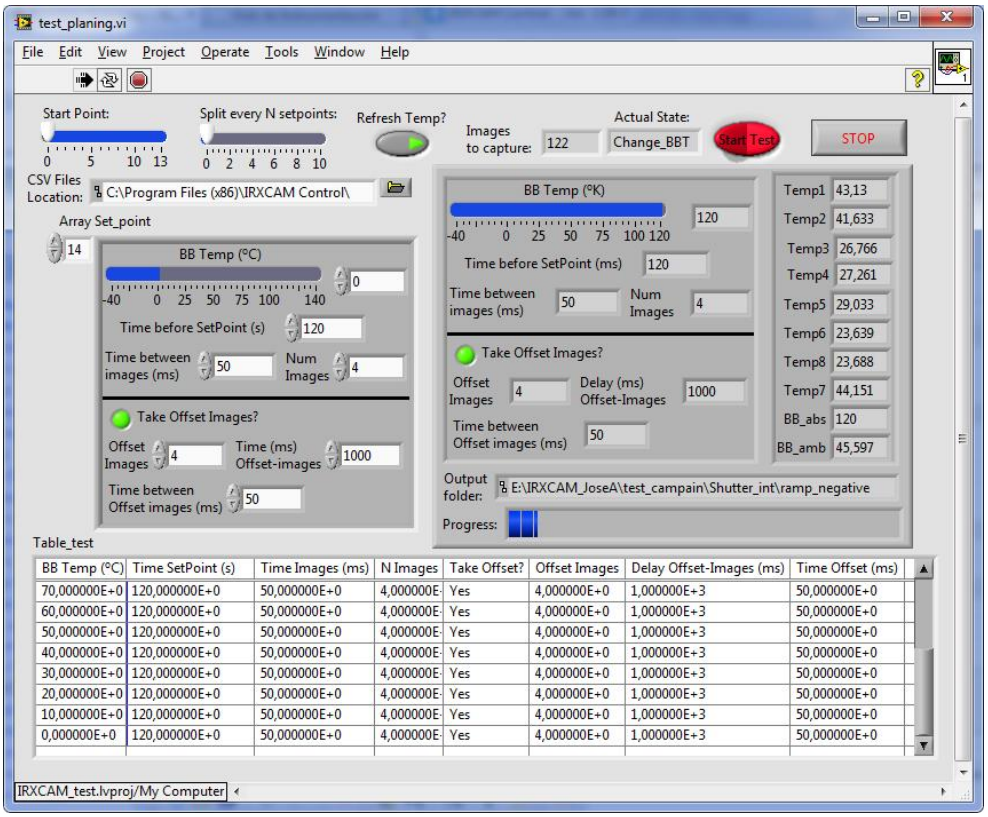

Figure 3.7: Graphical Interface for the Test Control Software developed.

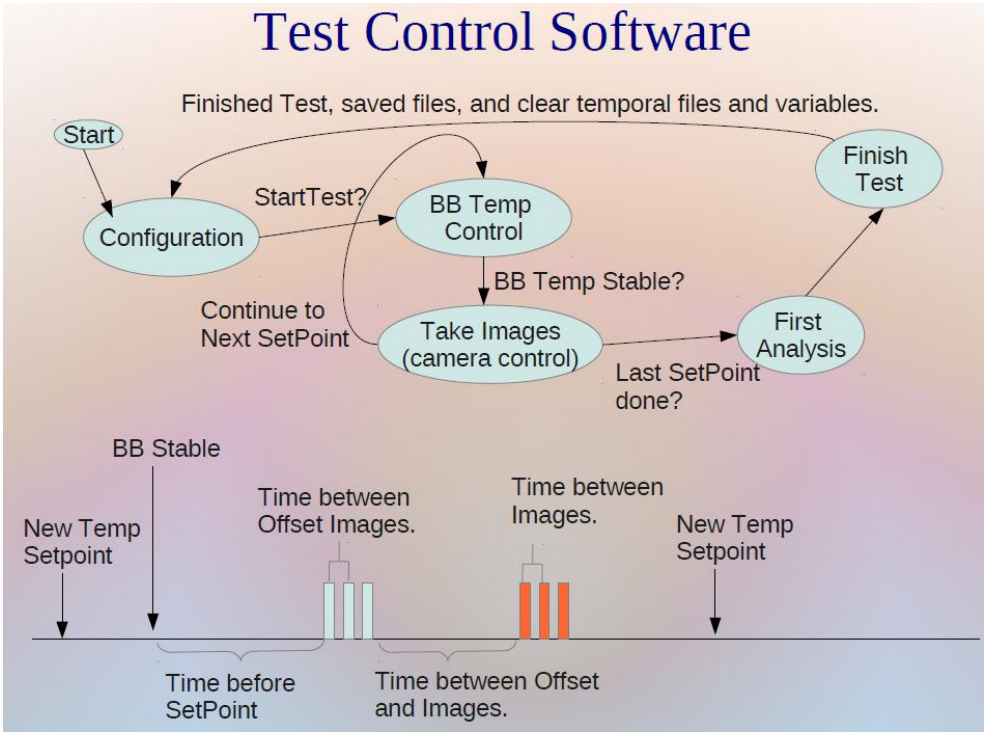

Figure 3.8: Control Diagram of the Test Control Software developved.

3.2.5 Parameters and variables of interest

The main objective is to characterize the micro-bolometer to be used for the EUSO space telescope IR-Camera. There is a series of variables related to the operation point, readout electronics, environmental conditions, and detector response that should be evaluated. Some of these variables are tuneable, and the impact on the detector response can be measured; others are fixed by the FEE design of INO. The main parameters involved in these procedures are summarized in Table 3.5.

Before starting with the tests, a series of trade-offs and laboratory measurements have been made to find the best gain and offset voltage values, maximize the responsivity, minimize the NETD, and ensure the full target range. Using our default couple of main values ($VGFID = 3101$ mV, and $VSK = 5315$ mV), if varying 200 mV the $VGFID$ voltage the improvement in the NETD is close to $\approx 20\%$ in the NETD value. So, we proceed first to vary a larger amount (over 0.5 V), but this new value saturates the camera's output (the A/D converters or the detector analog outputs). It is necessary to couple this tuning varying also the offset (VSK voltage). However, this voltage is limited to 5500 mV (both in the ULIS and, obviously, in the INO camera electronics). The final trade-off in the voltage values chosen for the tests was: $VGFID = 3351$ mV and $VSK = 5500$ mV. The value of $CTIA$ has been left unchanged ($CTIA = 1.0$) to reduce the number of variables in the trade-off. Figure 3.9 shows the change in the detector's response, with the factory setup, and the new values to increase the responsivity.

Table 3.5: Table of dedicated variables.

Group	**Parameter**	**Value**	**Comments**
FPA	VDDA	5 V (Fixed)	
voltages	VSSA	0 V (Gnd,Fixed)	
	VDDL	3.3 V (Fixed)	
	VSSL	0 V (Gnd,Fixed)	
	VBUS	2.8 V (Fixed)	
	GFID	0 V to 5 V	Gain (Tuneable)
	VSK	2 V to 5.5 V	Offset (Tuneable)
	VDET	0 V (Gnd, Fixed)	Fixed
	GSK	2.2 V (Fixed)	
INO	VOUT1-CM	2250 mV (Fixed)	Internal FEE voltage.
Voltages	VOUT2-CM	2250 mV (Fixed)	Internal FEE voltage.
	VOUT3-CM	1881 mV (Fixed)	Internal FEE voltage.
Clocks	MC	$>$ 8 MHz (Fixed)	Master clock
	INT	32.9 μs or 65.8 μs	(Fixed) Reading clock, for 60 Hz or 30 Hz
Control	Outputs	1 or 2	FPA reading channels (default=1)
Bus	CTIA gain	8 values	1, 1.152, 1.29, 1.5, 1.8, 2.25, 3.0, 4.5 (default=1)
	Flip output	(Fixed)	Right to left, and up to down.
	Window	1 (Fixed)	640 $\times$ 480 pixels.
Temperature	FPA	8.5° C to 30° C (Tuneable)	Temp of the FPA controlled by the TEC (default=24° C)
	FPA stability	10 mK (Fixed)	
	FEE, optics, & casing	-30° C to $+55$° C	Ambient, controlled
	FEE stability	$\approx$ 10 mK	
	Target range	-40° to $+140$° C	Black Body target temperature
	Target resolution	$<$ 120 mK (ULIS)	NETD $<$ 65 mK (INO)
Response	Output Range	1 V to 4.2 V	Fixed
	Responsivity	5 mV/K	Tuneable according voltages and operating point.
Data Out	Frame Rate	30 fps to 60 fps	Fixed to 1 or 2 channels.
Bits/pixel	16 bits	Fixed by FEE.	

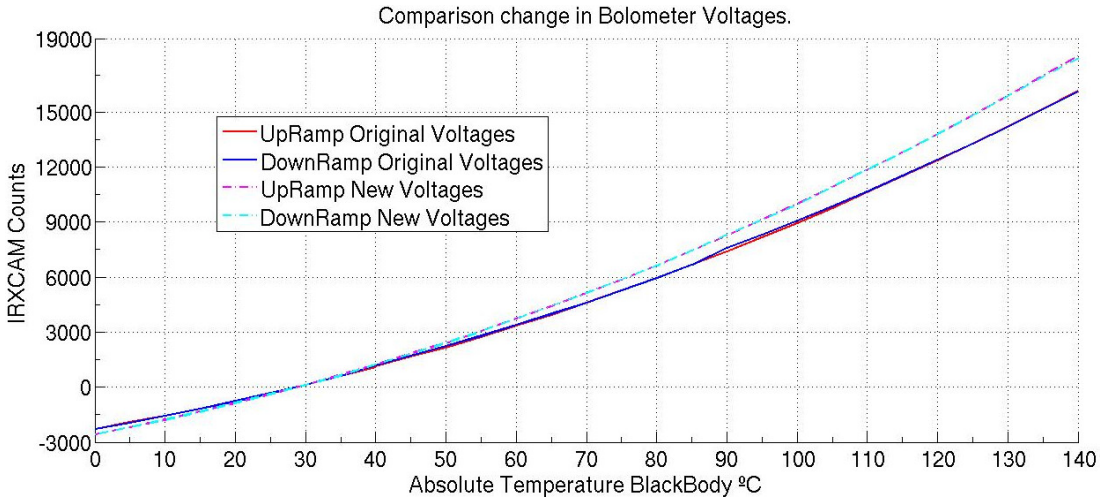

Figure 3.9: Detector response for the voltage set point change.

3.3 Test Procedure and Results

In this section, the micro-bolometer characterization tests and their results are discussed [Morales de los Ríos et al.].

3.3.1 Non Uniformities Calibration

As the number of pixels increases and their sensitivity improves, the image quality is increasingly dependent on a process called Non-Uniformity Calibration (NUC). As we know, a micro-bolometer imaging array is essentially an array of tiny resistors, and because of the micro-scale of these devices, there are variations in how each pixel responds to the infrared energy from an object. The response of the infrared camera's sensor must be normalized, meaning that the differences in response (gain correction) and DC output (offset correction) for the detector pixels have the same signal (or a minimal difference).

Summarizing, in front of a uniform scene, the signal is not the same for all the pixels. Possible corrections of the NUC:

- One point correction (n=1) is usually referred to as the offset correction.
- Linear correction (n=2), very good if the signal is in linear dynamic range. Most common.
- Polynomial corrections (n>2), only used if poor linearity or when the system requires very high performances.

The computation to correct the NUC has been obtained for each pixel 2 parameters, the slope (gain), and offset. Using the IRXCAM-640 as FEE, there is a step by step procedure to carry out this correction (or "calibration") in the IRXCAM-640 software. In this case, some limitations can be included, for example, a minimum and a maximum correction factor, or a minimum or maximum output voltage of the micro-bolometer. If some pixels' response is "out" of these limits, they are considered "non-operational pixels" and must be replaced by an average of the surrounding ones. The final result of this calibration procedure is an "RPLfile" that includes the gain matrix to correct all the pixels and the "replaced pixels". This table is loaded by the software and, together with the previously stored "offset" average image, allows for correcting the image (providing an optional output of 8 bit-data in the INO camera). However, we prefer to use the raw 16 bits output for this tests and made the corrections offline during the analysis of each image.

Gain matrix of the FPA

To calculate the gain matrix, the most common procedure is to set the temperature of the FPA (default, +24° C) and to choose two different tem-

peratures of the BB (one cold $\approx +10^{\circ}$ C and one warm $\approx +60^{\circ}$ C). These images would be the two necessary flat references, supposed linear microbolometer response in this range. The reference BB must be placed in front of the camera (including the optics). Enough images must be taken to average the two calibration points. We can compute the results using the IRXCAM-640 control software "Calibration Tab Procedure" or entirely offline.

There is a limitation with the instruments in these tests, the surface area (75×75 mm) of the BB is too small to focus the camera. So, PRNU (Photo-Response Non-Uniformity noise) files for calibration provided by the manufacturer (in this case, INO) have better behavior than our files. The INO provided PRNU files have to be used, until a bigger area BB is available, to correct the images. If the camera optics is not focused, the energy is not equal for the entire flat image (Figure 3.10, left part). The RPL-file provided by INO was obtained without optics. A new one should be generated in the same way, including the optics. However, the result will not change at all the previous results because we do not consider PRNU inside the image or cosmetic defects, rather good as tested by INO in their previous calibration.

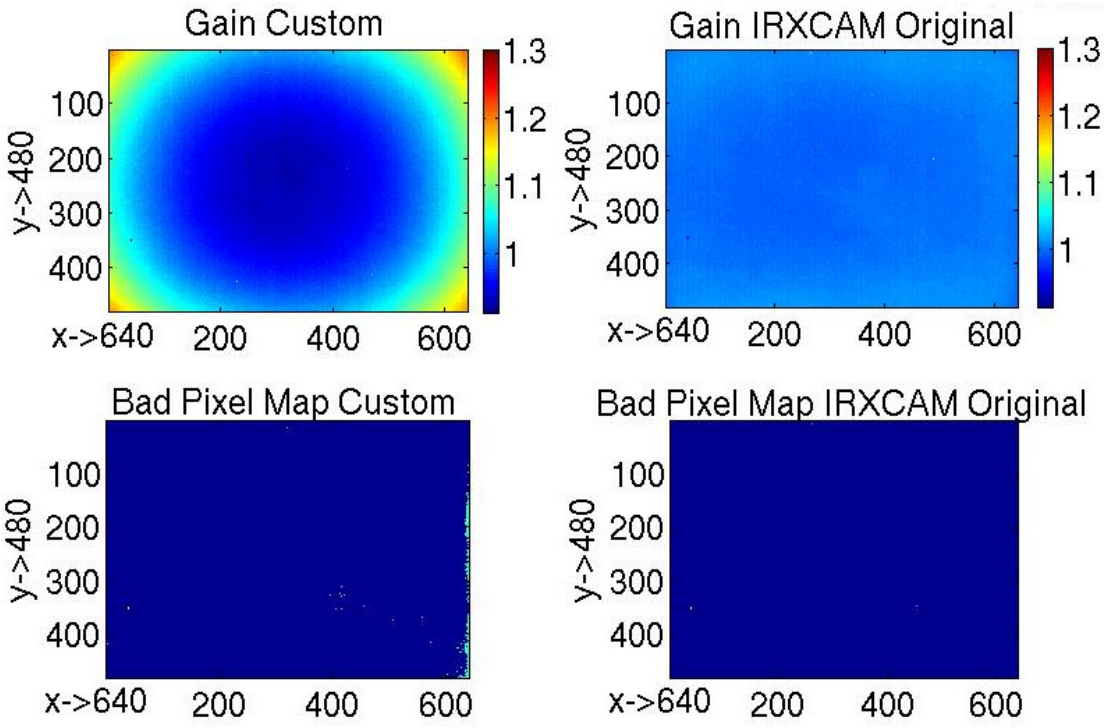

Figure 3.10: NUC Gain and bad pixel matrix, test with not focused optics (left), and INO RPL file data (right).

Offset; Internal or External shutter.

There is a strong dependence of the offset level in the micro-bolometer signal (basis) with the time, mainly due to external radiance influences, temperature variations in the environment, and other factors. Figure 3.11 describes the importance of the offset graphically.

The detector output voltage is composed of:

- Signal coming from the scene
- Signal coming from the camera temperature variations (mainly optics and detector casing).
- Offset coming from the FPA temperature variation
- Offset coming from pixel non-uniformity (PRNU or NUC)

Although, only the signal coming from the scene is of interest. The following actions are needed to extract from the micro-bolometer output the signal coming from the scene:

- Image obtained with a stable camera temperature
- Shutter actuation
- Image obtained with the shutter closed, to correct the FPA temperature variations, and the pixel non-uniformity (the correction of the FPA temperature variations is only possible if the shutter temperature follows the same variations, or if the shutter is outside the camera and stable in temperature).
- Camera and optics temperature monitoring data.
- Corrected image from camera temperature drift for analysis.

Figure 3.11: Graphical explanation of the offset paper in the micro-bolometer based IR-Cameras.

For the best correction, on a first approach, experimented with an external shutter to have a reference value to correct the FPA temperature variations, the pixel non-uniformities, and the camera temperature variations. However, in this case, have found that (Figure 3.12), the variation of the ambient temperature over the external shutter (as the external shutter

is not controlled in temperature) produces a variation in the reference to be subtracted. If the tests go slower, results improve (due to the thermal inertia), but there is a clear "hysterics" effect. Shutter shall be internal, as close as possible to the optics, and with its temperature as stable (or actively controlled) as possible.

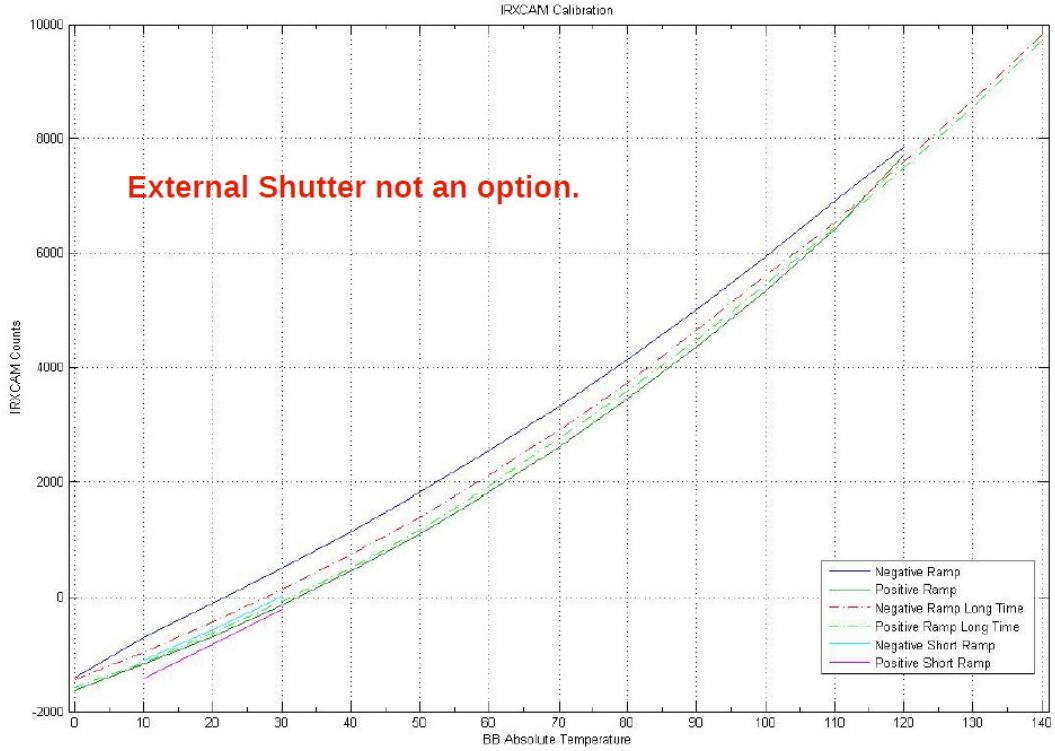

Figure 3.12: Behavior of the IRXCAM-640 with an external shutter.

As explained before, bad results lead me to discard the use of an external shutter, and use the internal shutter installed between the camera optics and the ULIS detector.

In figure 3.13, I have operated the camera using the internal shutter and plot the detector response. Up ramp and Down ramp fits rather well. The shape of the curve is as expected.

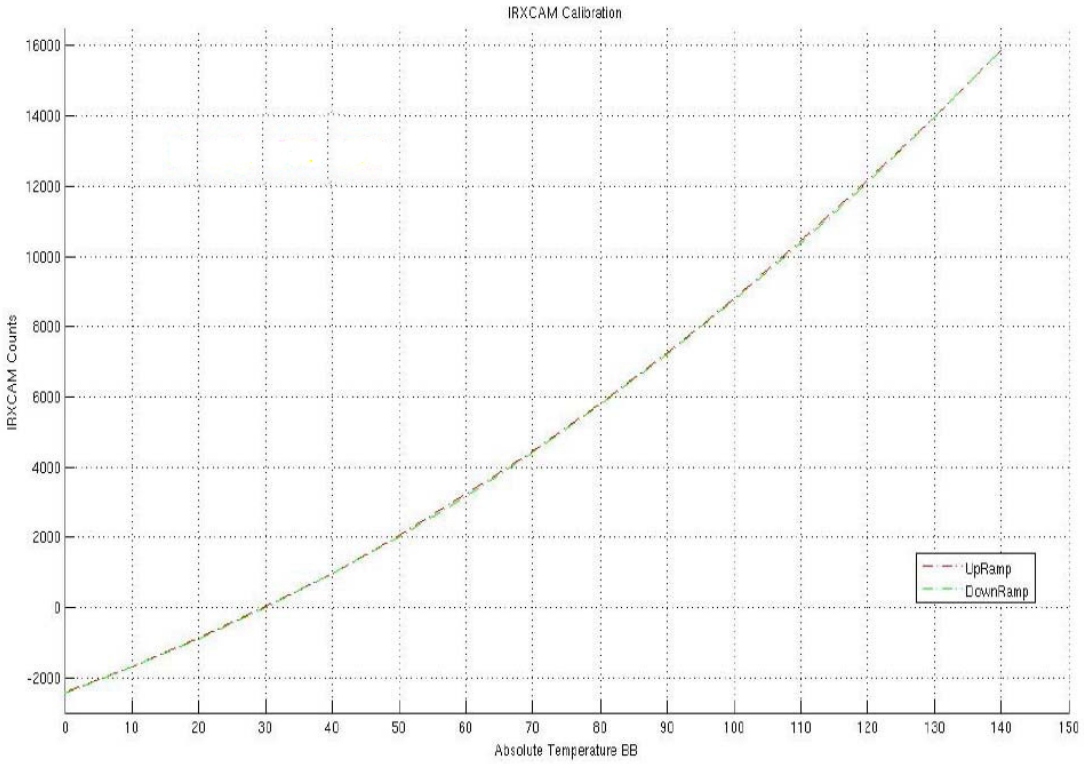

Figure 3.13: Behavior of the IRXCAM-640 with an internal shutter between the optics and the detector.

In order to check the behavior of the system with the environment temperature (mainly the offset behavior and shape of the calibration curves), we have also measured the behavior of the system inside the climatic chamber, with the following working conditions:

- $VGFID = 3351$ mV and $VSK = 5500$ mV (optimized voltages)
- FPA-Bolometer temperature: +24° C (default)
- Ambient temperature at: (a) 0° C; (b) +15° C and (c) +30° C (room temperature) with a humidity value for $HR \approx 15\%$
- Shutter temperature and optics PID controlled (with ±10 mK stability) @ +12° C, +22° C and +34° C (Note: It would be necessary

more power to balance the environment temperature with the shutter reference for offset temperature).

- Frequency in the image acquisition = 30 Hz (30 fps, entire 640 × 480 pixels).
- First image of each series was discarded. I have discovered some type of "remanence" or capacitive effect in the bolometer (or, less probable, in the INO electronics camera), so the first image showed a slightly larger amount of signal.

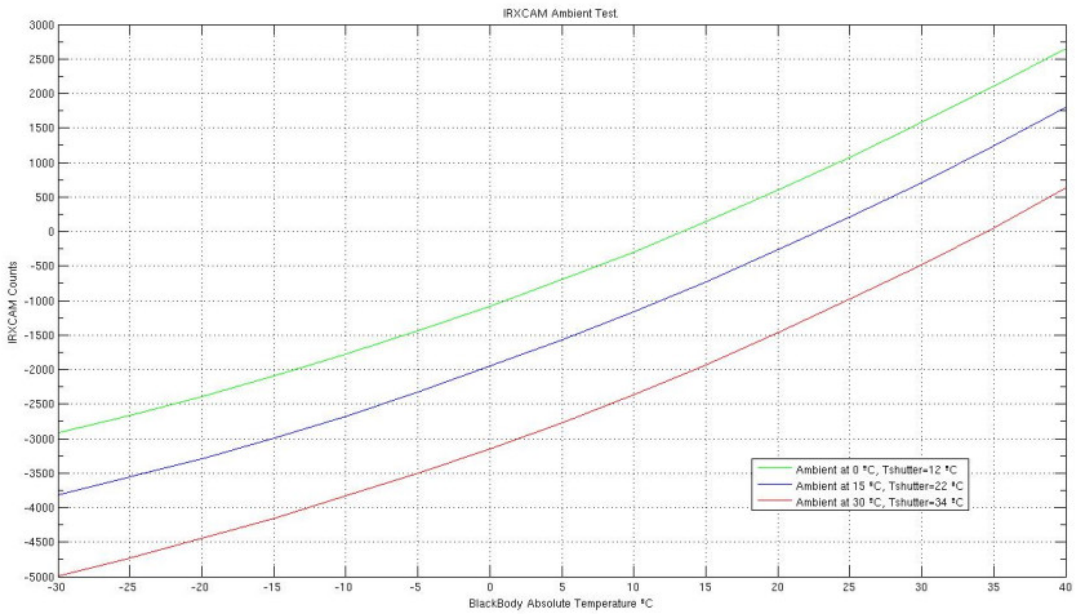

Figure 3.14: Shutter offset temperature influence, parallel curves are due to change in the shutter reference temperature.

It is worth to be remarked the relevance of shutter influence. The tests have measured identical calibration curves changing only a few degrees the reference temperature of the shutter controlled with the PID servo. As natural, curves are parallel due to the offset variation, but the calibration parameters should obviously change. It is impossible to keep the same value

for these temperatures, as is strongly dependent on the ambient because it is not entirely isolated from it.

3.3.2 Absolute calibration

Usually, commercial thermal images contain several Look Up Tables (LUTs) inside their firmware to save the different calibrations with the chosen parameters. Obviously, these options are limited to avoid an almost infinite number of possible combinations and calibrations. The main objective of the absolute calibration of a thermal image is to give the user a correspondence between the data output (digital corrected) and the real scene temperature (in °C or K). After the FPA is tuned around the requested operating point & dynamic range, we must check the response's linearity. This is an important subject for the calibration because only two points are needed for a straight line. If we request more accuracy, or the response in the requested dynamic range is not linear, we need to create an entire LUT (Look Up Table) to associate each digital value coming from the FEE to the real scene temperature.

We have measured the behaviour of our current system inside the climatic chamber (Figure 3.15), with the following working conditions ("working point"):

- $VGFID = 3351$ mV and $VSK = 5500$ mV (optimized voltages).
- FPA-Bolometer temperature: +24° C (default) (accuracy ±10 mK)
- Ambient temperature ≈ 22° C (controlled by the climatic chamber).
- Shutter case and optics temperature controlled with a PID servo (±10 mK stability) at +28° C.

- Frequency in the image acquisition = 30 Hz (30 fps, entire 640×480 pixels).
- First image of each series (series of 5 images for offset and target) was discarded. Because some type of "remanence" or capacitive effect in the micro-bolometer, the first image showed a slightly larger amount of signal.
- Offset subtracted in each set of images.
- F#= 0.86.
- Temperature of the Blackbody: from $-40°$ C up to $+140°$ C
- NETD $\approx$ 65 mK
- Integrating energy over the range from 7 μm to 14 μm (optics spectral range).

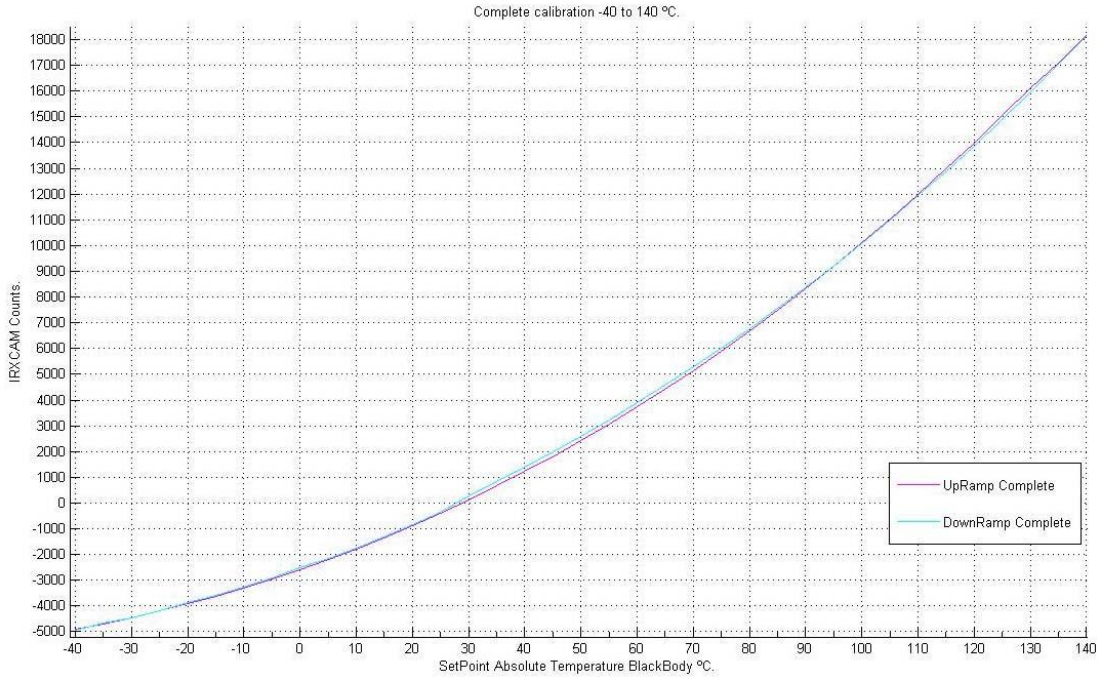

Figure 3.15: Complete range calibration test.

To evaluate the system, we can use the classical theory about blackbodies radiation. It is well known that a perfect blackbody (BB) emits energy as a function of the temperature and the wavelength, according to Planck's Law. The "total exitance" (M as f(T)) of the BB, integrating over the entire spectrum, is given by the Stefan-Boltzmann Law, where the exitance (energy) is proportional to T^4. The first approximation is to fit the experimental data with a curve of temperature to the fourth power and with the Plank law integrated from 7 μm to 14 μm. From figure 3.16 can be extracted that the best fit happens using only the above mentioned 7 μm to 14 μm range. Such fit is rather good, indeed at high temperatures, where the fourth power fails. If we want to use a simple polynomial adjustment, it is possible to fit a better curve in this region varying slightly the temperature exponent ($\approx T^{3.6}$), over the entire spectrum.

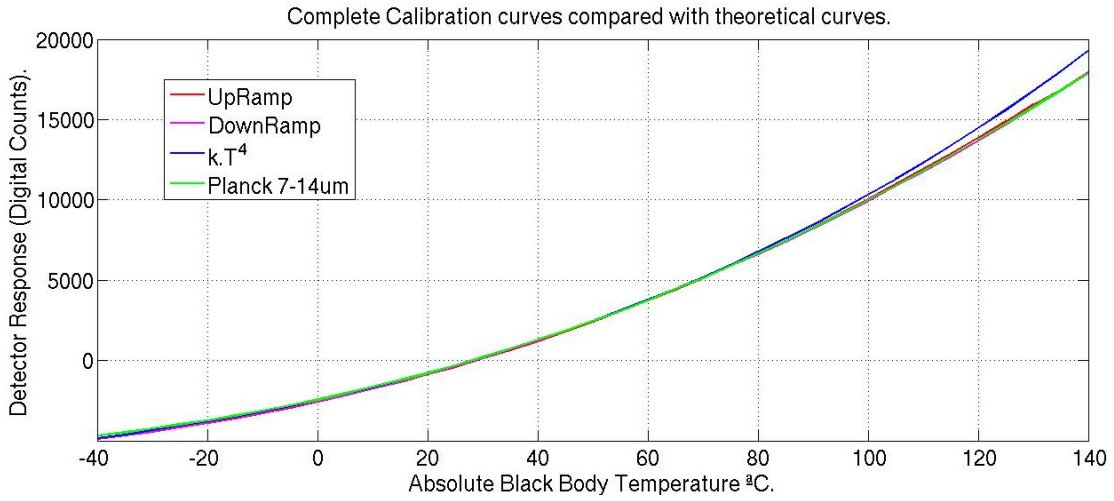

Figure 3.16: Complete range calibration test compared to theoretical Planck curves.

Meanwhile, we are interested in fitting a linear response using the energy (irradiance over the array or the equivalent radiance coming from the source target) versus the microbolometer's output response. To do this, we must integrate Planck's blackbody radiation function in the area of interest (in

our case, from 7 μm to 14 μm) using, for example, the approximation given by Widger and Woodall [23]. After these calculations, we get the response as a linear function of the calculated radiance (Figure 3.17).

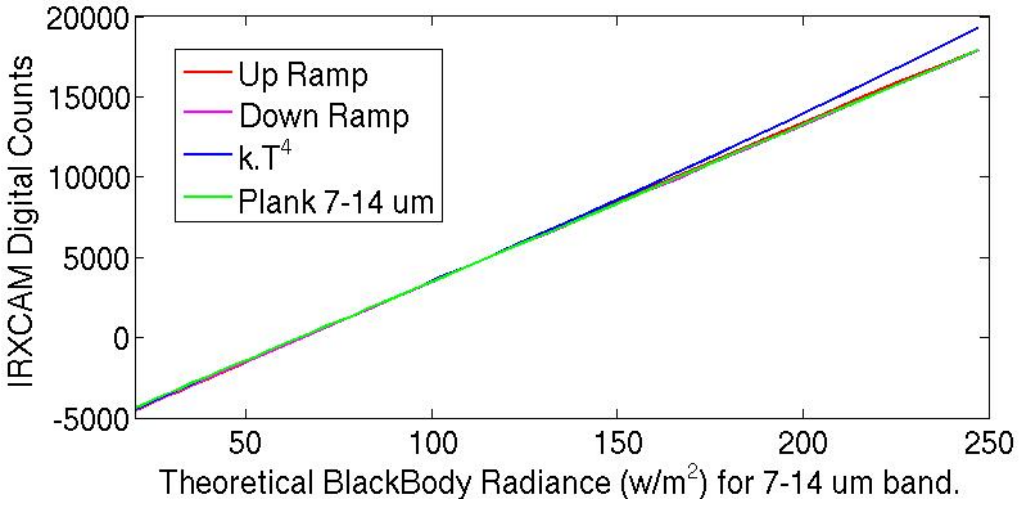

Figure 3.17: Detector response vs Planck theoretical irradiance.

At room temperatures, we get approximately a value of 11.3 mK/counts (885 counts in [20° C to 30° C] range) for this set of default values. This is the first approximation for a calibration o reduced LUT (Figure 3.18). Using this, it is possible to get a rough calibration for the camera in our test setup. For example, the human face, we have taken a real image (Figure 3.19) with the ULIS + IRXCAM-640 camera. However, it has to consider the skin emissivity that is lower than the 98% of the BB emissivity.

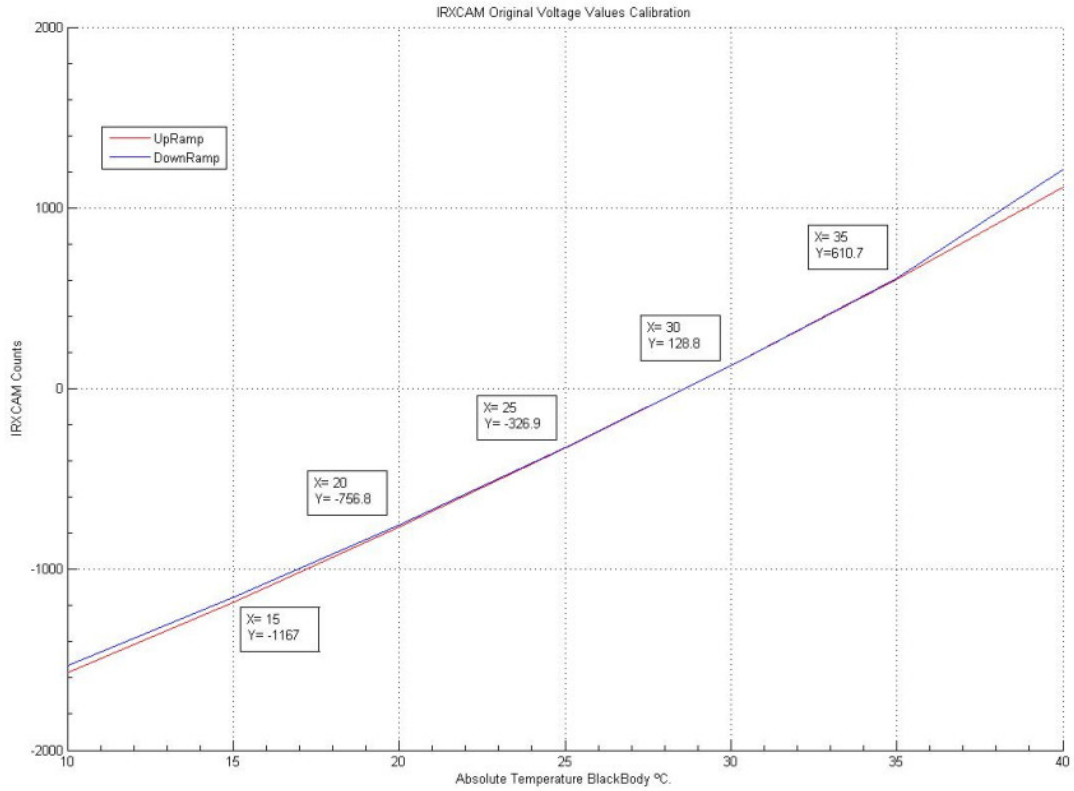

Figure 3.18: Calibration values at room temperature.

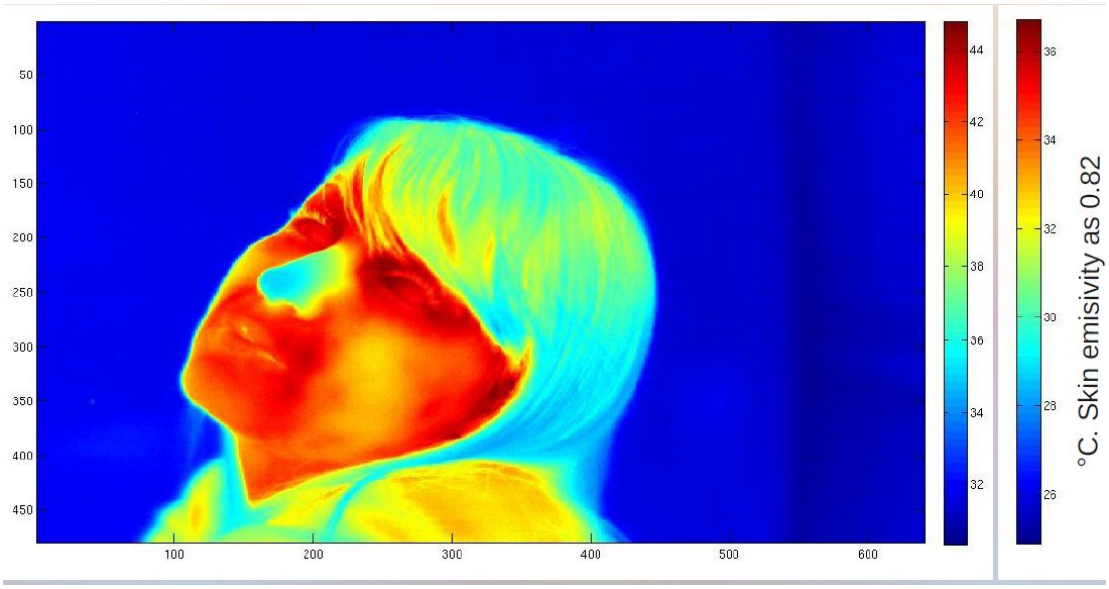

Figure 3.19: Test of the IRXCAM-640 with a human face.

From the previous tests, we have obtained some curves plotting the detector's response vs. the temperature of the target blackbody, in the available range of [−40° C to +140° C]. Although the plots are not linear, the ob-

tained results are as expected. The micro-bolometer is linear according to the incoming energy (irradiance over the detectors' surface). So, it is necessary to transform temperatures of the BB into radiance/irradiance values to check the goodness of the linearity detector. Calibration should be done in a similar way. To limit the huge amount of parameters involved, we have used optimized voltages for the micro-bolometer. With these values, we get the best NETD possible (see section 3.3.3), although the dynamic range shrinks a bit (which is not very important for our requirements). Of course, there is no chance to tune the voltages according to the different wavelengths because of design constraints, as images will be composed of both wavelengths. To avoid previous confusions, we must add that the micro-bolometer integrates energy using the whole responsivity range, and this range fits rather well with the optics used (from 7 μm to 14 μm).

3.3.3 Temperature resolution and NETD

The temperature resolution is one of the most important figures of merit in infrared thermal devices. Usually, it is evaluated as the Noise Equivalent Temperature Difference (NETD). The NETD is the scene temperature difference equal to either the detector's internal noise (detector NETD) or the total electronic noise of a measurement system (system NETD). In this case, as I can not separate FPA and FEE (IRXCAM camera), we will evaluate the system NETD. The classical and conventional test setup is rather simple. It consists of temperature control BB reference and some ambient (passive) object that creates a simple "slit" target for the camera to visualize. The temperature of the BB is adjusted until it nearly equals the ambient target temperature.

In our case, it is effortless to place our "half-moon" target in front of the BB and change the temperature of it until the image disappears from the camera screen control program. The BB controller reports both room and BB temperatures. Besides, some additional temperature sensors can be placed. This is the way to get a "quantitative" measurement of the system NETD. However, the evaluation of the NETD is rather difficult within the specifications (with the accuracy required less than 50 mK). Using the half-moon target, these classical tests are challenging because small variations of the BB induces small variations in the surrounding air, varying the ambient temperature. After many attempts, the results' uncertainty was substantial. To evaluate the NETD, two alternative methods have been used.

NETD evaluated using small steps increments of the BB temperature.

To avoid the problems of stability before mentioned, I have programmed several ramps of setpoints (with small increments of 10 mK) in the BB emitting surface, getting groups of offset and raw images (usually 4 of each), in order to average and plot. In this plot (Figure 3.20) there are some strange artifacts; some flat "stairs", probably due to the lack of time to stabilize the entire BB surface, changing every 10 mK. However, the "noise" in the small temperature steps is no more (peak to valley) than 5 counts (using the same default values of temperature and voltages). Therefore, over 5 counts $\times 11.3$ mK/counts is equal to ≈ 56.5 mK. Nevertheless, this is not an accurate test. New tests were carried out in order to avoid these spurious steps (Figure 3.21), waiting for enough time to stabilize the blackbody (which accuracy is over ≈ 2 mK only), and isolating the internal shutter from the environment, as it was explained before. With the PID servo control loop implemented,

this implies, in principle, a very stable offset reference to subtract the target images.

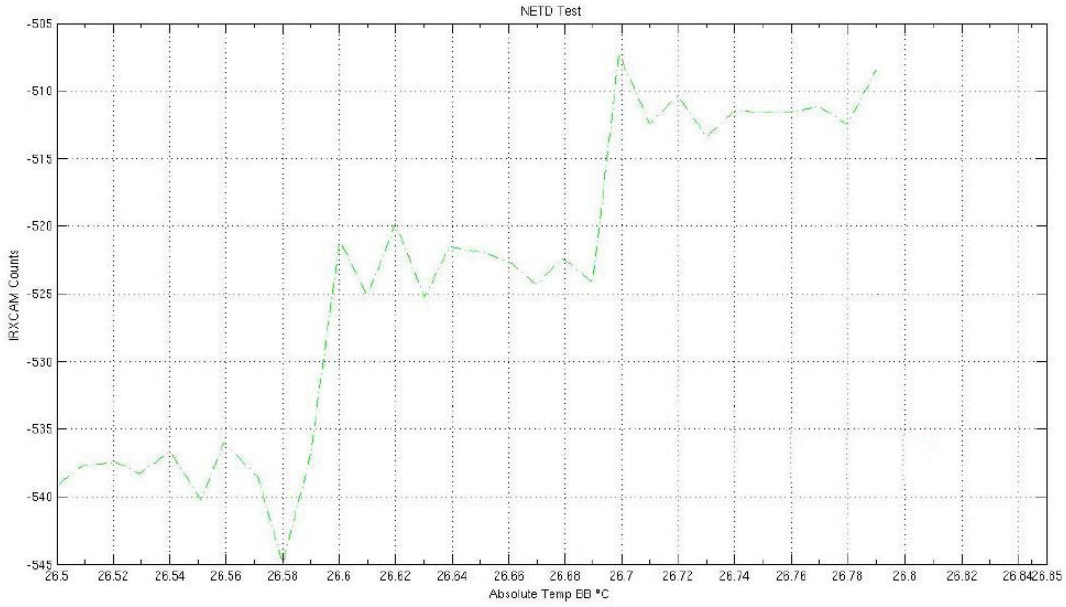

Figure 3.20: NETD evaluated using small steps increments of the BB temperature.

In this new plot (Figure 3.21) we present at the same time the evolution of the PID-stabilized temperature of the shutter and also the optics (attached to the same aluminum temperature-controlled case). Variations are minimum, within ± 10 mK on average. In the Y-axis plots, we show these temperatures and the IRXCAM counts too, and as in the previous plot, X-axis is the evolution of this signal with the target's temperature. As I have added a small delay to improve the BB plate's stabilization, previous stairs are almost disappeared. The only artifact that remains is larger spikes, probably due to the long time to measure needed (drifts of the system or EMC isolated problems). As before, common "spike-noise" are over 5 counts. To get this plot, 5 offset images plus 5 target images have been taken at each BB temperature point (every 10 mK). Each group's first image was always discarded, as shown a slightly larger signal, probably due to

some remanence or capacitive effect of the micro-bolometer.

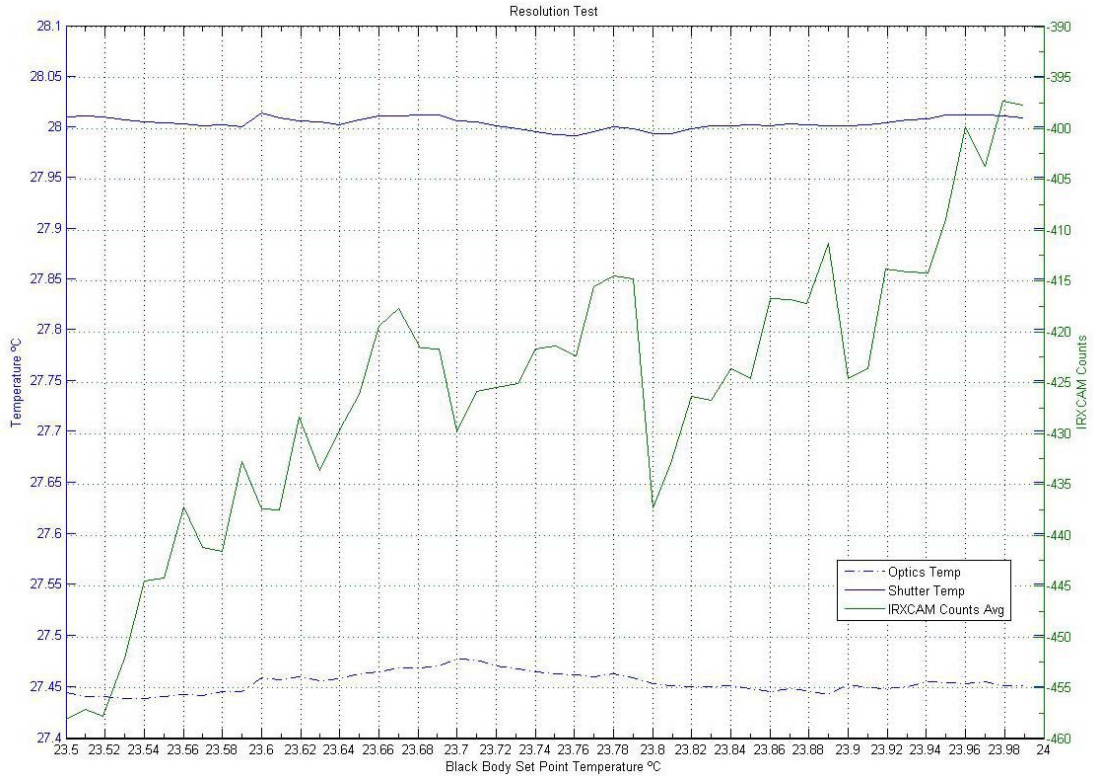

Figure 3.21: NETD evaluated using small steps increments of the BB temperature, with isolated and stabilized temperature for the shutter.

The NETD calculated according to statistical RMS noise.

To obtain more confident results for the NETD, the system's noise was evaluated in a classical way, averaging a small, medium, and a large number of offset images taken consecutively. With these configurations:

- $VGFID = 3351$ mV and $VSK = 5500$ mV.
- Temp shutter and optics PID controlled +28° C (with 10 mK stability).
- Frequency in the image acquisition = 30 Hz (30 fps, entire 640×480 pixels)
- First image of each series was discarded. Because of some type of

"remanence" or capacitive effect in the micro-bolometer, the first image showed a slightly larger amount of signal.

- Long series of images (100 images) of the controlled temperature shutter. Analyzed in groups of 4, 50 and 100 images.

- Repeat the tests for several micro-bolometer FPA temperatures, available with the INO + included Peltier electronics: (a) 8° C (Figure 3.22) minimum; (b) 16° C (Figure 3.23); (c) 24° C default temperature (Figure 3.24); (c) 30° C (Figure 3.25) and finally; (d) 32° C maximum available temperature (Figure 3.26). In this last case, the stability was slightly worse than 10 mK in the bolometer, mainly in the first points of the series, so the values obtained in the NETD suffer and are a bit higher than the rest. As shown from the respective figures, the working temperature for the micro-bolometer is not relevant for the NETD values obtained.

Table 3.6 summarize the results of this test. It is important to remark here that the values given for the NETD in adus (Analog Digital units or counts) are valid. However, the conversion into mK (multiplying by the conversion factor 11.3 mK/counts) is temperature-dependent (the bolometer's temperature changes the calibration curve, as we have seen changing the offset). However, the variations in this temperature range (from +8° C up to +32° C) is minimal, and for example, data acquired at 24° C (default) should be realistic enough. This conversion factor obviously includes the F# (≈ 0.86 in our optics), as it is also a parameter for the configuration. Note $counts = adu$; these expressions are equivalent.

Table 3.6: NETD tests for several FPA temperature, analyzing different samples size.

Units	**FPA Temp**	**4 samples**	**50 samples**	**100 samples**
adus	8° C	4.39	6.07	9.68
mK	(Figure 3.22)	49.60	68.59	109.38
adus	16° C	4.64	6.19	8.98
mK	(Figure 3.23)	52.43	69.94	101.47
adus	24° C	4.89	6.22	9.10
mK	(Figure 3.24)	55.25	70.28	102.83
adus	30° C	5.46	6.97	9.63
mK	(Figure 3.25)	61.69	78.76	108.81
adus	32° C	6.16	6.88	9.50
mK	(Figure 3.26)	69.60	77.74	107.35

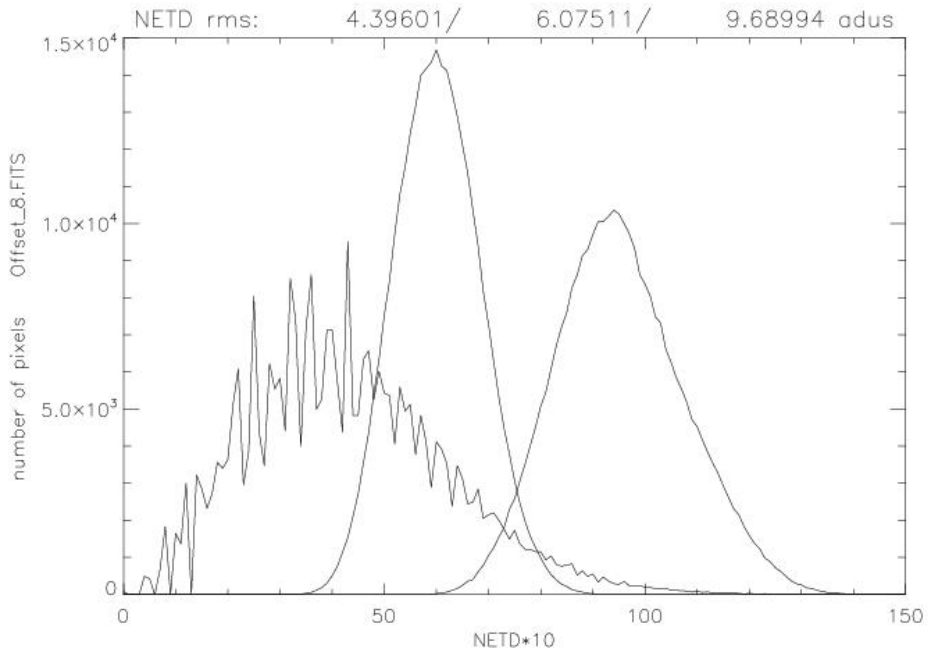

Figure 3.22: NETD test at 8° C, for 4, 50 and 100 samples.

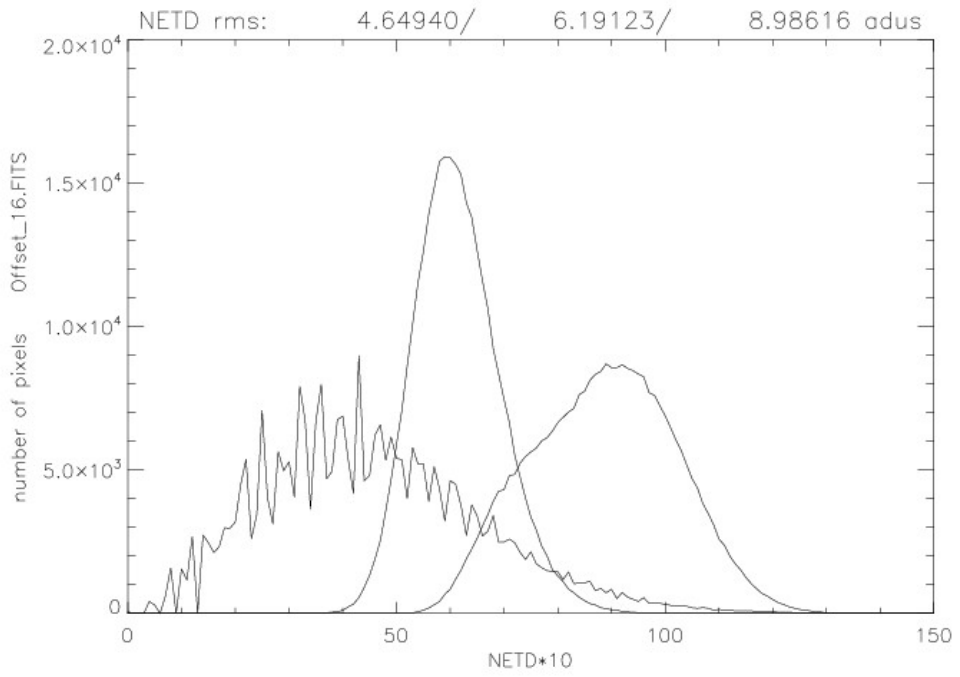

Figure 3.23: NETD test at 16° C, for 4, 50 and 100 samples.

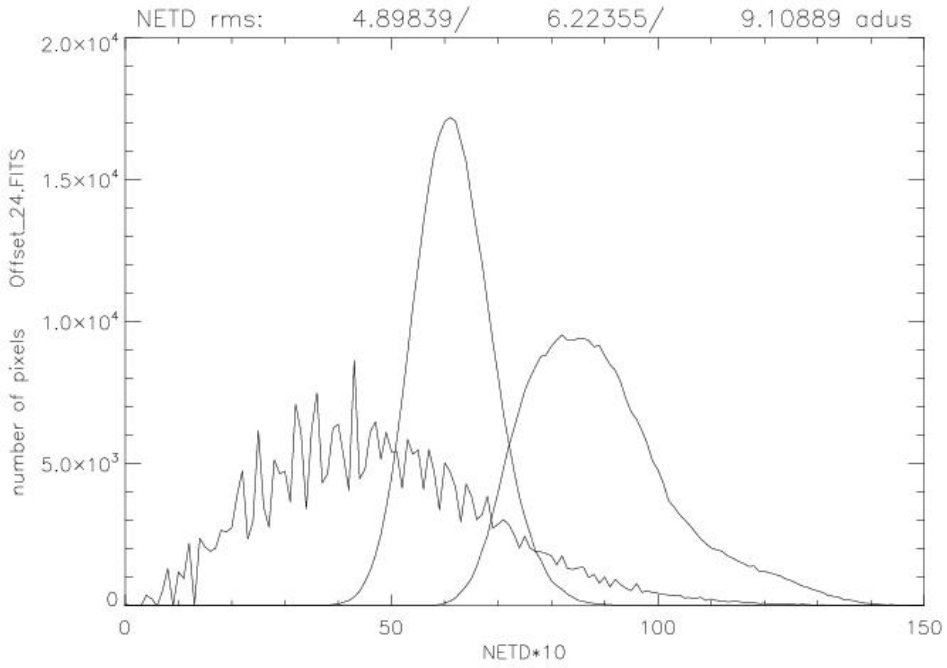

Figure 3.24: NETD test at 24° C, for 4, 50 and 100 samples.

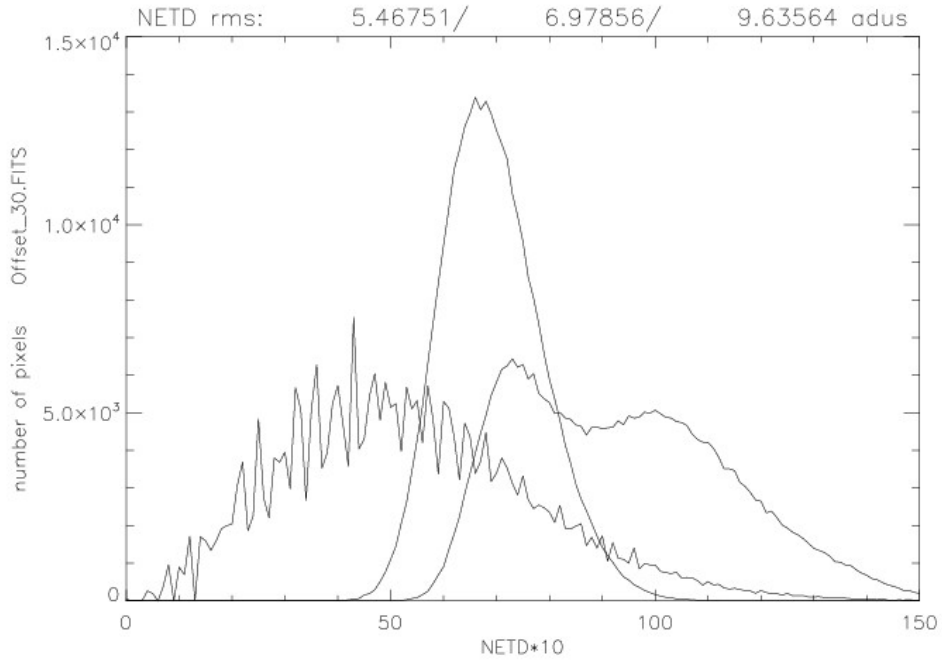

Figure 3.25: NETD test at 30° C, for 4, 50 and 100 samples.

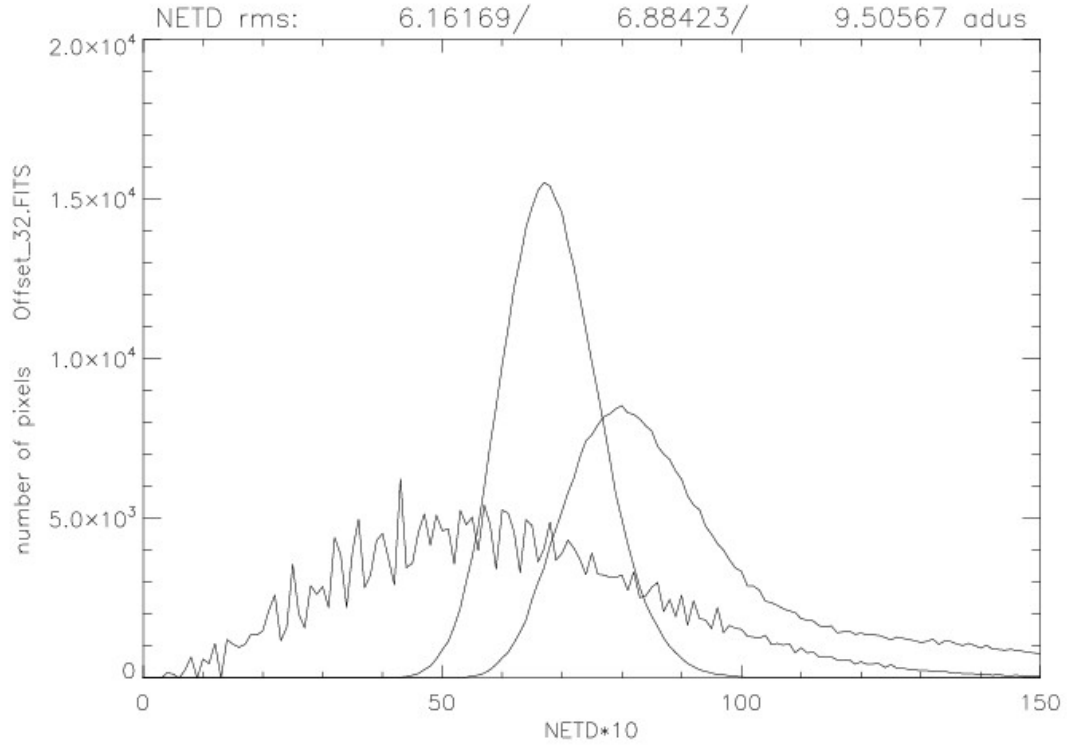

Figure 3.26: NETD test at 32° C, for 4, 50 and 100 samples.

It must be taken into account that, using filters with smaller bandwidths

over 1 micron, the amount of energy (signal or response in the bolometer) drops, and the NETD becomes worst in the same amount (considering variations over the signal with the same electronics noise).

3.4 Onboard Calibration Error Study

After setting a previously chosen "working point" involving voltages, optics, and temperature of the bolometer, the entire infrared camera must be calibrated using a couple of high-temperature blackbodies (BB) with predefined fixed temperatures.

Using the previously obtained curves of output response vs. BB temperature (target), a couple (or several) of points can be derived to calibrate. Obviously, after showing that the microbolometer's response behaves linearly according to the irradiance (energy). If this is the case, two points should be enough.

To evaluate the best choice for the fixed BB temperatures, I have considered a target temperature equal to $-40°$ C, the minimum temperature available with the experimental setup. After experimenting several iterations (Figure 3.27) with different couples of points (hereinafter "TL" as Temperature Low and "TH" as Temperature High) at high temperature (because power design constraints limits for Space will make feasible BB temperatures around $10°$ C to $40°$ C) in order to get the best couple (or minimum error measured in $°$ C, between the linear fit and the experimental value).

It is worth to be mention here that, in order to compare results, we must know the "transform factor" (or pure calibration, or a relation between degrees and counts from the camera) at the setting point ($@-40°$ C in this

case). This "transform factor" is got from the experimental curves as the slope (or the derivative $\Delta K/\Delta counts$, see equation 3.1).

$$\Delta K/\Delta counts = dT/dR(T) \tag{3.1}$$

R(T) is the micro-bolometer's response as a function of the temperature; obviously, these values change if we select another "working point". In our case, we estimated a value of 11.3 mK/counts for $+28°$ C and 22.1 mK/counts for $-40°$ C in this case. To get the best couple of calibration points, I have carried out several fits using the radiance vs. output response plots.

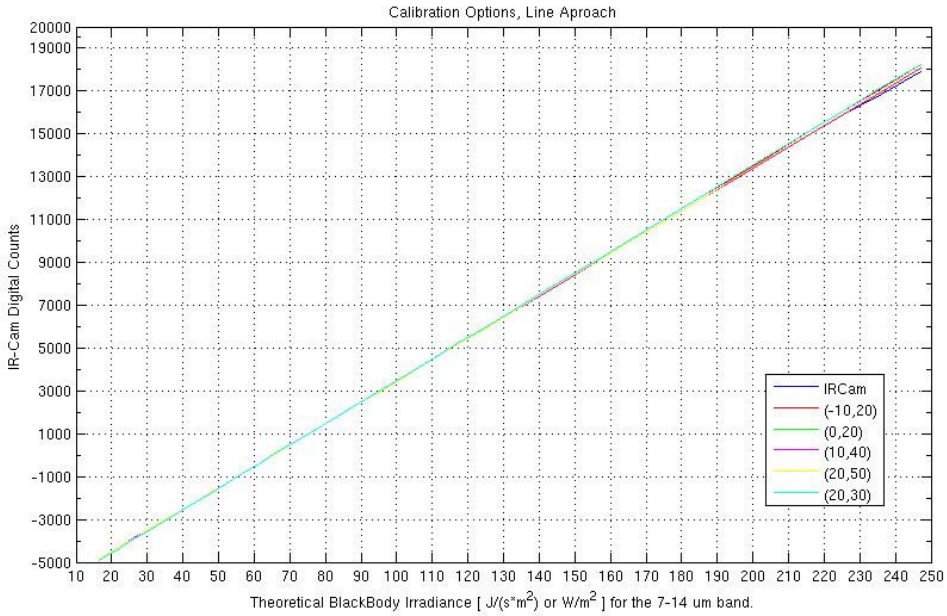

Figure 3.27: Fits of several couples of TL & TH with the experimental data. Values into brackets are (TL, TH).

In order to get the most accurate values for the calibration, I have processed the data taken in the previous complete calibration test in this way:

1. Group couples of TH (temperature high) and TL (temperature low) images as calibration points, changing the width of the interval $\Delta T =$

$(TH - TL)^\circ$ C. With our setup described in the previous tests, we got ΔT =10, 15, 20, 25, 30, 35 and 40° C.

2. Calculate the difference between the experimental point from a target @ -40° C (our minimum available temperature) and the linear fit using a straight line with the 2 selected calibration points (in irradiance, overall the incoming radiation in the 7 μm to 14 μm band).

3. Plot the difference between the experimental value and the calibration straight line (error in ° C or K). Some results examples taking TL, and TH with a ΔT of 20° C is show in Figure 3.28, 30° C in Figure 3.29, and 40° C in Figure 3.30

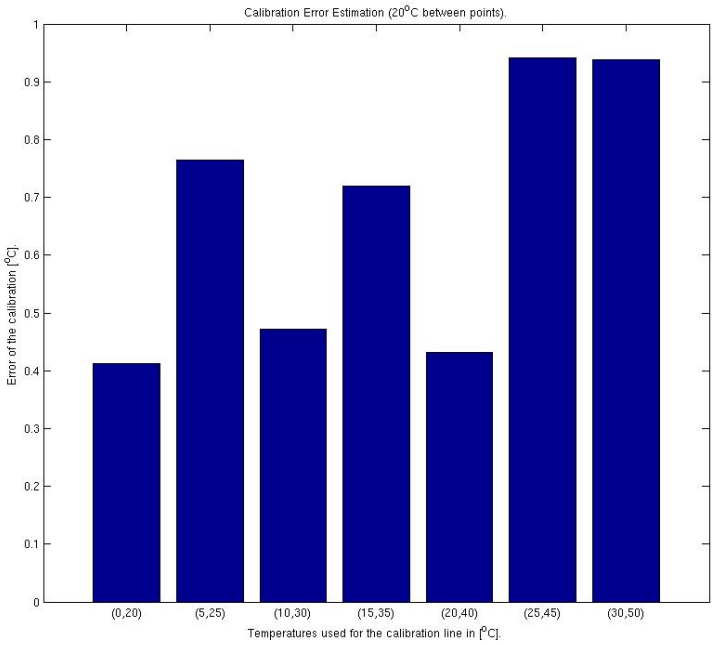

Figure 3.28: Error of line going from TL & TH with the experimental data at -40° C. Values into brackets are (TL, TH).

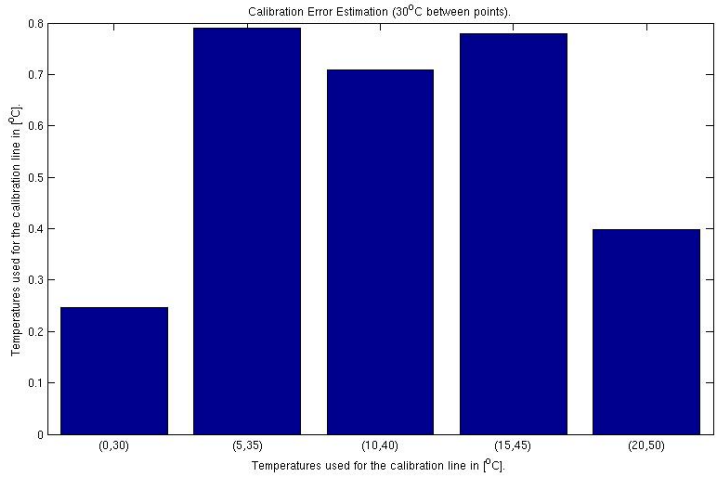

Figure 3.29: Error of line going from TL & TH with the experimental data at -40° C. Values into brackets are (TL, TH).

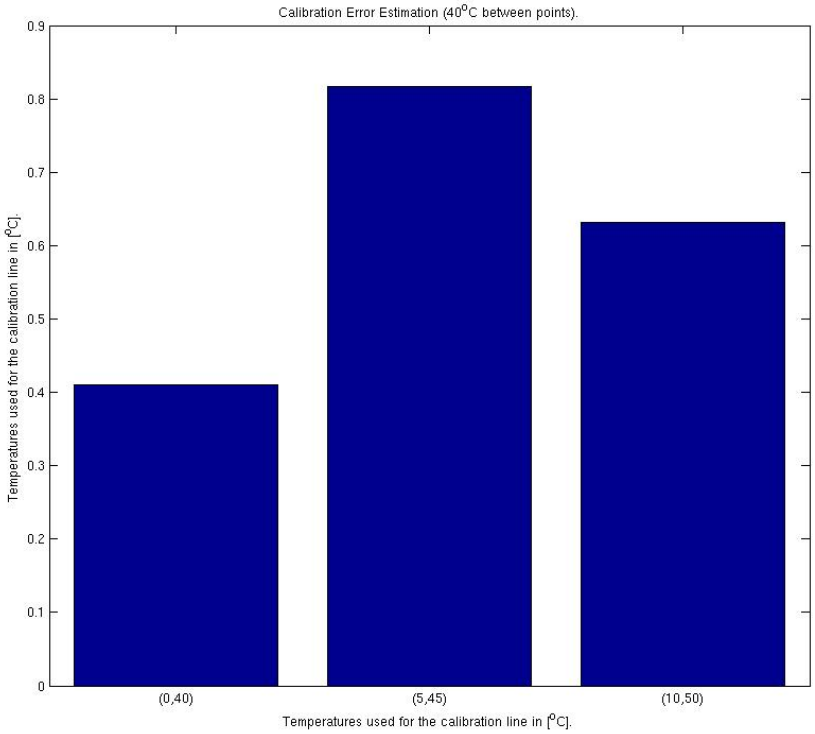

Figure 3.30: Error of line going from TL & TH with the experimental data at -40° C. Values into brackets are (TL, TH).

From the analyzed cases, the following conclusions can be extracted:

- If the interval range (the TL calibration temperature) is near to the

temperature of the target, the error drops ($\approx$ 200 mK to 400 mK)

- The relative errors seem to be independent from the calibration range. Therefore, an averaged value about $\approx$ 500 mK to 600 mK is rather common in all the intervals analyzed.

- It is important to remark here that in our setup, the environment of the micro-bolometer (shutter + optics case) are thermalized in the $\pm$10 mK range, the same for the simulated target ($\pm$10 mK) and the microbolometer's temperature. If this stability is not available in the final system, and only a rough estimation of the BB temperatures are measured, it would be necessary to carry out an additional calibration (calibration of the micro-bolometer + calibration of the BB's as a function of their own temperature).

- Regarding the NETD budget, this calibration error must be considered. I suggest at this moment that, with this run of tests and this specific setup, an average value of $\approx$ 500 mK must be included due to the calibration error using 2 on-board BB's. New tests should be done when the two filters over the array are installed because this test considers the irradiance band from 7 μm to 14 μm, and with the new bands, the detector response curve could change.

3.5 Final results

From the first tests carried out with the ULIS micro-bolometer handled with an INO modular electronics for evaluation, some important conclusions can be extracted:

- The ULIS bolometer unit tested behaves in general as expected. It seems to be a good choice for the EUSO space IR-Camera.

- The ULIS bolometer response to the incident radiation is similar to those reported by the manufacturer. It is a smooth curve, only approximate linear in a small region close to the ambient temperature ($\approx 10^\circ$ C to $\approx 30^\circ$ C). For calibration, a LUT shall be necessary, keeping fixed all the detector setpoint related parameters.

- The ULIS micro-bolometer behaves well, adjusting the tunable voltages, both in gain and offset. As the dynamic range requested is, in principle, small for the mission, we can tune the micro-bolometer to get the minimum NETD possible.

- The PRNU correction for the gain matrix should be done with the final optics, well-focused, and a big enough BB to cover the entire FoV.

- As expected, the micro-bolometer is very offset dependent. Any small change in the temperature of reference changes the resulting value of the images. It is recommended to apply the same temperature control to the FPA and the shutter (including optics). This value should be stable within 10 mK to guarantee the best performance.

- Operating temperature of the FPA is not a problem. In the range of Peltier-controlled temperatures available (from 8° C up to 30° C), the ULIS microbolometer's response does not change its performance, only the offset reference, as mentioned.

- Environment temperature of the entire camera (including the INO testing electronics) is not a problem. The environment range [0° C to 30°

C] does not change the camera performances (excluding the offset, due to variations of the temperature transmitted to shutter and optics, which should be thermalized).

- The micro-bolometer can measure temperature in the whole range tested [$-40°$ C to $140°$ C], with an approximately linear area around the ambient temperature [$10°$ C to $40°$ C]. Furthermore, an almost linear response using the energy (irradiance over the array coming from the source) vs. the detector output.

- There is no chance of adjusting the detector setpoint for the different wavelengths. The design concept involves using half detector for one band and the other half for the other band.

- Values obtained for NETD are good enough, below the 120 mK offered by ULIS and close to the expected 45 mK to 50 mK calculated for the INO camera and the optics in this configuration by INO. Best fits are obtained with a 50 sample average (as in the ULIS procedures test reports), but only 4 samples, on average, produces the expected result although with more pixel value dispersion.

- First image of each series has unusual values. It seems to have some remanence or capacitive effect in the micro-bolometer (more plausible than in the electronics). This image must be acquired and wasted, resetting the readout circuit of the micro-bolometer. Acquisition speed is fast enough (30 fps or 60 fps) to allow this.

- A calibration using only 2 reference temperatures is possible with an error lower than $1°$ C. However, it would require good stability of the detector temperature and a reliable target temperature. A suggestion

is to use the lowest temperature possible for the TL BB to improve the calibration error.

- The INO control electronics keeps two old images in memory for each series. This issue but must be taken into account when testing with this camera model.

Chapter 4

IR Camera End to End Simulation

4.1 Motivation and Global view

An End to End (E2E) dedicated simulation of the infrared camera gives us simulated infrared images of those we expect to obtain once the infrared camera is onboard a space mission. It provides us with the capabilities to study the impact of several scenarios of the atmosphere, in terms of retrieval temperature accuracy, to analyze the detection capabilities, calibration procedures, and a correction factor to be taken into account for the final data of the infrared camera onboard a space mission. At this design stage of the IR-Camera prototype, this E2E simulation will give answers to key points of the design, like the compression algorithms evaluation and an estimation of the expected accuracy of calibration options [24].

The E2E simulation is a complex software, written in C++, and divided into several stages. Figure 4.1 shows the block diagram of the E2E simulation developed for the IR Camera. It start with an IR atmospheric scenario.

After reading the input scene, the optics elements simulation takes place. Similar to the optics, the filter spectrum function is taken into account by

generating a 2-bands image. The temperature of the casing, lenses, shutter have been taken into account as well.

Following, it is necessary to create a detector model to obtain images similar to that obtained by the detector. We have to obtain images of 12 bits similar to the detector FEE and then convert them to 10 bits as the proposed prototype does. As the last step, for the instrument simulation, we have to compress images for their transmission; the goal is to achieve the highest compression ratio with a low loss of resolution.

An On-Ground simulation is also developed simulating the reception of the IR image on the ground, decompressing. After decompression, we have to obtain brightness temperature images using the calibration curves and correcting the optics distortion and background noise.

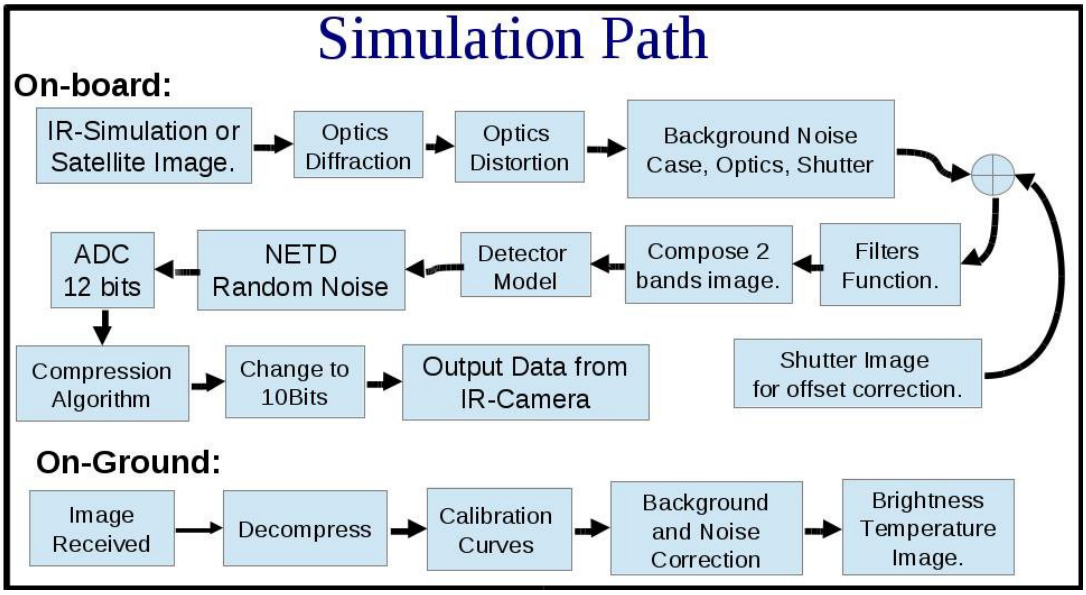

Figure 4.1: View of the END to END Simulation for the IR-Camera.

4.2 The Satellite Data Simulation Unit Software

The input of the simulation starts with the simulation of the IR scenario using atmospheric simulation software. For this development, the Satellite Data Simulator Unit (SDSU) [25] was selected as a package to compute synthetic satellite data from user-provided geophysical parameters such as cloud-resolving model (CRM) output. The SDSU is designed to simulate microwave brightness temperature, radar reflectivity, radar path-integrated attenuation (PIA), visible and near-infrared radiances, and thermal infrared brightness temperature. Instead of the simulator, we can use real satellite IR images as input for the E2E simulator code, taken by missions like MODIS [26] or CALIPSO [27]. Figure 4.2 shows a sample of the SDSU simulation for a cloud scenario for two wavelengths at 10.2 μm and 11.5 μm.

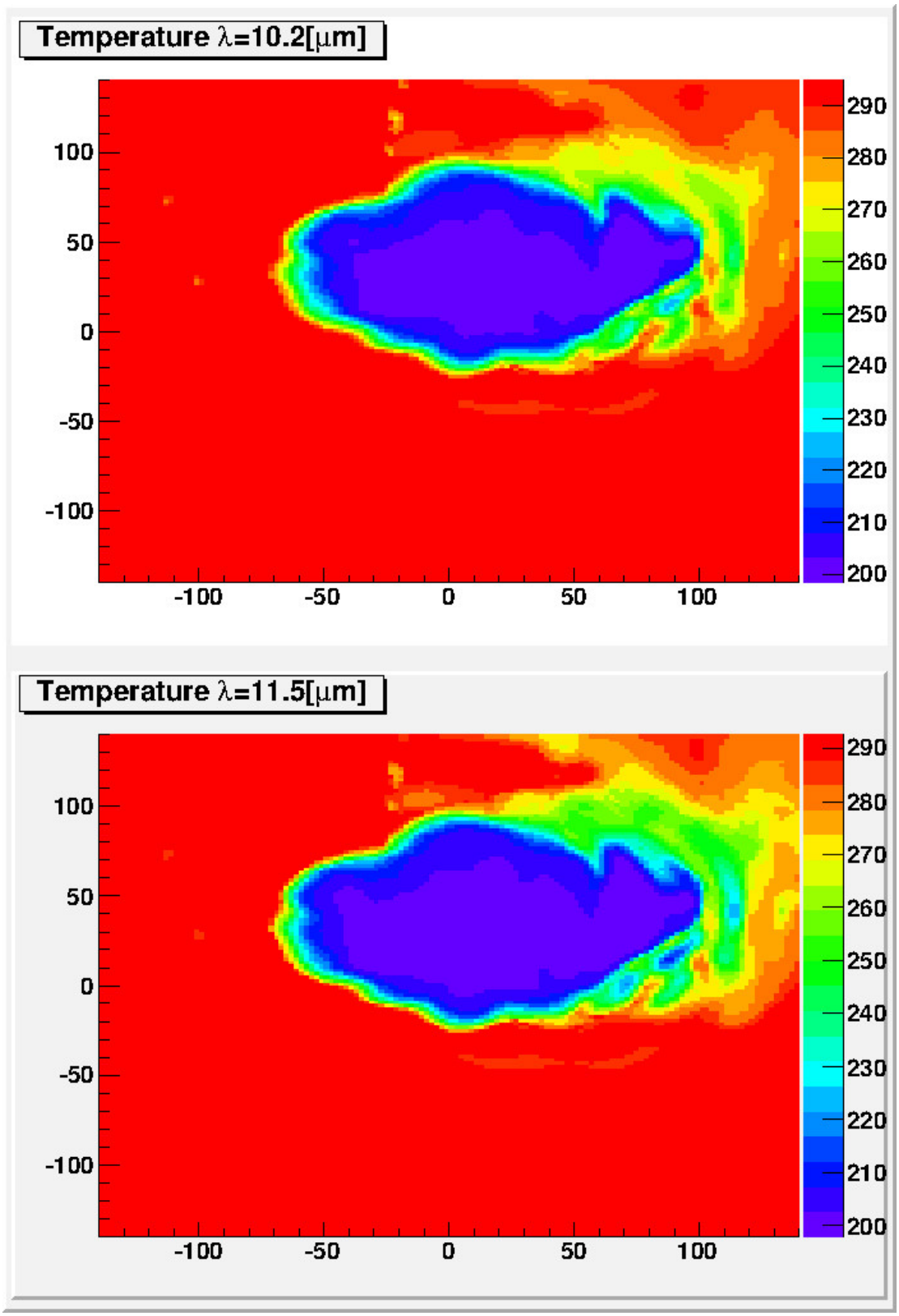

Figure 4.2: View of the SDSU simulation for a reconstructed cloud scenery in the IR Camera bands.

An IR simulated brightness temperature image is obtained from this

code. This IR is used as input to the E2E simulator.

4.3 The IR-Camera Instrument Simulator

The simulation of the infrared camera has different stages. After reading the SDSU module's scene, the optics' behavior, diffraction, and distortions caused by the optics and their efficiency are simulated. This task is carried out through the evaluated optics design of the Code-V [28] provided parameters. The image is first blurred with the PSF (Point Spread Function) calculated for several optics regions. Each pixel of the FoV image is transported to the position inside a distorted image, using a transport matrix calculated with the distortion optics design simulation data (Fig. 4.3).

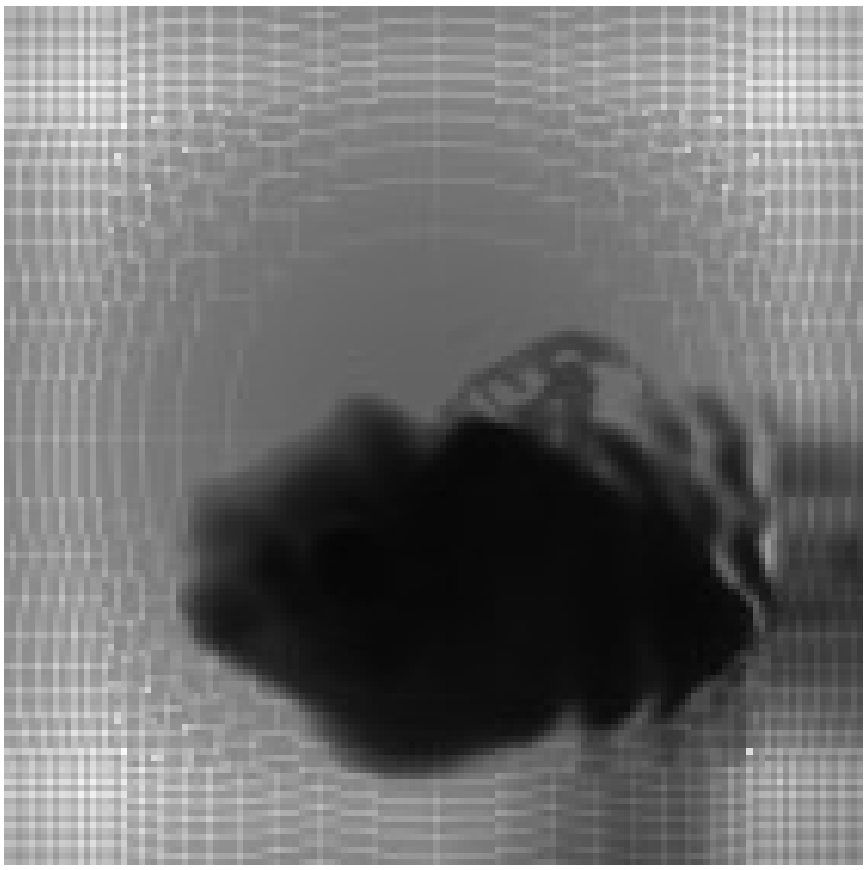

Figure 4.3: Image of an cloud seen from the camera with the barrel distortion applied.

The background noise generated by the case, optics, and the shutter has been simulated with the data provided by INO [21] and validated during the prototype characterization. The prototype camera optics module background noise implemented in the simulation is a commercial unit, the Surnia lenses from Janos [29], capable of measuring in the 7 μm to 14 μm region. This optics' main characteristics are: focal length = 25 mm and f#= 0.86, with a circular FOV of 45°. Wavelength is limited in the 7 μm to 14 μm range. The simulation includes the measured noise characteristics of this setup until the definitive optics can be characterized.

Similar to the optics, the filters spectrum function made by the manufacturer is taken into account, and produces a 2-bands image which is later processed by the detector module (Fig. 4.4).

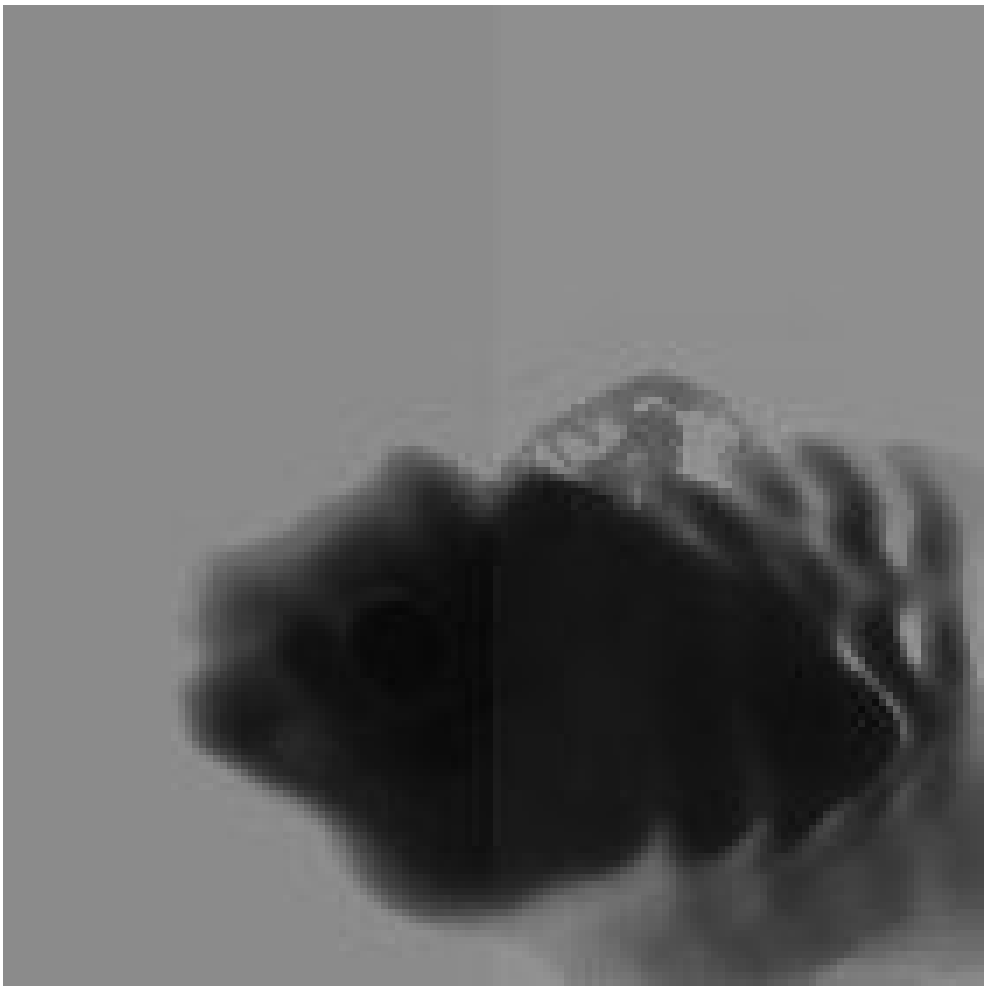

Figure 4.4: Image of an cloud seen from the camera with the filters division applied.

To create a detector model, the simulation module is based on the characterization performed with an electronics prototype module developed by INO (Canada) [21]. This electronics core is known as IRXCAM-640. Although the chip architecture exploits a TEC less operation, the already integrated TEC and the control loop allow us 10 mK stability in temperature, keeping low NETD values.

After applying the detector modules, the electronic noise (NETD) is simulated using random function generators and scaled within the observed values during the prototype characterization. An analog representation image is obtained with complete resolution. It is then passed through the

12-bit ADC (Analog Digital Converter) simulation module to adjust the image to the ADC's limited resolution. This provides us with a 12 bits resolution image of the scene. Lastly, as part of this instrument simulation, the compression algorithm and the conversion to 10 bits of the image are applied, obtaining as output from the IR camera simulator similar to the compressed image sent by telecommunication to the ground by the space camera final instrument.

The compressed image is then transmitted together with additional data from the camera monitoring system to the ground for its processing. This additional data, which includes parameters like the camera's optics temperature, and electronics voltage, is then used to calibrate and correct the image retrieved. The goal is that the instrument simulation output follows the data packages' formats and definitions to be transmitted.

4.4 On-ground processing; Cloud Top Height reconstruction

The infrared camera's objectives are set on the needs for the main mission events energy reconstruction required accuracy, which then is defined in the distance measured for the EAS point of maximum development X_{max}. The X_{max} needs to be measured with a maximum uncertainty of 120 g/cm^2 to be able to reconstruct the EAS energy with an accuracy of 30%. Therefore, the infrared camera's main objective is to reconstruct the top height of the clouds by observing the infrared emissions; this will help clarify the possible contribution to the error of the X_{max} measurement caused by the clouds layers. This then concludes that the simulation provides an output

in height rather than temperature to complete studies on the IR camera performance and mission importance. Complex methods of reconstruction are being developed for the infrared camera. Until ready to be implemented, the simulation has been included atmospheric temperature profiles and an adiabatic approach of the FOV atmosphere temperature. The adiabatic approach is based on a one-point calibration provided by the LIDAR to correlate observed temperatures to LIDAR measured Clouds' top height values.

The ground processing part of the simulation software input is the instrument simulation files. These data packages should follow the same format and contain all the data the main instrument will produce. As the image received is compressed, and in untreated values, the first step is to decompress the image and apply the correction and calibration functions. The output from this step to be performed as the initial data processing on-ground is brilliance temperature images, ready to be processed by the reconstructions algorithms.

4.4.1 LIDAR calibrated adiabatic atmosphere approach for height reconstruction.

An adiabatic process is one where no heat is exchanged between an air parcel and the surrounding air. In a steady-state atmosphere, we expect that as the air moves upwards, expands due to the reduced pressure; the adiabatic gas law is applied to characterize the atmosphere's cooling with increasing altitude. The most useful manifestation of the adiabatic law is 4.1: Adiabatic gas law.

$$p * t^{-\alpha/(\alpha-1)} = Ctte \tag{4.1}$$

And knowing the Hydrostatic equation to define the pressure 4.2, its integral 4.3, and the ideal gas law 4.4. It shows that a relation between temperature and height its possible, only missing to calculate the adiabatic constant from 4.1. To implement this method, a reference point of know height and temperature is needed; the onboard LIDAR could provide this point in JEM-EUSO.

$$\partial\rho/\partial z = -\rho/g \tag{4.2}$$

$$p = p_0 * e^{-M*g*z/(R*t)} \tag{4.3}$$

$$p = \rho * R/M * t \tag{4.4}$$

In this way, a simulation has been performed Nagoya University atmospheric simulator SDSU software to calculate the atmospheric profile (4.5) of a single layer test clouds at 3 km and 5 km. First simulate the LIDAR signal that bounces in the cloud (4.6) and calculate the adiabatic constant, using the LIDAR detected height and temperature of the camera pixel in the same location. Then using the adiabatic equation and its calculated constant, translated the brilliance temperature obtained by the camera into height, arriving at the following results 4.7.

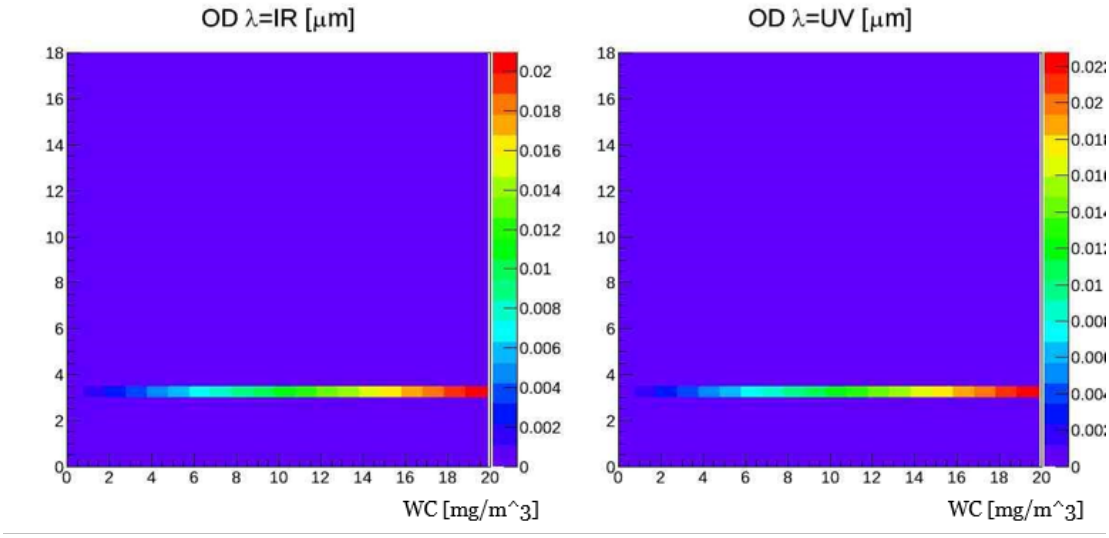

Figure 4.5: Example of the simulated optical depth for a cloud at 3 km (500 m wide) in infrared and ultraviolet. In terms of water content in color scale.

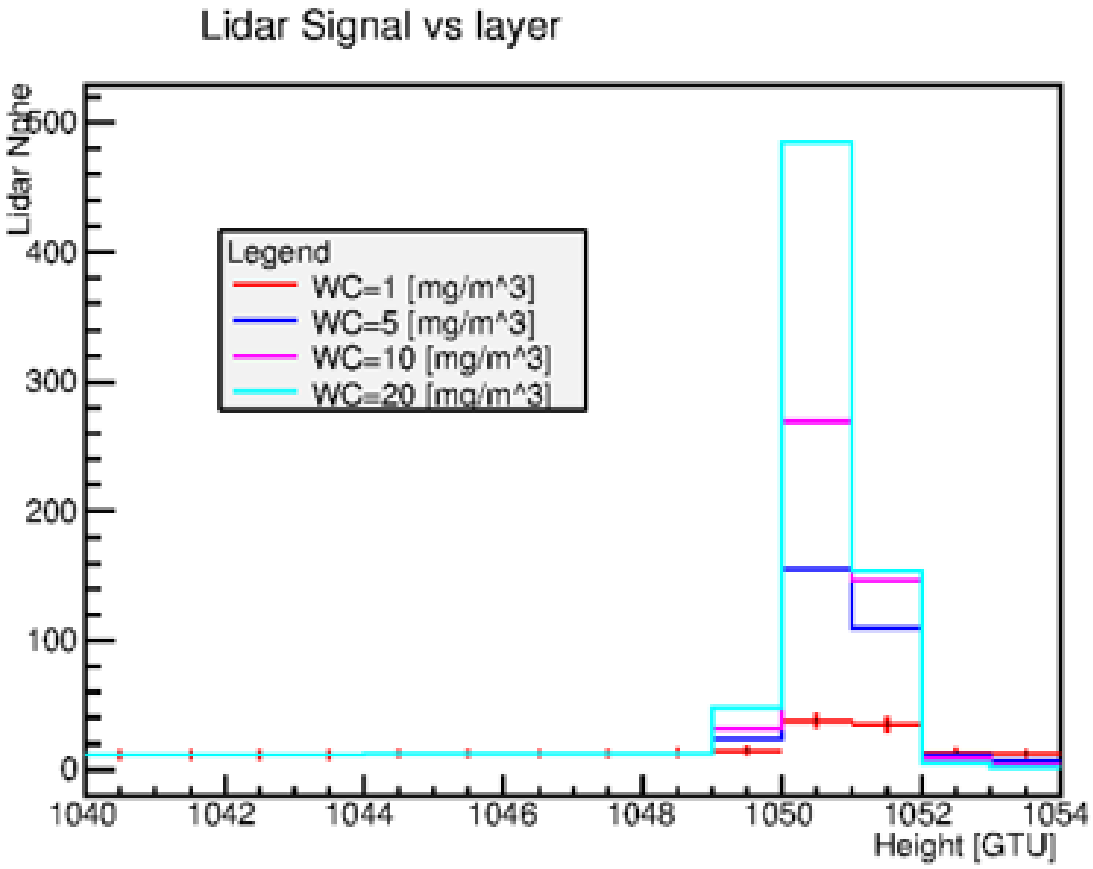

Figure 4.6: Example of the LIDAR signal that bounces in the cloud. Height is in *GTU*, where 1 *GTU* = 375 m; in this example, the cloud is at 6 km, and the LIDAR detects it at the *GTU* = 1051, *GTU* = 0 is at 400 km. Assuming, the LIDAR has an error of ±1 *GTU* or 375 m.

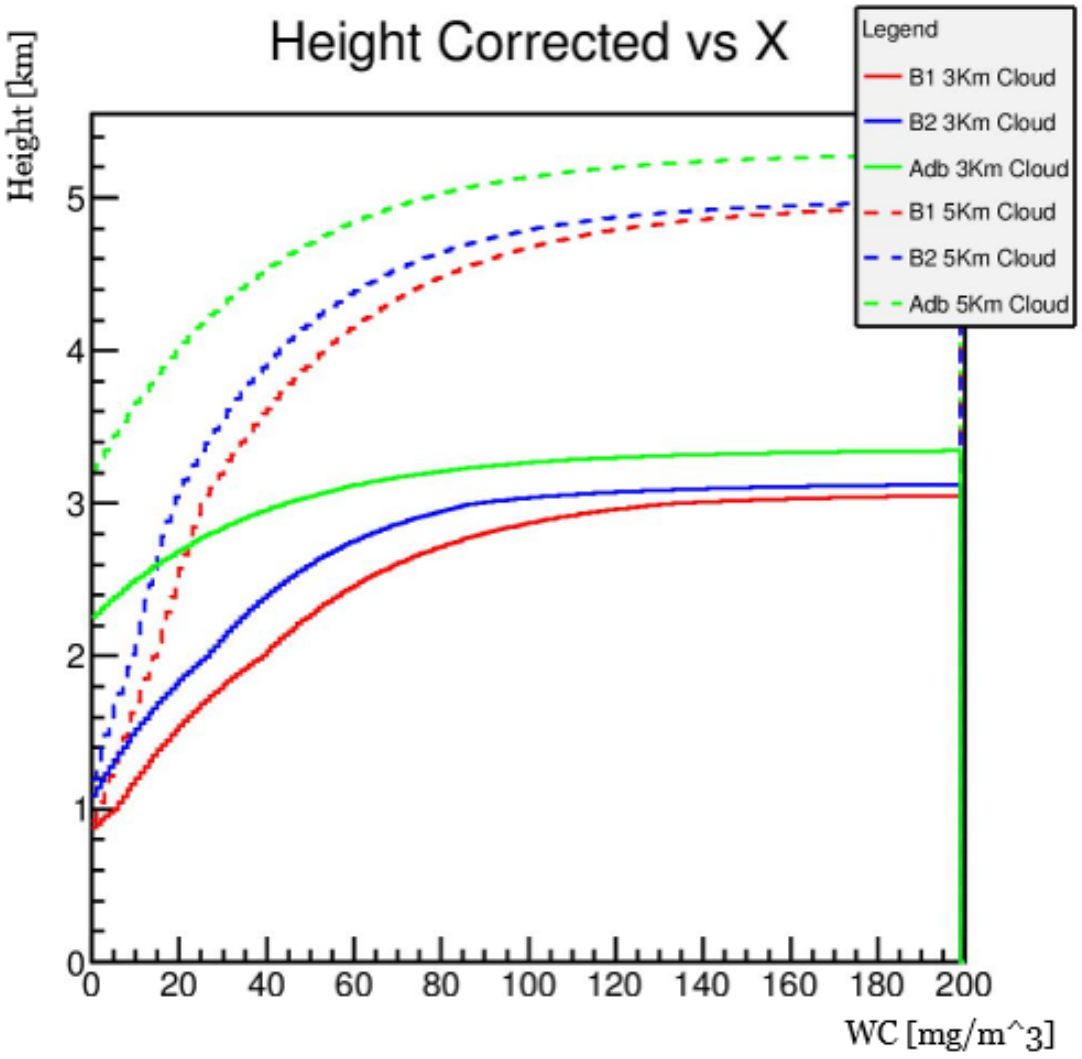

Figure 4.7: Example of the adiabatic height reconstruction, with clouds at 3 km (continuous lines) and 5 km (dot lines) in green. In blue and red, reconstruction of the height using temperature profiles for the 2-bands of the IR-Camera.

Reconstruction of real scenery from SDSU.

Comparison of a simulated scenery reconstruction using the LIDAR calibrated Adiabatic approach 4.8 and temperature profiles 4.9.

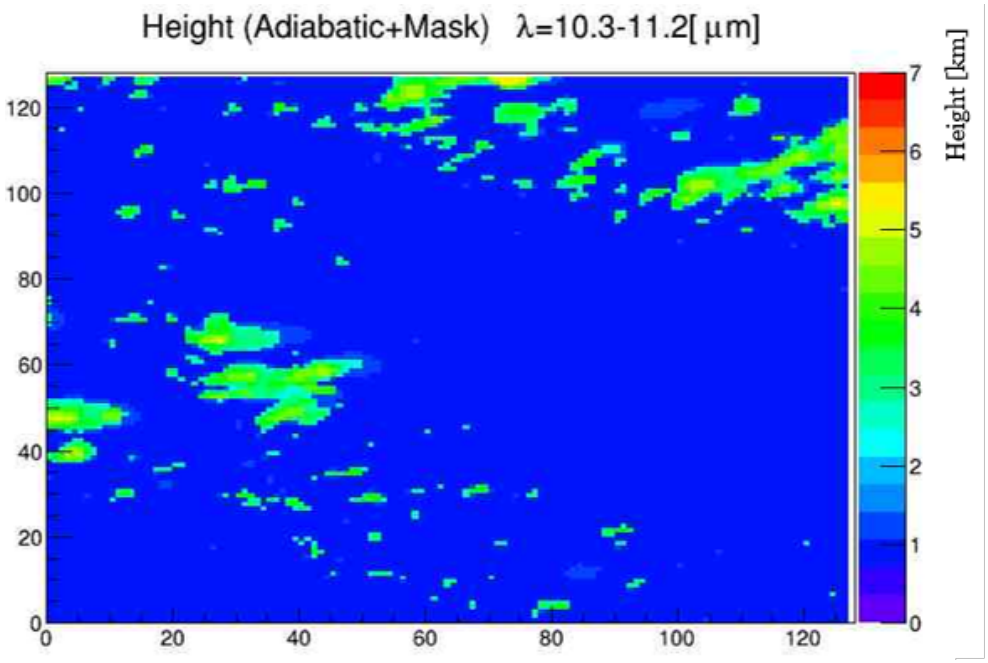

Figure 4.8: Height reconstruction of a simulated SDSU scenery and run thru the complete camera simulation, clouds height retrieved by the LIDAR calibrated adiabatic method.

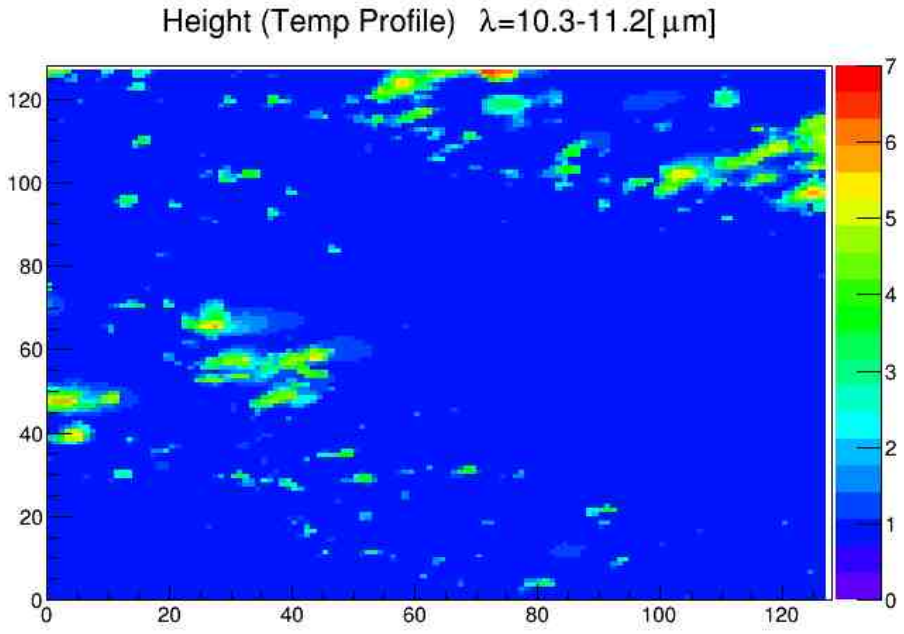

Figure 4.9: Height reconstruction of a simulated SDSU scenery and run thru the complete camera simulation, clouds height retrieved by using atmospheric temperature profiles.

4.5 Thin cloud detection in the FoV

The detection of clouds is the first challenge of the IR-Camera, in special thin clouds that could blur the signal of the cosmic ray and end in underestimating the characteristics of the cosmic ray event. The low water clouds increase very fast in terms of Optical Depth, and with just a few mm^3 of water, it can be already be treated as a black body but is not the same for the ice clouds like cirrus, that is the main reason we made this study with this type of cloud.

Calculated the Optical depth for thin cirrus using parametrization as described in [31], and have obtained (4.10) in terms of OD in the function of the cirrus Ice Water Content (IWC). To simplify the calculations, only 2 cases of ice spheres effective diameter are calculated, for $De = 135$ μm and $De = 175$ μm.

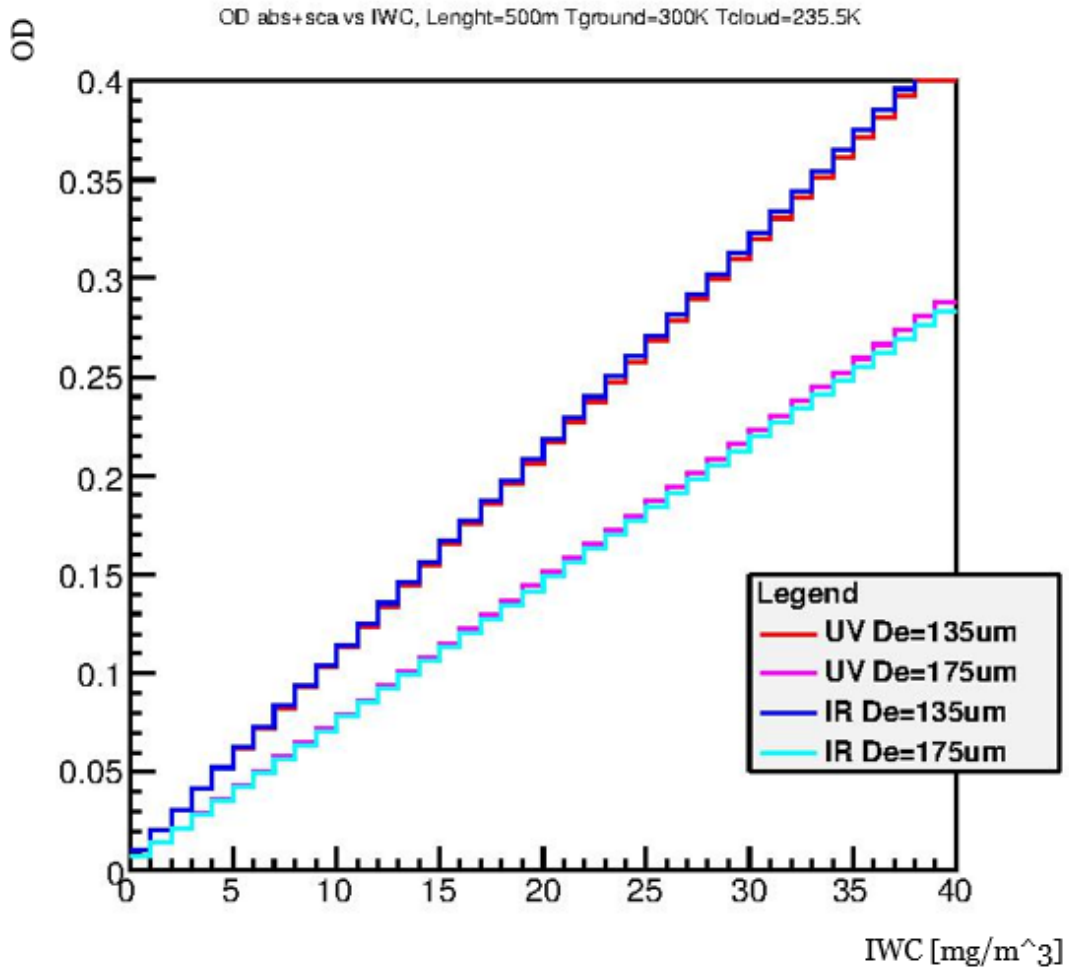

Figure 4.10: Optical depth of thin cirrus for a given medium distribution of ice particles $De = 135$ μm and $De = 175$ μm, in infrared (IR) and ultraviolet (UV), as IWC function.

Then with the calculated optical depth, we have simulated the sea IR emission. With 4.5 as a transfer function, we have simulated the irradiance and, using Planck function, the brilliance temperature that will be hypothetically captured by the IR-Camera. If we compare the temperature of a clear sky area and an area where the cirrus cloud is attenuating the radiation of the surface, it should be possible to detect cirrus with IWC contents greater than $IWC > 15$. IWC values of 15 and lower only represent $OD < 0.15$, these low OD values should not significantly impact the telescope main event reconstruction accuracy. (4.11).

$$\beta = \beta_{ground} * (1 - \tau) + \beta_{cloud} * (\tau) \tag{4.5}$$

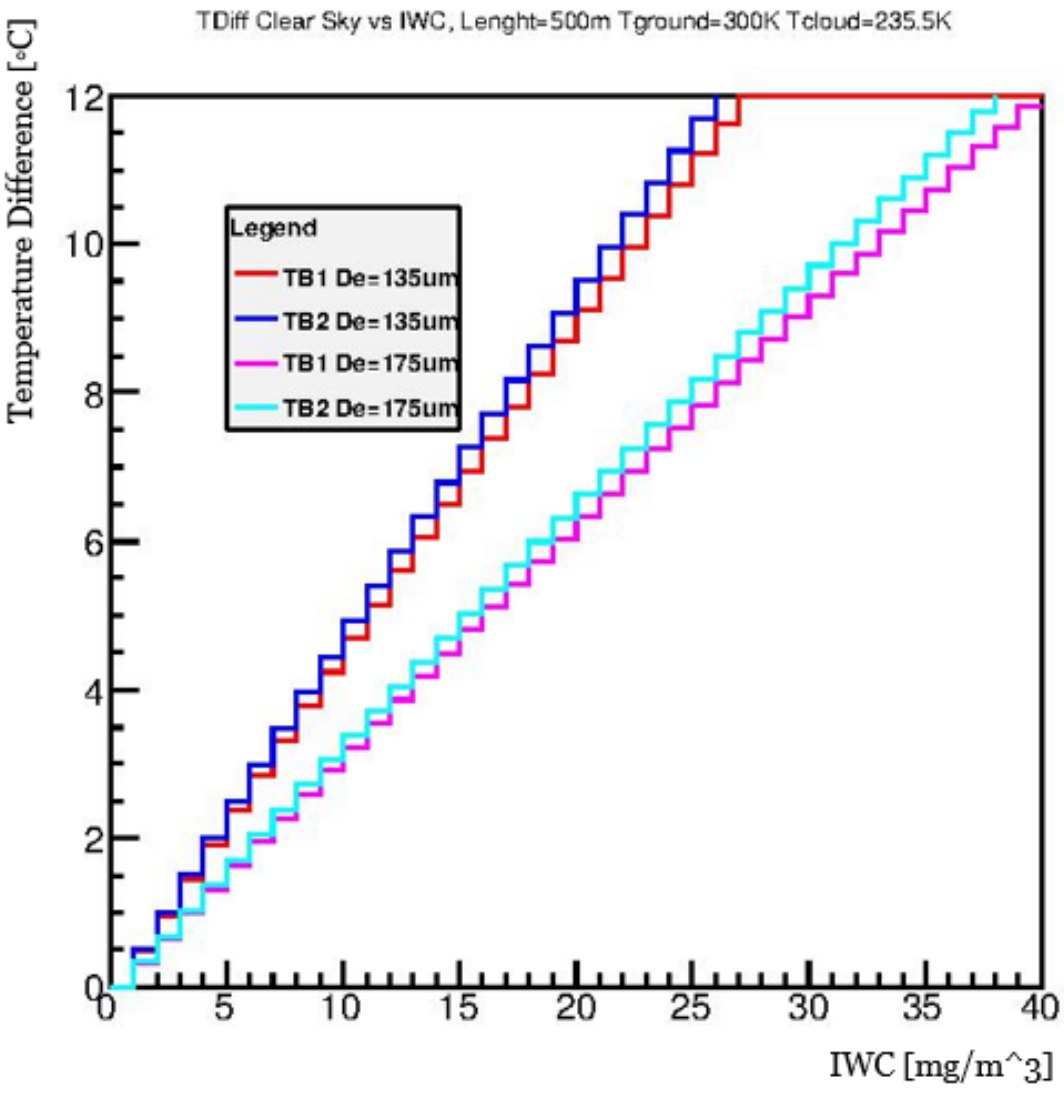

Figure 4.11: Temperature Difference of an area in clear sky conditions, minus the temperature of an area in cloudy conditions, as IWC function.

4.6 Application case: Compression algorithm study

One of the key points to estimate the data rate bandwidth for the infrared camera requirements is compressing the images to be sent. The evaluation of these algorithms' impact is crucial to assure that the images' compression

Table 4.1: Analysis of one compression image.

Comp Factor	0	3	5
In [kbits]	235.2	235.2	235.2
Out [kbits]	65.232	34.788	29.288
Comp Ratio	3.6	6.76	7.92
Typ Dispersion [K]	≈0.10	≈0.15	≈0.2
Max Dispersion [K]	0.15	0.63	0.9

will not compromise the scientific measurements.

We have used the simulator being developed for the instrument to perform this trade-off and some test images created with SDSU. The compression algorithm under study is the HP Labs LOCO-I/JPEG-LS [30]. The procedure is straightforward; we have used the simulated images of SDSU to create a control output image, then test these images with different compression factors to evaluate the compression ratio. Finally, assessing the impact on the data decompressed compared to the control images to understand how the measurements' values are affected.

For this first study, we have evaluated compression factors of 0 (near-lossless), 3, and 5. Human eyes cannot appreciate differences in the images; therefore, we have compared the values of each pixel of the test image with the related pixel of the control image and plot a histogram to evaluate the values' differences (Figure 4.12). Results are presented in Table 4.1.

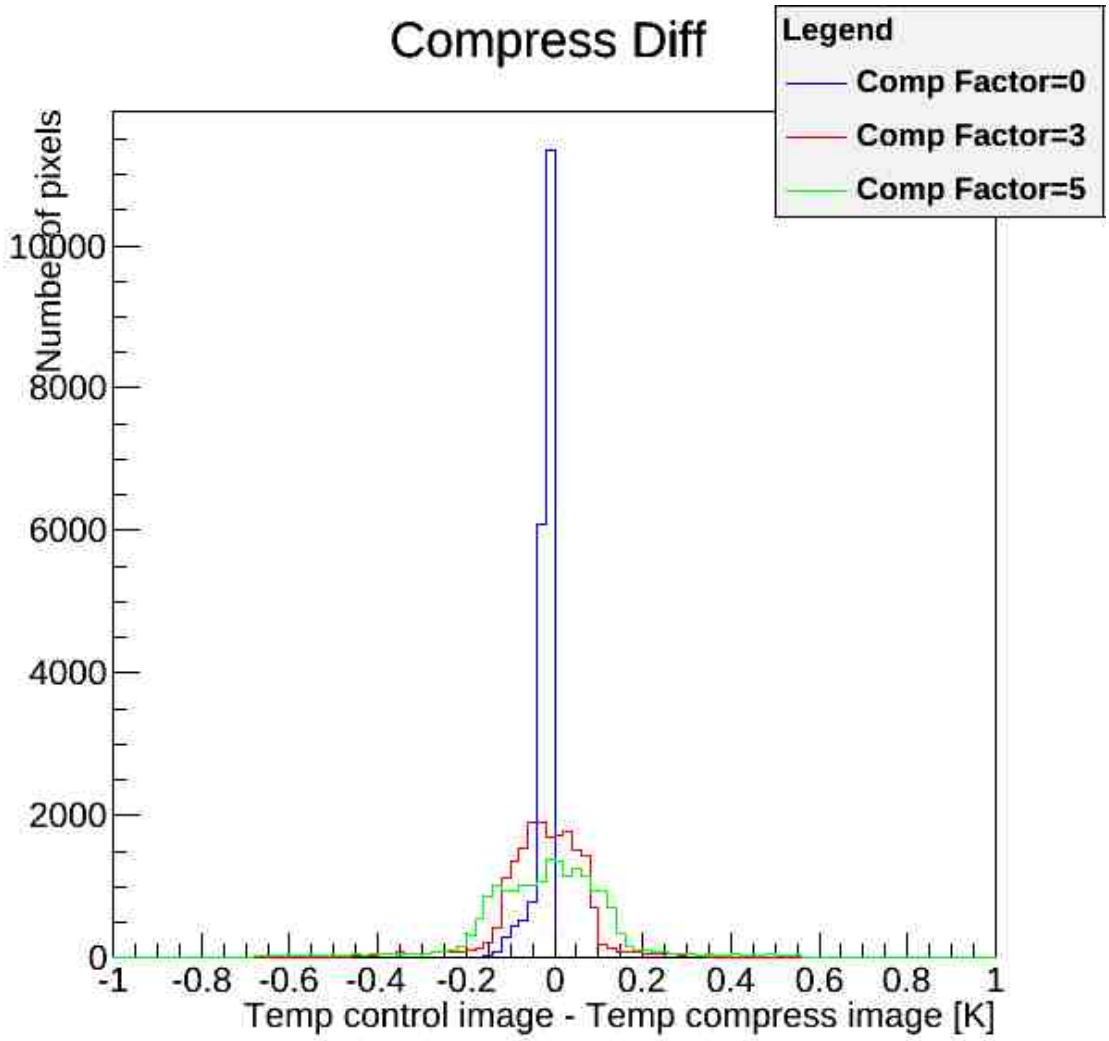

Figure 4.12: Control Image, and compressed image pixel value comparison.

Chapter 5

The JEM-EUSO Computing Model

This chapter describes a computing model for processing the offline data to be produced by JEM-EUSO every year.

5.1 Computational Requirements

5.1.1 Required Software

JEM-EUSO mission needs to evaluate the complete physical process of detecting a cosmic ray reaching the Earth. In this process includes several kinds of software involved. The injection in the Earth's atmosphere of the primary cosmic ray and the generation of the Extensive Air Shower; Simulation of the detector response; the reconstruction of the physical parameters of the primary cosmic ray from the JEM-EUSO detector data; and finally the backtracking of the particle from the Earth through Space to find the arrival direction of the primary particle.

Extensive Air Shower Simulators

Simulation of the EAS generated by the primary cosmic ray is a complex calculation made with Monte Carlo simulators developed especially for this

purpose by the astroparticle community. Extremely High Energy Cosmic Ray (EHECR) detectors do not have known sources used as calibrators of the detector response. No other possibility of detector calibration is available. This is why EAS detectors have to use the Monte Carlo simulators to check the detection system. Nevertheless, Monte Carlo simulators use particle interaction data obtained in accelerators but several orders of magnitude lower in energy. The cross-section has to be extrapolated five or six orders of magnitude over the experimental data, or make use of theoretical calculations. This results in a dependence on the hadronic model used of the results.

CORSIKA (COsmic Ray SImulator for KAskade experiment) [32] is the most powerful EAS simulator. It was initially developed for the Kaskade experiment in Karsruhe Germany. CORSIKA is a program for detailed simulation of extensive air showers initiated by high energy cosmic ray particles. Protons, light nuclei up to iron, photons, and many other particles may be treated as primaries. The particles are tracked through the atmosphere until they undergo reactions with the air nuclei or, in the case of unstable secondaries, decay. The hadronic interactions at high energies may be described by several reaction models alternatively: The VENUS, QGSJET, and DPMJET models are based on the Gribov-Regge theory, while SIBYLL is a mini-jet model. The neXus model extends far above a simple combination of QGSJET and VENUS routines. The most recent EPOS model is based on the neXus framework but with important improvements concerning hard interactions and nuclear and high-density effect. HDPM is inspired by the Dual Parton Model's findings and tries to reproduce relevant kinematical distributions being measured at colliders. Hadronic interactions at lower

energies are described either by the GHEISHA interaction routines, by a link to FLUKA, or by the microscopic UrQMD model. In particle decays all decay branches down to the 1 % level are taken into account. For electromagnetic interactions, a taylor made version of the shower program EGS4, or the analytical NKG formulas may be used. Options for the generation of Cherenkov radiation and neutrinos exist. CORSIKA may be used up to and beyond the highest energies of 100 EeV.

AIRES (AIR shower Extended Simulations)[33] was developed by Sergio Sciutto. AIRES identifies a set of programs and subroutines to simulate particle showers produced after the incidence of high energy cosmic rays on the earth's atmosphere and to manage all the data associated with these simulations. The present AIRES release includes a link to the recently developed QGSJET-II hadronic package (version II-03, developed by S. Ostapchenko). The executable AiresQII is the one to be used to invoke this model. This program needs about 200 MB of RAM memory to run.

CONEX [34] is a hybrid simulation code that is suited for fast one-dimensional simulations of shower profiles, including fluctuations. It combines Monte Carlo simulation of high energy interactions with a fast numerical solution of cascade equations for the resulting distributions of secondary particles. For a given primary mass, energy, and zenith angle, the energy deposit profile, as well as charged particle and muon longitudinal profiles, are calculated. Furthermore, an extended Gaisser-Hillas (GH) is performed for each shower profile, similar to what is implemented in CORSIKA. The shower simulation parameters, profiles, and fit results are written in a ROOT file.

EAS simulators are designed to simulate EAS generated by usual pri-

maries. Some primaries as ν or τ have to be simulated with other codes such as PHYTIA, TAUOLA, and HERWIG. These codes simulate the ν or τ first interaction, and the particles are later injected into the EAS simulator to obtain the complete EAS.

JEM-EUSO Detector Simulator

JEM-EUSO telescope simulation is done by either of the codes written by the collaboration; official codes are ESAF (EUSO Simulation and Analysis Framework) and the Saitama Code. [35]

Event Reconstruction and Data Analysis

As in the simulation, the JEM-EUSO telescope event's reconstruction is done by either of the codes written by the collaboration; official codes are ESAF (EUSO Simulation and Analysis Framework) and the Saitama Code.

Data Analisis is done by macros in ROOT, is a framework for data processing, born at CERN, at the heart of the research on high-energy physics.

5.1.2 Use-cases Scenario

RAW data handling

The RAW data for events surviving the JEM-EUSO trigger system will be processed, when possible, on the main sites designed by the Simulation Committee. Then, the original data and the processed data will be copied to the main data repository.

Main telescope raw data The Main telescope telemetry is limited at 250 Kbps, making the amount of raw data produced per year less than 500

GB. As this data is precious, at least 2 copies are saved on every dataset to avoid losses + overheads; we estimate 1095 GB/Year to be stored. Then datasets are replicated among the sites collaborating to research.

Accessory instruments and Housekeeping data The Infrared Camera (IR) and Housekeeping system (HK) telemetry is limited at 25 Kbps for each subsystem, making raw data produced per year to less than 100 GB for both systems combined. As this data is precious, at least 2 copies are saved on every dataset to avoid losses. Then datasets are replicated among the sites collaborating to research.

Simulation data handling

The Simulation Committee will evaluate the simulation production strategy, and then the needed simulations will be processed on the main sites designed for this task, after production, the data will be copy to the main data repository.

Physics analysis

Physicists will typically use desktop systems for preparing and finalizing data analysis. Most analysis will require significant access to the main data repository. Many analyses will be based on a simple results review. However, other analyses will sometimes require access to high CPU needs, particularly when the data needs to be reprocessed for test and other new analysis tasks. In such cases, physicists' ability to run jobs directly on the grid will also be needed, requiring additional processing and storage capability. Results from the different analysis will typically be stored at storage elements dedicated to local physics analysis sites. Some limited

data sets will be stored on local systems at universities and laboratories. The results will be visualized using standard tools on desktop systems. This is a common practice noted in other collaborations computing model.[36] [37] [38].

5.1.3 Computing Requirements

Monte-Carlo simulation.

Based on past experiments' experience, the data analysis will consume a large fraction of the total amount of resources. The production scheme of Monte-Carlo simulation is based on the software that the Collaboration Board selects. Monte-Carlo data will be generated in an amount of 100 or 1000 times faster to collected real data (more than 1,000 events with energies between $7x10^{19}$ eV $\leq E \leq 10^{21}$ eV are expected during EUSO operation). This means that JEM-EUSO will need more than 100.000 simulated showers for the use of the whole collaboration physicist researchers. To avoid requesting a prohibitive amount of resources and enrich generated events with the collaboration signal of interest, the simulation board must review the objectives for simulation production goals dynamically.

Officially simulation software that EUSO will use are Corsika, Conex, Aires, and Slast showers generator. Eventually, some physicists of the the collaboration will use custom made software or customized versions of the official software.

RAW data and Analysis.

In contrast with Monte-Carlo for reconstruction and the simulation tasks, not all can be easily scheduled, as this will potentially involve all the physi-

cists of the collaboration applying customized algorithms many times on subsets of the data of various sizes. This way of performing analysis is called non-scheduled analysis. However, it is foreseen to perform planned analysis during the same production tasks (as the reconstruction passes) and, therefore, over the entire data set. This scheduled analysis will group in each pass all the official algorithms. The time needed to analyze reconstructed events depends very much on the complexity of the analysis algorithm and the Grid processing overhead. The latter can only be predicted once the Grid analysis has been exercised with the final middleware and at the final scale. We have considered the processing power an average value that can vary largely from one analysis to another due to different software versions and settings. To estimate the processing resources required for the analysis, we have considered three cases; i) that 200 physicists will exercise many times their algorithms on a small fraction of the data, ii) on a larger subset of the data, and iii) that the various analyses launched by the physics working groups are performed only once over the entire set of reconstructed data. Scheduled analysis regrouping many analysis tasks will require a larger computing power per event than chaotic analysis. Individuals will also perform analysis using computing resources available at their home institutes. These resources are not accounted for in the present evaluation of the requirements.

All data produced by the EUSO detector will be stored permanently for the duration of the experiment. This includes the raw data, one or more copies of the raw data, one set of Monte-Carlo data, reconstructed data from all reconstruction passes, analysis objects, calibration, and monitoring data. A fraction of the produced data will be kept on short term storage, providing

rapid access to data frequently processed and for I/O dominated tasks. The media for permanent and transient storage will be decided by the technology available. Presently the permanent storage media is magnetic tapes and transient storage disks. The ratio between disk and tape storage will change with time and dictate the price-performance ratio. The parameters used to estimate the storage requirements are derived from the Data Challenge experience.

The transient storage requirements on fast access media depend very much on the computing model, the balance of available distributed processing resources, and the network bandwidth and occupancy. In the absence of Grid simulation tools, our estimates on needed transient storage capacities are based on the requirement to store on disk data that will be frequently accessed primarily through non-scheduled tasks.

As commented, officially, analysis software that EUSO will use are ESAF and Saitama code. Eventually, some Physicists of the collaboration will use custom made software or customized versions of ESAF and SAITAMA.

Calibration.

The overall organized processing (calibration, alignment, reconstruction, and scheduled analysis) is scheduled and prioritized in the Grid resources. Because of its importance, calibration software and the calibration simulation needs should be defined and considered when allocating resources.

Ramp-up of resources after launch.

EUSO plans to have installed 60% of resources in the first year after launch, 80% in the second year, and 100% end in the third year. From there on,

after launch, EUSO plans on an annual investment of 15% of the value of the installed resources in the third year.

5.1.4 CPU, Data Storage, and Network Requirements.

Detailed resources requirements for Data analysis and Monte-Carlo simulation.

CPU requirements

All numbers in PFLOPS (petaflops = 10^15 flops). Yearly based estimation.

Task	Lower Estimation	Upper Estimation
Calibration	72	720
Data analysis	144	1440
UnScheduled tasks	144	1440
MC-Simulation	2880	28800
Total	3240	32400

Table 5.1: CPU requirements table.

Based on 1000 real events, Monte Carlo (1 event = 28,8 Tflops) should be around 100.000 to 1.000.000 events. Raw data and Analysis is estimated to be around 5% of Monte Carlo. For Unscheduled tasks, estimation is the same for Raw data and Analysis, and calibration is estimated to be half the needs for Unscheduled tasks but prioritized.

One Intel Q9400 is capable of 2 GFLOPS (Based on Whetstone Benchmark)[44], 63 PFLOPS is the equivalent of 365 Days of 1 intense CPU work. Yearly we will need around 100 or 500 CPUs of this type, estimating 70% of efficiency. (This is a relatively high-performance CPU, many computer centers may have older CPU.)

Data Storage requirements.

Permanent storage.

All numbers in GB (Giga-bytes = 10^9 Bytes). Yearly based estimation.

Task	Lower Estimation	Upper Estimation
RAW data	1095	1095
RAW data accessories	100	100
Data analysis	1000	10000
MC-Simulation (Official)	30000	300000
Other data	2000	4000
Total	34195	315195

Table 5.2: Permanent storage requirements table.

Monte Carlo (1 event = 300 MB) should be around 100.000 to 1.000.000 events. Raw data and Analysis is estimated as 10 MB/event. Other data includes calibration data and monitoring data.

Transient storage.

All numbers in GB (Giga-Bytes = 10^9 Bytes). Yearly based estimation.

Task	Lower Estimation	Upper Estimation
UnScheduled tasks	1000	10000
Test software	50	100
MC-Simulation (In Prod)	30000	300000
Total	31050	310100

Table 5.3: Transient storage requirements table.

Estimated 80% of eficiency for Data storage resources.

Network requirements.

Network bandwidth requirements depend mainly on the architecture and number of copy sets for permanent storage; more details about the EUSO Data Repository will be given in section 5.2). Also, the number of researchers working on each set of data should be considered for proper network bandwidth estimation.

Network requirements.

All numbers in GB (Giga-Bytes = 10^9 Bytes). Daily based estimation.

Task	**N**	**Unity Estimation**	**Lower Estimation**	**Upper Estimation**
Permanent storage sync	3		85	821
Review of daily raw data (research groups)	10	3-9	30	90
Physicist working on grid	10-30	1-9	10	270
Total			125	1181

Table 5.4: Network bandwith requirements table.

Each of the resource centers should provide enough data bandwidth to ensure proper data transfer.

Based on the data and CPU requirements, we found that the Tiers architecture is not recommended to EUSO.

5.2 JESR EUSO Software Repository

5.2.1 JESR Release Policy

Releases are, by definition, anything that is published beyond the group that owns it. In our case, that means any publication outside the group of people on the JESR list. If the collaboration is being instructed to download a package, then that package has been released.

Various packages are made available to the developer community for testing purposes during developing software and preparing a release. Special care should prevent non-developers from downloading and using nightly builds, snapshots, release candidates, or other similar (non-official release) packages. The only people who are supposed to know about such packages are the researchers following the developers' list (or searching its archives) and thus aware of the package's conditions. The general public should not use such test packages.

1. Test Packages are not released. All releases require due process and official approval. Test packages are for testing ongoing development and should only be discussed inside the project development list. It should be listed in the repository as test-builds.

2. Nightly Builds and personal test, usually once a day. These packages are intended for regular testing of the build process and to give automated testers a common build for regression testing. They are used by the developer who is working directly on the code. It should be listed in the repository as private and the name of the responsible developer.

3. Release Candidates are packages that have been proposed for approval

as a release but have not yet been approved by the project. These packages are intended for developers (and users who follow the development discussions) to test and report back to the project regarding their opinions on the package quality compared to prior releases. Many release candidates are possible before a release approval. Users that are not interested in development testing should wait until a release is formally approved. It should be listed in the repository as prerelease.

4. Releases are packages that have been approved for general public release, with varying degrees of caveat regarding their perceived quality or potential for change. Releases that are intended for everyday usage by non-developers are usually referred to as "stable" or "general availability (GA)" releases. Releases that are believed to be usable by testers and developers outside the project, but perhaps not yet stable in terms of features or functionality, are usually referred to as "beta" or "unstable". Releases that only represent a project milestone and are intended only for bleeding-edge developers working outside the project are called "alpha". Should be listed in the repository as official.

5.2.2 JESR Structure

The archive directory structure is as following:

official/
stable01/
x64/
i386/
stable02/

beta01/

alpha01/

prerelease/

x64/

i386/

test-builds/

x64/

i386/

private/

users/

ana.garcia/

pepe.manolo/

5.2.3 JESR Deployment

1 main server & 1 mirror (CETA/CIEMAT).

Local mirrors (at each RC (Resource Center), daily sync, simple local mirrors available as NFS volumes to local working nodes). JESR NFS should be mounted in the /usr directory as /usr/JESR/ with only-read access.

5.2.4 JESR Certification Process

JESR Certification Process compounds the steps needed to convert a prerelease to an official stable release, to be used by all the collaboration physicists and engineers involved on EUSO.

The first step is Software Testing made by the developers, which is an

investigation conducted to provide information about the software's quality under test. Software testing also provides an objective, independent view of the development phase to appreciate and understand the software's risks. Test techniques include, but are not limited to, the process of executing a program or application with the intent of finding software bugs.

Software testing can also be stated as the process of validating and verifying that a software program/application:

1. meets the operational and technical requirements that guided its design and development;

2. works as expected; and

3. can be implemented with the same characteristics.

Depending on the method employed, software testing can be implemented at any time in the development process. However, most of the test effort occurs after the requirements have been defined, and the coding process has been completed. As such, the methodology of the test is governed by the software development methodology adopted. The output of this stage is a report made by the developers and submitted to the Simulation Committee for the Verification stage.

The Verification stage, made by the Simulation Committee, can be summarized in one single question. Have we built the software right? (i.e., does it match the specification report made in the software design and report made in the Software testing stage).

The collaboration board makes the last Validation step, and again it can be resume by the following question. Have we built the right software? (i.e., is this what the people in the collaboration wants). After this step, the

prerelease is marked as official stable and copy in the software repository's appropriated directory.

The terms verification and validation are commonly used interchangeably in the industry. It is also common to see these two terms incorrectly defined. According to the IEEE Standard Glossary of Software Engineering Terminology:

- Verification is the process of evaluating a system or component to determine whether a given development phase's products satisfy the conditions imposed at the start of that phase.
- Validation is the process of evaluating a system or component during or at the end of the development process to determine whether it satisfies specified requirements.

When a new release is made, people must be informed about the availability of new releases. At the very least, emails should be sent out announcing this to all appropriate mailing lists. Many top-level projects have announcement lists for this purpose.

5.3 JEDR EUSO Data Repository

5.3.1 JEDR Architecture

As a conclusion from section 5.1 Tier architecture is not suitable for EUSO. Because of Low/Medium data/CPU needs. Even a medium resource center could have all the resources needed by EUSO. The only obstacle with managing all the resources in only one center is the bandwidth needed.

To solve this, EUSO data will be mirrored in at least three sites located in separated regions to improve data access from the physics working on the grid. (Data links between countries in the same continent are faster than inter-continental links).

When fully set up, EUSO will have 3 Full JEDR: American, Japanese, and European. Containing each one a full set of the RAW DATA, MC data, and ground analysis data. Additionally, other resources center could have a direct connection to the nearest JEDR with read access only.

5.3.2 JEDR Catalog

For the files in the Data Repository, a Catalog (Database) should be maintained to track each file and faster searching. The catalog has different tables for each type of file; MC, Raw data, and simulated/reconstructed data.

The simulation files table with the following data: Identifier, Primary Particle, Energy, Zenith angle, Azimuth angle, SW-Release, Low-energy-hadronic-model, High-energy-hadronic-model, thining, User, Site, latitude, longitude, and LFN (Logic File Identifier).

The raw data table, containing: Identifier, time, date, post-processed, ground-data analysis output identifier, and LFN.

The simulated/reconstructed data table, containing: Identifier, time, date, site, user, Mother-raw data identifier, and LFN.

The catalog is kept in one master site (any of the JEDR, to be defined) and mirrored to the others full JEDR. The catalog and the full JEDR will be synchronized daily.

Main JEDR access method

Two methods will be implemented to access files on the JEDR: simple download and other for direct work on the grid.

For simple download, via a toolkit (by a simple software or a PHP web site, TBD), each collaboration researcher will have privileges to search the entire catalog and download the files selected. This option, simple, efficient but limited to the amount of data that the user can download daily for bandwidth limitations. For the analysis that would require huge amounts of data (Eg, running a new program over 3 months of raw data), a portion of the grid is reserved for users.

For grid work, a simple program that receives the specs to search in the database as data-cards and outputs the LFN will do the work. So any physics could write a simple script that first search the database for the files wanted and then performs analysis on the files found.

Both programs will be included on the JESR toolkit to provides all functionality to query, browse, download, and direct GRID jobs.

5.3.3 JEDR namespace

Archive directory structure.

simulation/r01/eas/
det/
rec/
r02/eas/
det/
rec/

data/ rd/

re/

In simulation MC, "r01"..."rxx" refers to the software release used for simulation, "eas" is the extensive air shower simulation, "det" is the detector simulation output files, and rec is the reconstructed events from the simulation. Also, the data folder is separated into two subfolders, "rd" refers to real data (rd/) and "re" to reconstructed events (re/).

For simple access, local JEDR will be available to local working nodes as NFS and should be mounted in the /mnt directory as "/mnt/JEDR/" with only-read access.

5.4 Administrative Organization

5.4.1 Collaboration Board (CB)

It is formed by the Mission PI, the heads of divisions, and nationals PI. Is the maximum instance for decisions. It evaluates the reports from the simulation committee and have the final stage of defining the main objectives.

5.4.2 Simulation Committee (SC)

It is formed by the managers of each task force explained below. It evaluates the needs of the scientist collaboration and traces the path to solve its needs. Reports to the CB, for aspect as major changes in the programs, resources needs, and changes in the analysis goals.

Production Task Force (PTF)

This group is in charge of steering the MC, and simulation/reconstruction. They have the responsibility to maintain the JEDR updated and working properly.

Production Manager (PM)

Is the chairman of the PTF (Production Task Force).

Software Development & Certification Task Force (SDCTF)

This group is in charge of software tests and development. They have the responsibility to maintain the JESR updated and working properly.

Software Manager (SM)

Is the chairman of the SDCTF (Software Development & Certification Task Force).

Calibration Task Force (CTF)

This group is in charge of the analysis task that concerns the JEM-EUSO instrument calibration.

Calibration Manager (CM)

Is the chairman of the CTF (Calibration Task Force).

Resource Center Task Force (RCTF)

This group has the responsibility to maintain the resources among different centers working. It integrated with personal from the collaboration and one representative for each resource center participating in the collaboration.

Resource Manager (RM)

Is the chairman of the RCTF (Resource Center Task Force).

5.5 Virtual Organization

To separate development, production, and user tasks, JEM-EUSO will have 4 different VO (Virtual Organization), each with separate privileges over the resources. The aim is to organize more efficiently the work in the grid.[40]

5.5.1 JEVO for Software Certification & Development

A virtual organization only for the development and software repository maintenance is managed by the Software Development & Certification Task Force (SDCTF) members and have read/write access to the JESR.

5.5.2 JEVO for Calibration

A virtual organization only for the calibration analysis tasks, managed by the Calibration Task Force (CTF), has privileges for resources needs over the other virtual organization.

5.5.3 JEVO for Scheduled Production

A virtual organization only for the scheduled MC and ground analysis tasks, managed by the Production Task Force (PTF), and have and have read/write access to the JEDR.

5.5.4 JEVO for Unscheduled Production

A virtual organization for the physics of the JEM-EUSO collaboration that wants to use grid resources. This VO has read access to the JEDR and the JESR.

5.6 JEM-EUSO Middleware

As there are so many different middlewares, and each resource center could use a different one, JEM-EUSO needs tools to make work between different middleware. Starting from the mount types for the data and software repository and beyond basic tools for each architecture. There is a need to isolate the users from middleware specifics.

The first step is the JESR toolkit for the JEDR catalog and easy download for basic users.

Chapter 6

Conclusions

At the UHECR regime observed by EUSO, above 10^{19} eV, clouds' existence will blur the observation of UHECR. Therefore, the monitoring of the cloud coverage by the EUSO space telescope is crucial to estimate the effective exposure with high accuracy and calibrate the UHECR and EHECR events just above the threshold energy of the telescope. The infrared camera of EUSO is an infrared imaging system aimed to detect the presence of clouds in the FoV of the EUSO main telescope and obtain the cloud coverage and cloud top altitude during the observation period of the EUSO main instrument.

In this work, contribution at the level of System to the full prototyping and space-qualified design of the infrared camera for a UHECR space mission is pointed out in Chapter 2. The detected radiation is basically related to the target temperature and emissivity, and it can be used to estimate the clouds' top height.

In Chapter 3, the characterization of the infrared camera prototype has been accomplished. From the prototype tests, we can conclude that the ULIS bolometer's response to the incident radiation is similar to those data reported by the manufacturer and predicted by theory. From the first tests

carried out with the ULIS microbolometer handled with an INO modular electronics for evaluation, this detector seems to be a good choice for our space mission. Therefore, the infrared camera's design should continue using this prototype as a baseline if the requirements do not change, and the advances in electronics do not bring us a better detector in the upcoming years.

In Chapter 4, the development of the E2E simulation and the obtained results have been presented. Our further objective is to make the model more extensive and robust, covering each area of the design more deeply and to try to address the impact of several design characteristics to have a very detailed study of the detection error, and to provide a platform for the IR-Camera design engineers to test the changes necessary in each step of the further development processes. To this moment, a study on the compression algorithm's impact on accuracy was based solely on this simulation software.

Chapter 5 presents the bases of a computing model for the processing of the ground segment support data produced by the EUSO space observatory every year for the simulation of the instrument and the data analysis tasks. This work has contributed very significantly to the UAH-SPAS group, providing the groundwork necessary to implement so efficient resources necessary to analyze the data provided by EUSO. This work has been presented in two JEM-EUSO international meetings, and its under discussion in the collaboration. The Computing Model of EUSO serves as a major guideline for installing the ground segment of the mission. Estimations on the infrastructure size to be deployed are made. The software requirements to be installed where listed and an administrative organization have been proposed for managing the EUSO ground segment.

Bibliography

[1] Hess, Victor F. The Electrical Conductivity of the Atmosphere and Its Causes. Constable and Company. (1928).

[2] J. H. Adams et al, An evaluation of the exposure in nadir observation of the JEM-EUSO misión, Astroparticle Physics, Vol 44, pp 76-90, 2013.

[3] M.D. Rodríguez Frías for the JEM-EUSO Collaboration, The JEM-EUSO Space Mission @ forefront of the highest energies never detected from Space, Proc. Workshop on Multifrequency Behaviour of High Energy Cosmic Sources, MdSAI, 83, 337-341, 2012.

[4] Rodríguez Frías, M. D. et al. for the JEM-EUSO Collaboration., The JEM-EUSO Space Mission: Frontier Astroparticle Physics at ZeV range from Space., Homage to the Discovery of Cosmic Rays. Nova Science Publishers, New York, ISBN: 978-1-62618-998-0, Inc, pg 201-212, (2013).

[5] R. A. Mewaldt. Macmillan Encyclopedia of Physics, 1996.

[6] Kampert, Karl-Heinz and Watson, Alan. Extensive Air Showers and Ultra High-Energy Cosmic Rays: A Historical Review. The European Physical Journal H, 2012.

[7] von W. Heitler and Nordheim, 1934. Search for electron-positron pair production by non-relativistic heavy charged particles.

[8] La colaboración JEM-EUSO, https://jemeuso.riken.jp.

[9] The JEM-EUSO Collaboration., Adams, J.H., Ahmad, S. et al. The Atmospheric Monitoring System of the JEM-EUSO instrument. Experimental Astronomy, Volume 40, 45-60 (2015). DOI 10.1007/s10686-014-9378-1

[10] The JEM-EUSO Collaboration (corresponding authors: Toscano, S., Morales de los Ríos, J. A., Neronov, A., Rodríguez Frías M. D., & Wada, S.)., The Atmospheric Monitoring System of the JEM-EUSO instrument., Experimental Astronomy, 37, (2014), doi=10.1007/s10686-014-9378-1.

[11] Rodríguez Frías, M.D., Toscano, S., Bozzo, E., del Peral, L., Neronov, A., and Wada, S. and for the JEM-EUSO Collaboration., The Atmospheric Monitoring System of the JEM-EUSO Space Mission, Proceedings of the 2^{nd} AtmoHEAD Conference, Padova (Italy), ArXiv:1501.0482 [astro-ph.IM] (2014).

[12] Rodríguez Frías, M. D. et al. for the JEM-EUSO Collaboration., The Atmospheric Monitoring System of the JEM-EUSO Space Mission., Proc. International Symposium on Future Directions in UHECR Physics, The European Physical Journal, 53, 10005-pg1-7, (2013), http://dx.doi.org/10.1051/epjconf/20135310005.

[13] M.D. Rodríguez Frías for the JEM-EUSO Collaboration, The Atmospheric Monitoring System of the JEM-EUSO Space Mission. Proc.

International Symposium on Future Directions in UHECR Physics, CERN. The European Physical Journal, 2012.

[14] A. Neronov, S. Wada, M.D. Rodríguez Frías et al., Atmospheric Monitoring System of JEM-EUSO, Proceedings of 32nd International Cosmic Ray Conference (ICRC), Beijing, 6, 332 (2011). (Preprint) Arxiv:1204.5065.

[15] S. Wada, T. Ebisuzaki, T. Ogawa, M. Sato, T Peter, V. Mitev, R. Matthey, A. Anzalone, F. Isgro, D. Tegolo, E. Colombo, J.A, Morales de los Ríos, M. D. Rodríguez Frías, Park II, Nam Shinwoo, Park Jae and JEM-EUSO Collaborators, Potential of the Atmospheric Monitoring System of JEM-EUSO Mission, Proc 31st International Cosmic Ray Conference (2009).

[16] W. Herschel, Experiments on the Refrangibility of the invisible Rays of the Sun. LL. D. F.R.S, 1800.

[17] J.A. Morales de los Rós et al., The IR-Camera of the JEM-EUSO Space Observatory, Proceedings of 32nd International Cosmic Ray Conference (ICRC), Beijing, 11, 466 (2011).

[18] Rodríguez Frías, M. D. et al. Towards the Preliminary Design Review of the Infrared Camera of the JEM-EUSO Space Mission., Proc. International Cosmic Rays Conference, Rio de Janeiro, Brazil, arXiv:1307.7071v1 [astro-ph.IM], (2013).

[19] J.A. Morales de los Rios, E. Joven, L. del Peral, M. Reyes, J. Licandro & M. D. Rodriguez Frias, The JEM-EUSO Space Mission Infrared Cam-

era Prototype Characterization, Advances in Space Research: Special Issue "Centenary of the discover of the Cosmic Rays", 2013.

[20] The JEM-EUSO Collaboration (corresponding authors Morales de los Rios, J. A. & Rodríguez Frías, M. D.), The infrared camera onboard JEM-EUSO, Experimental Astronomy, 37, doi=10.1007/s10686-014-9402-5, (2014).

[Morales de los Ríos et al.] Morales de los Ríos, J. A., Joven, E., del Peral, L., Reyes, M., Licandro, J., and Rodríguez Frías, M. D., The Infrared Camera Prototype Characterization for the JEM-EUSO Space Mission., Nuclear Instruments and Methods NIMA, 749, 74-83, ISSN 0168-9002 (2014).

[21] IRXCAM Control Application Software User Manual, INO, September 2010.

[22] "Infrared Reference Source DCN 1000 User's Manual", HGH Systems infrarouges (version August, 2010).

[23] Integration of the Plank blackbody radiation function, Bulletin American Meteorological Society, vol-57 No-10, (1976).

[24] J.A. Morales de los Rios et al. An end to end simulation code for the Infrared Camera of the JEM-EUSO Space Mission., Proc. International Cosmic Rays Conference, Rio de Janeiro, Brazil, (2013).

The JEM-EUSO Collaboration, The JEM-EUSO Mission: Contributions to the ICRC 2013, Proc. of 33rd International Cosmic Ray Conference (ICRC), Rio de Janeiro, Brazil. ArXiv:1307.7071, (2013).

[25] Hirohiko Masunaga et al, Satellite Data Simulator Unit, A multisensor, multispectral Satellite Simulator Package, 2010, American Meteorological Society.

[26] MODIS (Moderate Resolution Imaging Spectroradiometer) NASA website: http://modis.gsfc.nasa.gov/ & http://ladsweb.nascom.nasa.gov/data/search.html.

[27] CALIPSO (Cloud-Aerosol Lidar and Infrared Pathfinder Satellite Observation) NASA website: http://www-calipso.larc.nasa.gov/ , CNES website: http://smsc.cnes.fr/CALIPSO/

[28] CODE V Optical Design Soft., http://www.opticalres.com/

[29] JANOS, SURNIA Lenses Website: http://www.janos-tech.com/products-services/thermal-imaging-lenses/surnia-lenses.html

[30] HP Labs LOCO-I/JPEG-LS, http://www.hpl.hp.com/loco/

[31] Qiang Fu and K.N. Liou, Parametrization of the Radiative Properties of Cirrus Clouds, 2008, Journal or the Atmospheric Sciences.

[32] D. Heck, Extensive Air Shower Simulations with CORSIKA and the influence of High-Energy Hadronic Interaction Models. https://arxiv.org/abs/astro-ph/0103073, 2001.

D. Heck, J. Knapp, J.N. Capdevielle, G. Schatz, T. Thouw, Forschungszentrum Karlsruhe Report FZKA 6019 (1998).

[33] S. Sciutto, Simulation of Particle Air Showers, http://aires.fisica.unlp.edu.ar

S. J. Sciutto, The AIRES system for air shower simulations. An update, Contributed to 27th International Cosmic Ray Conferences (ICRC 2001), Hamburg, Germany, 7-15 Aug 2001.

[34] T. Pierog et al, First results of fast one-dimensional hybrid simulation of EAS using CONEX, Nucl.Phys.Proc.Suppl. 151:159-162 (2006).

[35] S.Bottai et al., Simulation and Data Analysis for EUSO, Proceedings of 28th ICRC Tsukuba (2003) 943.

[36] Alice Techical Design Report, CERN-LHCC-2005-018, Alice TDR 021, (2005).

[37] Alice Computing Model, CERN-LHCC-2004-028/G-086 (2005).

[38] Roger Jones, The ATLAS Computing Model, International ICFA Workshop on Grid Activities, Lancaster University (2006).

[39] M.C.Espirito Santo et al., The EUSO Science Operations and Data Centre, Proceedings of 28th ICRC Tsukuba (2003) 1089.

[40] EGEE-III, Functional Description of Grid Components and Associated Work Plan, EGEE-III-MJRA1.3.1-945450-v5-1,(2009).

[41] Scientific Linux https://www.scientificlinux.org/

[42] Vance, Ashlee (2003-12-17). "Sun and UC Berkeley are about to BOINC". The Register.

[43] BOINC http://boinc.berkeley.edu/

[44] A synthetic benchmark, H J Curnow and B A Wichmann, Computer Journal, Vol 19, No 1, pp43-49, (1976).